POLITECNICO DI MILANO

Civil Engineering for Risk Mitigation (CERM)

MASTER OF SCIENCE IN CIVIL ENGINEERING

"live-bed pier scour under steady and unsteady conditions"

Supervisor: PROF. Alessio Radice.

Co-supervisor: PROF. Andrea Galli.

Ahmed Monofy

860102

April 2018

Acknowledgements

I wish to deeply thank my parents who have been always exerting countless effort to support me throughout my entire life. Special thanks to Prof. Alessio Radice who is always a gentile advisor and instructor, the one who widened our background with his extensive information and scientific work about hydraulics and morphology that is a crucial field in my country particularly because of the existence of Nile river. Personally, I have acquired good experience by working under his supervision, specially, in work organizing and planning as well as dealing with laboratory facilities. Beside his significant help in writing this manuscript. This work could not have been that much valuable without the help introduced by Prof. Andre Galli who deducted an appreciated time, despite his overwhelming work, to help achieving tangible results in the geotechnical modeling that is important for the completion of this work.

Gratefully, I would like to thank all my friends who have helped me to reach this point, specially, Jorge Perez Loaiza who tried to help me explaining some basic knowledge that I have lack of, to work on the geotechnical part.

Appreciated work is always done by the administration’s members, it is worth mentioning the effort of Mr. Alessio Meoli to help the foreign student upon their first arrival and throughout their study period.

Abstract

The experimental campaign is dedicated to test and understand the pier scour phenomenon under steady and unsteady flow in live-bed condition. In addition, the interaction between the incoming dunes. and the scour process in vicinity of the pier is investigated

For the steady conditions, two discharge values of 1.4 and 1.6 times the threshold flow rate are selected. A number of measuring positions are introduced to study the scour development, the characteristics of the dunes and their relationship with the scour depth, and finally the time-varying slope of the scour hole. The equilibrium time to achieve a dynamic equilibrium is found to be a decreasing function of the flow rate. The mean and minimum scour depths within the fluctuations after equilibrium are decreasing functions of the flow rate, while the maximum depth is an increasing function of the flow rate. The dune control of the scour fluctuations is analyzed. The amplitude of scour depth and dune fluctuations is computed based on different probability ranges to find out the interdependency between the depth fluctuation within the scour hole and the migrating dunes upstream. The amplitudes are similar for the dunes and the scour depth at the lower discharge; however, higher are found for elevation variation at mid-slope of the scour hole. On the contrary, for the higher discharge, the opposite trend is observed, with all the amplitudes of the points within the hole are similar and higher than the points upstream of the hole. Autocorrelation functions are used to assess the time scales of the dunes and the scour depth fluctuations. Further analysis of the scour hole is carried out to understand the mechanism of sediment avalanche within the hole. Slope stability analysis is performed using the Fellenius method to enlighten the mechanism of sediment failure into the hole, in this way interpreting the experimental measurements of the hole slope variation. In addition, the scour hole slope dependency on the flow rate is measured, as higher slope is evident at lower flow rate. Moreover, the celerity of the dunes is calculated using three different methods (cross-correlation function, user-determined overlap and sediment mass balance using the amplitude values), finding the dunes celerity as an increasing function of the flow rate. Discharges of 1.2, 1.4 and 1.6 times the threshold were used to build different stepwise hydrographs for unsteady runs, where equilibrium sediment feeding was always used. The distance of the next approaching dune to the pier nose at the time of discharge modification is the experimental control introduced to assess the scour depth behavior during the transition phases between the hydrograph steps. The scour proceeds more when the nearest dune is far upstream and is instead lowered when the dune is on the edge of the scour hole at the time of discharge modification. The mean, minimum and maximum values of the scour depth at different hydrograph steps are evaluated, with the mean and minimum gradually decreasing during the rising limb, while the maximum scour depth remains almost constant over the whole period of the hydrograph.

Astratto

La campagna sperimentale è volta a studiare il fenomeno dell’erosione localizzata a una pila di ponte, in condizioni di live-bed e con flussi sia stazionari che non stazionari. Inoltre, è studiata l'interazione tra le dune in arrivo e il processo erosivo in prossimità della pila.

Le prove in condizioni stazionarie sono state condotte per due valori di portata, pari a 1,4 e 1,6 volte la portata limite per il trasporto solido. La quota del letto è stata misurata in continuo in numerose posizioni per studiare lo sviluppo dello scavo localizzato, le caratteristiche delle dune e, infine, la pendenza della buca di erosione. Il tempo necessario per raggiungere un equilibrio dinamico si rivela essere una funzione decrescente della portata. Le profondità di scavo medie e minime (considerando le fluttuazioni dopo il raggiungimento dell'equilibrio) sono funzioni decrescenti della portata, mentre la profondità massima è una funzione crescente della portata. Per quanto riguarda il controllo esercitato dalle dune sulle fluttuazioni della profondità di erosione, l'ampiezza delle oscillazioni è stata calcolata in base a diversi intervalli di probabilità ed è risultata simile per le dune e la profondità di erosione alla portata inferiore (per quanto, tuttavia, ampiezze maggiori si siano misurate lungo il pendio di monte della buca di erosione). Al contrario, per la portata maggiore, si è osservata una tendenza differente, con le ampiezze delle oscillazioni dello scavo maggiori di quelle relative alle dune in arrivo. Sono state usate delle funzioni di autocorrelazione per valutare le scale temporali delle dune e delle fluttuazioni della profondità di erosione. Ulteriori analisi sono state effettuate per comprendere il meccanismo degli scivolamenti del materiale solido nella fossa di erosione. L'analisi della stabilità del pendio è stata eseguita utilizzando il metodo Fellenius, interpretando in questo modo le misurazioni sperimentali della variazione della pendenza della buca. Infine, la celerità delle dune è stata calcolata utilizzando tre diversi metodi, ed è risultata essere una funzione crescente della portata.

Le prove in condizioni non stazionarie sono state realizzate creando degli idrogrammi a gradini con le portate di 1,2, 1,4 e 1,6 volte la portata limite. L’alimentazione solida è stata sempre mantenuta in equilibrio con la portata idrica. Le prove non stazionarie sono state condotte variando il tempo a cui la portata veniva modificata, in funzione della posizione della duna più prossima alla buca di erosione. L’erosione procede maggiormente quando la duna più vicina è distante dalla buca, e viene invece smorzata quando la duna si trova sul bordo della fossa di erosione al momento della modifica della portata. Sono stati valutati i valori medi, minimi e massimi della profondità di scavo nelle diverse fasi dell'idrogramma, con le medie e i minimi gradualmente decrescenti durante la fase di crescita, mentre la profondità massima è rimasta quasi costante per tutto il periodo dell'idrogramma.

نبذة مختصرة

الدراسة الحالية تكرست لاختبار و فهم ظاهرة النحر التي تحدث امام أعمدة الكباري تحت تصرف المياه الثابت والمتغير في حالة وجود رواسب متحركة في القاع. لذلك تم العمل على فهم تلك الظاهرة وعلاقة النحر بالامواج الرملية المتحركة القادمة من أعلى القناة.

في التصرف الثابت, تم تطبيق قيمتين هما 1.4 و 1.6 من قيمة التصرف الذي يبدأ عنده تحرك الرمال بالقاع. عدد من اوضاع نقاط القياس تم تطبيقها من اجل فهم صفات الامواج الرملية وعلاقتها مع عمق النحر وتغير ميل الحفرة الناتجة عن النحر. الوقت اللازم للوصول لحالة توازن عمق النحر ينقص مع زيادة مقدار التصرف. اقل عمق نحر والعمق المتوسط الذي يحدث بعد الوصول لحالة التوازن يقل مع زيادة التصرف, بينما اقصى عمق نحر يزداد مع زيادة التصرف . تأثير الموج الرملية على عملية النحر تم دراستها. سعة التغير في عمق النحر و الامواج الرملية تم حسابهم على أساس عدد من نطق الإحتمالات. لكي يتم فهم العلاقة بين الامواج الرملية المتحركة وتغير عمق النحر. في حالة التصرف الاقل, وجد ان سعة تغير عمق النحر تطابق مع سعة تغير ارتفاع الامواج الرملية ولكن اكبر سعة تغير توجد على السطح المال لحفرة النحر. على العكس للتصرف الأعلى, سعة التعير في عمق النحر داخل حفرة النحر متشابه ولكنه أعلى من سعة التغير للنقاط المتواجدة قبل حفرة النحر. تستخدم دالة الترابط الذاتي لتقييم المقاييس الزمنية الأمواج الرملية وتذبذبات عمق النحر . يتم إجراء مزيد من التحليل لحفرة النحر من أجل فهم آلية الانهيار االرملي داخل الحفرة. يتم إجراء تحليل ثبات المنحدر باستخدام طريقة Fellenius لتنوير آلية انهيار الرمال في الحفرة ، وبهذه الطريقة يفسر القياسات التجريبية لتغير منحدر الحفرة .بالإضافة إلى ذلك ، يتم قياس اعتماد ميل الحفرة على معدل التصرف ، حيث أن الانحدار الأعلى واضح عند انخفاض معدل التدفق. علاوة على ذلك ، يتم حساب سرعة الامواج الرملية باستخدام ثلاث طرق مختلفة (دالة الارتباط المتبادل ، والتداخل الذي يحدده المستخدم وتوازن الكتلة الرسوبية باستخدام قيم الاتساع) ، وإيجاد تزايد سرعة الامواج الرملية بزيادة معدل التصرف .

تم استخدام التصرفات من 1.2 ، 1.4 و 1.6 مرة من التصرف الذي يبدأ عنده تحرك الرمال لبناء تصرف متدرجة ، حيث كان يتم اختبار تأثير مسافة اقرب موجة رملية من الحفرة عا تغير عمق النحرأثناء الإنتقال من تصرف إلى آخر. ويستمر النحر أكثر عندما تكون اقرب موجة رملية بعيدة عن الحفرة ويقل عندما تكون الموجة على حافة الحفرة عند تعديل التفريغ. يتم تقييم القيم المتوسطة والقصوى واالصغرى لعمق االنحر عند التصرفات المختلفة ، مع انخفاض العمق المتوسط والاقل تدريجيًا خلال زيادة التصرف تدريجيا ، بينما يبقى أقصى عمق للنحر ثابتًا تقريبًا طوال فترة التصرفات المتغيرة بالكامل.

Table of contents

1. **Introduction**.....1

2. **Sediment transport in open channel and bridge pier scour** 4

2.1. Sediment Transport.....4

2.1.1 Bed formation.....4

2.1.2 Physical properties of sediments.....6

2.1.3 Bed load transport.....8

2.2. Pier Scour.....11

2.2.1 Local scour.....11

2.2.2 Clear water and live-bed scour.....13

2.2.3 Steady-flow scour studies.....14

2.2.4 Unsteady-flow Clear-water scour studies.....20

2.2.5 Conclusion of pier scour studies and motivation.....24

3. **Laboratory Description**.....25

3.1 Experimental facilities.....25

3.1.1 water discharge measurements and components.....27

3.1.2 sediment particles' properties.....29

3.1.3 sediment feeding component.....30

3.2. Measuring devices.....32

3.2.1 measuring tools and accuracy.....33

3.2.2 Software process.....38

3.3. Experimental Campaign.....38

3.3.1 experimental set up.....38

3.3.2 Threshold conditions....39

4. Steady flow rate experiments and analysis....41

4.1. Steady experimental runs....41

4.1.1 data despiking....45

4.2. Scour experiments analysis....47

4.2.1 Scour equilibrium time and Depth....47

4.2.2 Scour depth and bed fluctuations....51

4.2.3. scour hole slope analysis....62

4.2.4. time scale analysis of scour....74

4.3. Dunes characteristics....79

4.3.1. time scale analysis of dunes....79

4.3.2. dune celerity....85

4.4. Comparison with previous results....95

5. Live-bed scour Unsteady flow study....98

5.1 Unsteady scour experiments....98

5.2 **Unsteady Experiments Analysis**....100

5.2.1 Scour progression phase....100

5.2.2 Scour depth and transition phases....101

5.2.3 Scour depth variation....108

Conclusions....112

References....114

List of Figures.

Figure (1- 1): Main causes of bridge collapse (Imhof, 2004). 2
Figure (1- 2): Different natural hazards causing bridge collapse (Imhof, 2004). 2

Figure(2- 1): Bed forms in movable boundary hydraulics: (a) typical bed forms and (b) bed form motion(Chanson,2004). 5
Figure (2- 2): Sediment size distribution sample(Chanson,2004). 7
Figure (2- 3): Examples of angle of repose(Chanson,2004). 7
Figure (2- 4): Forces acting on a sediment particle (Chanson,2004). 8
Figure (2- 5): Shields parameter as a function of the particle Reynolds number for sediment in water (Chanson,2004). 10
Figure (2- 6): Bed-load motion: (a) sketch of saltation motion and (b) definition sketch of the bed-load layer(Chanson,2004). 10
Figure (2- 7): Sketch of the system of vortices at a bridge pier (Melville and Coleman, 2000). 12
Figure (2- 8): Time evolution of scour depth in clear-water and live-bed conditions (Brandimarte et al,2012). 13
Figure (2- 9): Relative equilibrium scour depth, Sd\b versus velocity excess, V/V_c for d_{50} = 0.6 and 0.85 mm. (Chiew and Melville,1984). 15
Figure (2- 10): Relative equilibrium scour depth versus D/d50 at various values of V/V_c. (Chiew and Melville,1984). 16
Figure (2- 11): Evolution of dimensionless scour depth at pier nose under steady flow (Chang et al,2004). 18
Figure (2- 12): Measured equilibrium scour depth H/b over flow intensity V/Vc (Ettmer et al, 2015). 19
Figure (2- 13): Stepwise hydrographs for Runs U1–U13 (Chang et al, 2004). 21
Figure (2- 14): Evolution of dimensionless scour depth at pier nose under stepwise hydrograph (Chang et al, 2004). 22
Figure (2- 15): Superposition of scour evolution under stepwise hydrograph (line) and steady flow conditions for each step (circles, squares, and diamonds) (Lopez et al,2014). 23
Figure (2- 16): The temporal scour depth fluctuation change with the flow velocity (Melville and Coleman,2000). 24

Figure (3- 1): Hydraulics laboratory 25
Figure (3- 2): Hydraulics laboratory sketch 25
Figure (3- 3): Experiment's channel 25
Figure (3- 4): Experiment's units plan sketch 26
Figure (3- 6): Inlet tank 27
Figure (3- 5): Inlet pipes' connection 27
Figure (3- 7): Channel's Inlet straightener pipes 28
Figure (3- 8): Flow meter reader 28
Figure (3- 9): Flow meter device 28

Figure (3- 10): Control valve 29
Figure (3- 11): CDF of sediment samples 30
Figure (3- 12): Hopper (Sediment feeder) 31
Figure (3- 13): Hopper controller 31
Figure (3- 14): Perforated pipe for wetting sediment 32
Figure (3- 15): Lasers 33
Figure (3- 16): Laser measuring concept. 33
Figure (3- 17): Lasers' calibration curve. 36
Figure (3- 18): Voltmeter 37
Figure (3- 19): Acquisition tool and power supply 37
Figure (3- 20): Experimental set up sketch (Radice and Lauva,2017). 39
Figure (3- 21): Critical flow for incipient motion (Veronica, 2015). 40

Figure (4- 1): Bed fluctuation sample in E3 44
Figure (4- 2): Scour evolution phases. 44
Figure (4- 3): Raw data sample. 45
Figure (4- 4): Despiked data 46
Figure (4- 5): Unrefined despiked data 46
Figure (4- 6): Refined and despiked data 47
Figure (4- 7): Scour depth evolution at different discharge. 48
Figure (4- 8): Dimensionless equilibrium time at different discharge. 48
Figure (4- 9): Scour depth fluctuation for Q=1.4Qc 49
Figure (4- 10): Scour depth fluctuation for Q=1.6Qc 50
Figure (4- 11): Dimensionless mean, maximum and minimum scour depth change with discharge ratio. 51
Figure (4- 12): Experiment E1 measurements. 52
Figure (4- 13): Experiment E2 measurements. 53
Figure (4- 14): Dimensionless amplitude profile for Q=1.4Qc. 54
Figure (4- 15): Experiment E3 measurements. 55
Figure (4- 16): Experiment E4 measurements 55
Figure (4- 17): Experiment E5 measurements. 56
Figure (4- 18): Dimensionless amplitude for measuring points of E3,E4 and E5;(a) probability range 80%,(b)probability range 90%, (c)probability range 95%,(d) probability range 98%. 57
Figure (4- 19): Experiment E6 measurements. 58
Figure (4- 20): Experiment E7 measurements 59
Figure (4- 21): Dimensionless amplitude profile for Q=1.6Qc 59
Figure (4- 22): Dimensionless amplitude at far distances for different discharge;(a) probability range 80%, (b) probability range 90%,(c) probability range 95%, (d) probability range 98%. 60
Figure (4- 23): Dimensionless amplitude at close distances for different discharge;(a) probability range 80%, (b) probability range 90%,(c) probability range 95%, (d) probability range 98%. 61
Figure (4- 24): Temporal scour slope variation at different directions;(a) on the central axis, (b) on 45o inclined direction to the right side, (c) on 45oinclined direction to the left side. 62

Figure (4- 25): Scour slope mean, minimum and maximum values at different directions. 63
Figure (4- 26): Scour slope variation during E7. 63
Figure (4- 27): Scour slope comparison between E3 and E7. 64
Figure (4- 28): Scour slope variation with scour depth at different point. 65
Figure (4- 29): Slope variation trend vs scour depth at points within the scour hole in E3. 65
Figure (4- 30): Slope variation trend vs scour depth at points within the scour hole in E7. 66
Figure (4- 31): Schematic of scour hole in flow direction (Wu et al,2016). 67
Figure (4- 32): Definition Diagram for Factor of Safety. 67
Figure (4- 33): Dividing the sliding mass into n slices 68
Figure (4- 34): Forces acting on each slice. 68
Figure (4- 35): Dune's dimensions' parameters 69
Figure (4- 36): Bed geometry and dune’s load distribution. 70
Figure (4- 37): Mobilized volume variation with hydraulic gradient at different friction angle. 71
Figure (4- 38): Different tried locations of point (P2). 72
Figure (4- 39): Different tried critical surfaces with their corresponding safety factors. 72
Figure (4- 40): Immediate slope angle after failure variation with p2 locations. 72
Figure (4- 41): The net accumulated volume downstream of the triggering point. 73
Figure (4- 42): Autocorrelation of slope variation in E3, E4 and E5. 74
Figure (4- 43): CDF of slope variation series in E3,E4 and E5. 75
Figure (4- 44): Autocorrelation of scour hole slope variation in E3 and E7. 75
Figure (4- 45): CDF analysis of scour hole slope variation in E3 and E7. 76
Figure (4- 46): Autocorrelation function comparison between measuring points within the scour hole and hole slope, (a) in case of Q=1.4Qc and E3, (b) in case of Q=1.6Qc and E7. 77
Figure (4- 47): Autocorrelation of water depths at points inside the scour hole in E3 and E7 78
Figure (4- 48): CDF of depths measured at points inside the scour hole during E3 and E7. 79
Figure (4- 49): Autocorrelation function of depths at points upstream the scour hole during E1 and E6. 80
Figure (4- 50): CDF of measuring points upstream the scour hole in E1 and E6. 81
Figure (4- 51): Autocorrelation of a measuring point inside and outside the scour hole for Q=1.4Qc 82
Figure (4- 52): Autocorrelation of a measuring point inside and outside the scour hole for Q=1.6Qc 82
Figure (4- 53): CDF of a point inside and outside the scour hole for discharge of 1.4Qc and 1.6Qc. 83
Figure (4- 54): Autocorrelation of depths at points inside and outside the scour hole at Q=1.4Qc. 84
Figure (4- 55): Autocorrelation of points inside and outside the scour hole at Q=1.6Qc. 84
Figure (4- 56): Experiment E1 setup. 85
Figure (4- 57): Dunes originally exist at points 2 and 3 for Q=1.4Qc. 86
Figure (4- 58): Matched dunes between points 2 and 3. 86
Figure (4- 59): Cross correlation function between points 2 ad 3 for Q=1.4Qc. 87
Figure (4- 60): Celerity values obtained by all the methods of computation for all the reaches. 90
Figure (4- 61): Experiment E6 setup. 90
Figure (4- 62): Dunes originally exist at points 2 and 3 for Q=1.6Qc. 91
Figure (4- 63): Matched dunes between points 2 and 3. 91
Figure (4- 64): Cross correlation function between points 2 ad 3 for Q=1.6Qc. 92
Figure (4- 65): Celerity values obtained by all the methods of computation for all the reaches. 94

Figure (4- 66): Celerity values for different flow rate computed by different methods. 95
Figure (4- 67): Scour evolution and fluctuation comparison with (Radice and Luava, 2017)..... 96
Figure (4- 68): Scour evolution and fluctuation comparison with some previous studies. 96
Figure (4- 69): Scour depth comparison between present study and previous ones: (a) mean scour depth,(b) maximum scour depth. 97
Figure (4- 70): Dimensionless equilibrium time similarity with (Radice and Lauva,2017)..... 97

Figure (5- 1): Scour evolution in different steady and unsteady experiments. 100
Figure (5- 2): Dimensionless equilibrium time for steady and unsteady experiments..... 101
Figure (5- 3): Hydrographs time steps. 102
Figure (5- 4): Left panels: water hydrographs. Right panels: sediment feeding hydrograph. (a) the hydrographs applied to T1. (b) hydrographs applied to T2. (c) hydrographs applied to T3.(d) hydrographs applied to T4. 103
Figure (5- 5): Scour depth temporal evolution and variation during T1. 104
Figure (5- 6): Scour depth temporal evolution and variation during T2. 105
Figure (5- 7): Scour depth temporal evolution and variation during T3. 105
Figure (5- 8): Scour depth temporal evolution and variation during T4. 106
Figure (5- 9): Scour depth comparison between unsteady clear water conditions and unsteady live bed conditions..... 108
Figure (5- 10): Mean, maximum and minimum scour depth for different experiment: (a)mean scour depth,(b) maximum scour depth,(c) minimum scour depth. 109
Figure (5- 11): Mean, maximum and minimum scour depth for unsteady live bed condition. 110
Figure (5- 12): Scour depth comparison between steady and unsteady conditions. (a) maximum, (b)mean,(c) minimum. 111

List of Tables.

Table (1- 1): Percentage of collapsed bridges over time (Imhof, 2004). 3

Table(2- 1): Basic bed forms in alluvial channels.(Henderson,1966 and Graf ,1971) 5
Table(2- 2): Sediment size classification(Chanson,2004). 6
Table (2- 3): Properties of sediments used in experiments (Chiew and Melville,1984). 15
Table (2- 4): Experimental conditions (Chang et al,2004). 17
Table (2- 5): experimental conditions (Chang et al,2004). 19
Table (2- 6): Experimental Conditions for the unsteady conditions (Chang et al, 2004). 21
Table (2- 7): Conditions for Unsteady Tests (Lopez et al,2014). 23

Table (3- 1): Sediment properties 30
Table (3- 2): Hopper slot width and cycle duration for different Q/Qc(Radice and lauva,2017). 32
Table (3- 3): Lasers' calibration computations. 36
Table (3- 4): Lasers' calibration parameters 36

Table (4- 1): Steady Experiments. 42
Table (4- 2): Experiments description and measuring points placement. 43
Table (4- 3): Dimensionless equilibrium time for different experiments 49
Table (4- 4): Scour depth values for different experiments 50
Table (4- 5): Dimensionless scour depth for different experiments 50
Table (4- 6): The main mechanical parameters. 69
Table (4- 7): Dune's dimensions and load. 69
Table (4- 8): Integral scale of correlation of points within the scour hole and slope variation in E3 and E7. 77
Table (4- 9): Integral scale of correlation of points inside the scour hole in E3 and E7 78
Table (4- 10): Mean depth and dispersion range of depths at measuring points inside the scour hole during E3 and E7. 79
Table (4- 11): Integral scale of correlation of the points upstream the scour hole during E1 and E6. 80
Table (4- 12): Mean depth and dispersion range of depths at measuring points outside the scour hole in E1 and E6. 81
Table (4- 13): Mean depth and dispersion range of depths at a measuring points inside and outside the scour hole for 1.4Qc and 1.6Qc. 83
Table (4- 14): Integral scale of correlation for points inside and outside the scour hole at Q=1.4Qc. 84
Table (4- 15): Integral scale of correlation for points inside and outside the scour hole at Q=1.6Qc. 84
Table (4- 16): Matching results. 87
Table (4- 17): Matching results for all reaches for Q=1.4Qc. 87

Table (4- 18): Cross correlation function for all the reaches. 88
Table (4- 19): Celerity values result from sediment mass balance for Q=1.4Qc. 89
Table (4- 20): Celerity values obtained by all the methods of computation for Q=1.4Qc..... 89
Table (4- 21): Matching results for all reaches for Q=1.6Qc..... 91
Table (4- 22): Cross correlation function for all the reaches. 92
Table (4- 23): Celerity values result from sediment mass balance for Q=1.4Qc. 93
Table (4- 24): Celerity values obtained by all the methods of computation for Q=1.6Qc..... 94

Table (5- 1): Water and sediment discharges characteristics (Radice and lauva,2017). 99
Table (5- 2): Experiments set up and illustrative description. 99
Table (5- 3): Equilibrium time characteristics for different steady and unsteady experiments..... 101
Table (5- 4): Hydrographs time steps for unsteady experiments. 102
Table (5- 5): Transition phases in T2, T3 and T4. 106

List of symbols.

Fr= Froude number.

S= Relative density.

$\rho_{s=}$ the sediment density(kg/m^3).

ρ= the fluid density(kg/m^3).

d_s= sediment size (mm).

d_{50}= sediment size for which 50% by weight of the material is finer (mm).

d_{16}= sediment size for which 16% by weight of the material is finer (mm).

d_{84}= sediment size for which 84% by weight of the material is finer (mm).

d_{90}= sediment size for which 90% by weight of the material is finer (mm)

σ_g= the geometric standard deviation.

Φ= the sedimentological size parameter.

Φ_s= the angle of repose.

g= the gravity acceleration.

v_s= the volume of the sediment particle.

A_s= characteristic particle cross-sectional area.

F_b= the buoyancy force.

C_d= the drag force.

C_L= the lift force.

T_o= The bed shear stress.

μ= the fluid viscosity.

V_*= the shear velocity.

R_H=hydraulic radius.

n_{skin}=skin friction coefficient.

T*=shield's number.

Re*=friction reynod's number.

(T *)c = critical shield's number.

C_s= sediment transport.

δ_s= bed load active layer.

V_s= sediment particle velocity.

$\acute{m}_s$= the mass sediment flow rate per unite width.

q_s= the specific mass of sediment.

R_e= Reynold's number.

V= mean velocity.

V_c=critical velocity for sediment incipient motion.

b= pier diameter.

H= the flow depth.

Sd= the scour depth.

V_p= peak velocity.

te= equilibrium time.

t_p= time of peak discharge.

T_d= experimental run time.

Q= water discharge.

Q_c=Critical water discharge at bed load incipient motion.

d_{eq}= equivalent diameter of sediment particle.

P= porosity.

Qs= the solid discharge per unit width (m^2/s).

Dist= distance (cm).

Ø= dimensionless sediment transport rate per unit width.

i= hydraulic gradient.

Δ_{ds}= amplitude of scour depth.

Δ_d= amplitude of dunes.

x_d= dune distance upstream of the pier nose (m).

h = dune's height (m)

l1= dune's front length(m)

l2= dune's tail length (m)

q_{max} = dune's load per unit width (KPa)

γ_{wat} = specific weight of water (kN/m^3).

γ_{dry}= the specific weight of dry sediment(kN/m^3).

γ_{sat}= the saturated unit weight(kN/m^3).

γ_{eff}= the effective unit weight(kN/m^3).

COR= the center of rotation of a sliding mass.

k = a separation time.

σ_x= the variance of x series.

λ= the integral scale of correlation.

L = the time lag.

σ_y = the variance of y series.

C=celerity (cm/sec).

B =channel width.

λ_D= dune wavelength.

T_D =dune period.

W_D =the volume of one dune.

d = the distance between the two measuring points (cm).

Prop = probability range.

Fs= factor of safety.

τ_{ff} = the maximum shear stress that the soil can sustain.

σ_n =normal stress.

τ = the actual shear stress

W_i = the weight of slice i.

α_i=the slope of slice i bed.

C'= the cohesion coefficient.

1.Introduction

The history of ridge hydraulics is replete with incidents of failed bridges did not adequately account for the capacity of alluvial rivers to erode, or scour, channel beds and banks. Images of undermined piers, undercut abutments, and washed-out bridges approaches have haunted bridge engineers since antiquity (Melville and Coleman, 2000).

Generally, a crossing bridge, with pier and abutments in the river bed and banks, represents an alteration of the natural geometry of the river section and, thereby, creates an obstacle for the river flow that, as it approaches the bridge, has to change its own natural pattern; furthermore, because of the modified flow conditions at the bridge crossing, the streamflow acquires a strong erosive power. Consequently, in the subcritical flow conditions that are usually encountered in river channels, the resulting increase in flow velocity and erosive power of the streamflow creates conditions that endangers the stability of bridge foundations.

An interesting and valuable document by Titus Livius represents one of the most ancient evidence of the interaction between water and bridges: The Roman historian recorded that in 193 B.C. a flood destroyed two wood bridges over river Tiber, in Rome. Other floods occurred and, as a direct consequence, the censors Marcus Aemilius Lepidus and Marcus Fulvius Nobilior were asked to build the first bridge in stone in Rome (Bersani and Bencivenga, 2001; Lagunes, 2004).

The story of this unfortunate bridge that proved to be extremely sensitive to the scouring effect of the flowing water is characterized by a series of interventions that were designed to stabilize the structure after being damaged by several flood events (Bersani and Bencivenga, 2001). The last reconstruction lasted only 23 years because on December 24th,1598 three of the six arches of the bridge were destroyed by an extraordinary flood of Tiber River and since then the bridge got the name of “Ponte Rotto” (Broken Bridge). Only one of the six original arches of the bridge is still standing and Ponte Rotto is now an attractive roman ruin for tourists and a token of bridge scouring for technicians (Brandimarte et al. 2012).

Indeed, even now in modern times, pier and abutment undermining due to scouring and riverbed erosion has been widely recognized as being the main cause for bridge damage and failure (Melville and Coleman, 2000; Richardson and Davis, 2001). According to a comprehensive collection of bridge failure data worldwide gathered by Imhof (2004), natural hazard is the main cause of bridge collapse as demonstrated in figure (1-1) and among the natural hazard listed causes, flooding or scour is responsible worldwide for around 60% of the collapses as shown in figure (1-2).

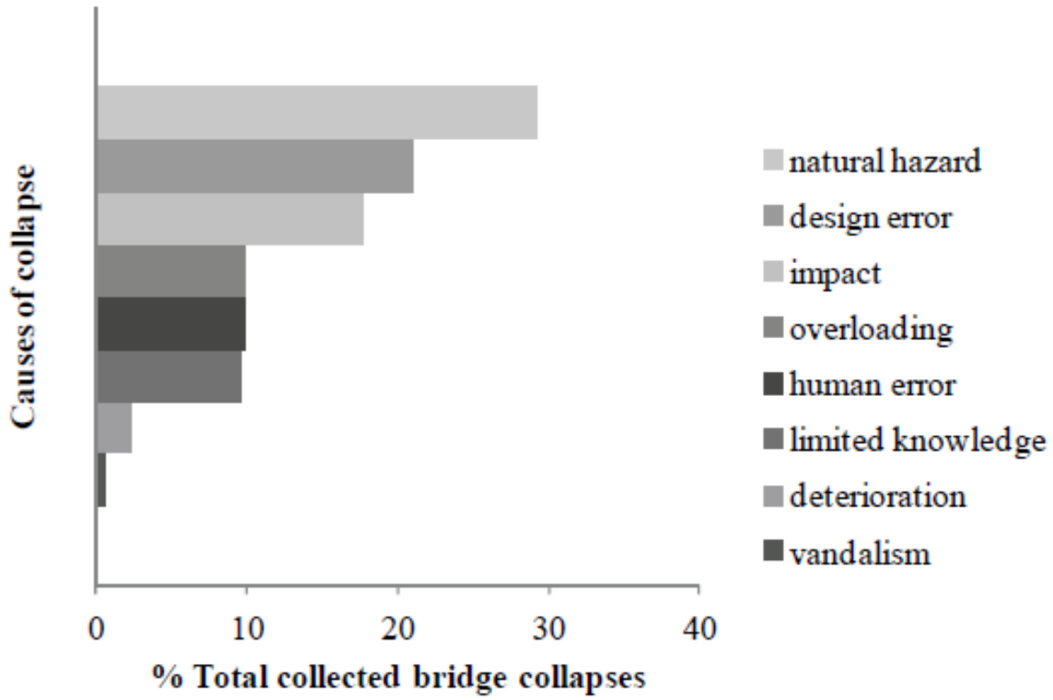

Figure (1- 1): Main causes of bridge collapse (Imhof, 2004).

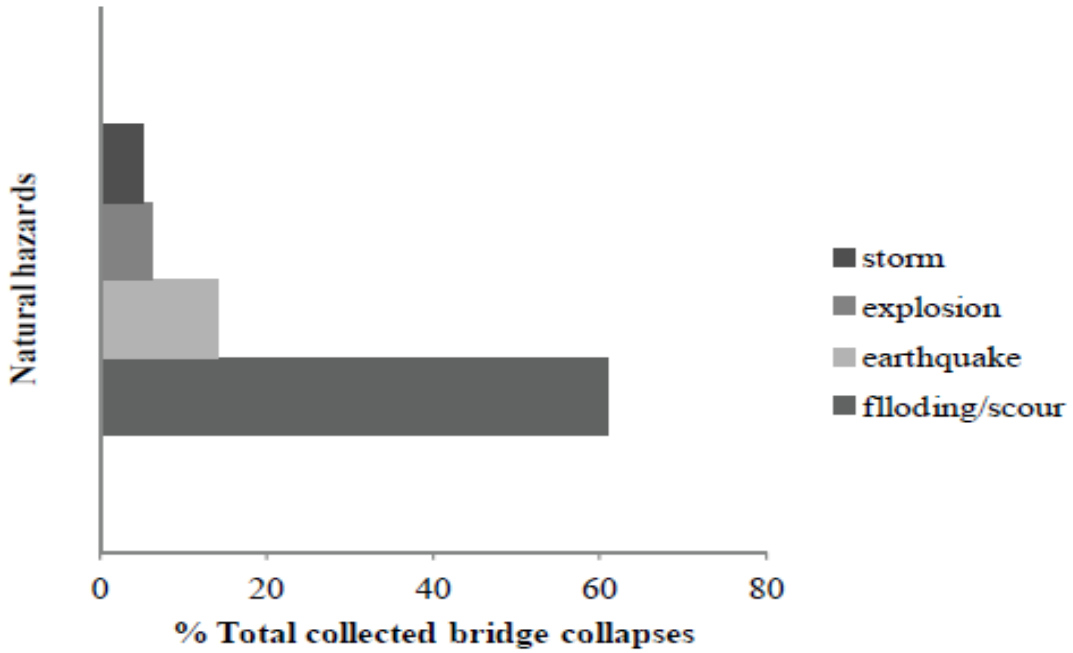

Figure (1- 2): Different natural hazards causing bridge collapse (Imhof, 2004).

In the United States more than 1,000 bridges have collapsed in the past 30 years, and 60% of failures occurred because of the processes of river hydraulics, including pier scour (Deng and Cai 2010). As Foti and Sabia (2011) noted, there are more than 26,000 bridges in the United States that have been identified as scour critical.

Bridge damage and failure have deep social and economic implications due to the costs of reconstruction, maintenance and monitoring of existing structures, the disruptions of traffic circulation and, in some extreme cases, the cost of human lives. In a wide research on bridge scour, the Federal Highway Administration (Brice and Blodgett, 1978) reported that damages to bridges and highways from major regional floods in 1964 and 1972 amounted to about US$100 million per event; in New Zealand a survey of roading authorities showed that scour caused by rivers results in roading expenditure of NZ$36 million per year (Macky, 1990).

Although the dynamic of bridge scouring is well known and several studies are available in the literature for interpreting the scour process and predicting the maximum scour depth (Graf, 1998; Melville and Coleman, 2000), over the past decades a number of bridge damages that occurred during river floods has shaken the scientific community and spurred engineers and researchers to improve scour prediction models and to renew scour measurement techniques (Brandimarte et al. 2012). Indeed, by looking at the database collected by Imhof (2004), one can notice that the percentage of collapsed bridge has increased in the past decades as illustrated in table (1-1): while collapses due to limited knowledge or design error have decreased in time, those due to natural hazards have increased.

BRIDGE COLLPASE CAUSES	***All bridges (237)***	***Before 1900 (35)***	***1900-1940 (27)***	***1941-1990 (117)***	***1991-2004 (58)***
Natural hazards	40	31	37	37	50
Limited knowledge	9	14	30	7	1
Design error	5	9	0	4	5
Overloading	14	26	4	14	14
Impact	25	17	29	30	19
Human error	3	0	0	2	7
Vandalism	1	3	0	0	2
Deterioration	3	0	0	6	2

Table (1- 1): Percentage of collapsed bridges over time (Imhof, 2004).

2. Sediment transport in open channel and bridge pier scour.

2.1 Sediment transport.

Sediment transport is a term used for the sediment load occur is rivers, streams, coastal areas and in many other fluid bodies. There are two types of sediment transport: bed load and suspended load, in which bed load characterizes the grains rolling along the bed while suspended load refers to grains in suspension.

2.1.1 Bed formation.

The bed form results from the drag force exerted by the bed on the fluid flow as well as the sediment motion induced by the flow onto the sediment grains. This interactive process is complex. In a simple approach, the predominant parameters which affect the bed form are the bed slope, the flow depth and velocity, the sediment size and particle fall velocity. At low velocities, the bed does not move. With increasing flow velocities, the inception of bed movement is reached, and the sediment bed begins to move.

The basic bed forms which may be encountered are the ripples, dunes, flat bed, standing waves and antidunes. At high flow velocities (e.g. mountain streams and torrents), chutes and step-pools may form. They consist of succession of chutes and free-falling nappes (i.e. supercritical flow) connected by pools where the flow is usually subcritical (Chanson,2004).

The typical bed forms are summarized in figure (2-1) and table (2-1). In table (2-1), column 3 indicates the migration direction of the bed forms. Ripples and dunes move in the downstream direction. Antidunes and step-pools are observed with supercritical flows and they migrate in the upstream flow direction.

In alluvial rives, dunes form with subcritical flow conditions only. Instead, antidunes exist in supercritical flow, as standing wave are characteristics of near critical flow.

Bed form (1)	Flow (2)	Bed form motion (3)	Comments (4)
Flat bed	No Flow (or $Fr \ll 1$)	NO	No sediment motion
Ripples	$Fr \ll 1$	D/S	Three-dimensional forms; observed also with air flows (e.g. sand ripples in a beach caused by wind)
Dunes	$Fr < 1$	D/S	Three-dimensional forms; sand dunes can also be caused by wind
Flat bed	$Fr \leq 1$	NO	Observed also with wind flow
Standing waves	$Fr = 1$	NO	Critical flow conditions; bed standing waves in phase with free-surface standing waves
Antidunes	$Fr > 1$	U/S	Supercritical flow with tumbling flow and hydraulic jump upstream of antidune crests
Chute-pools	$Fr > 1$	U/S	Very active antidunes
Step-pools	$Fr > 1$	–	Cascade of steps and pools; steps are often caused by rock bed

Table(2- 1): Basic bed forms in alluvial channels.(Henderson,1966 and Graf ,1971)

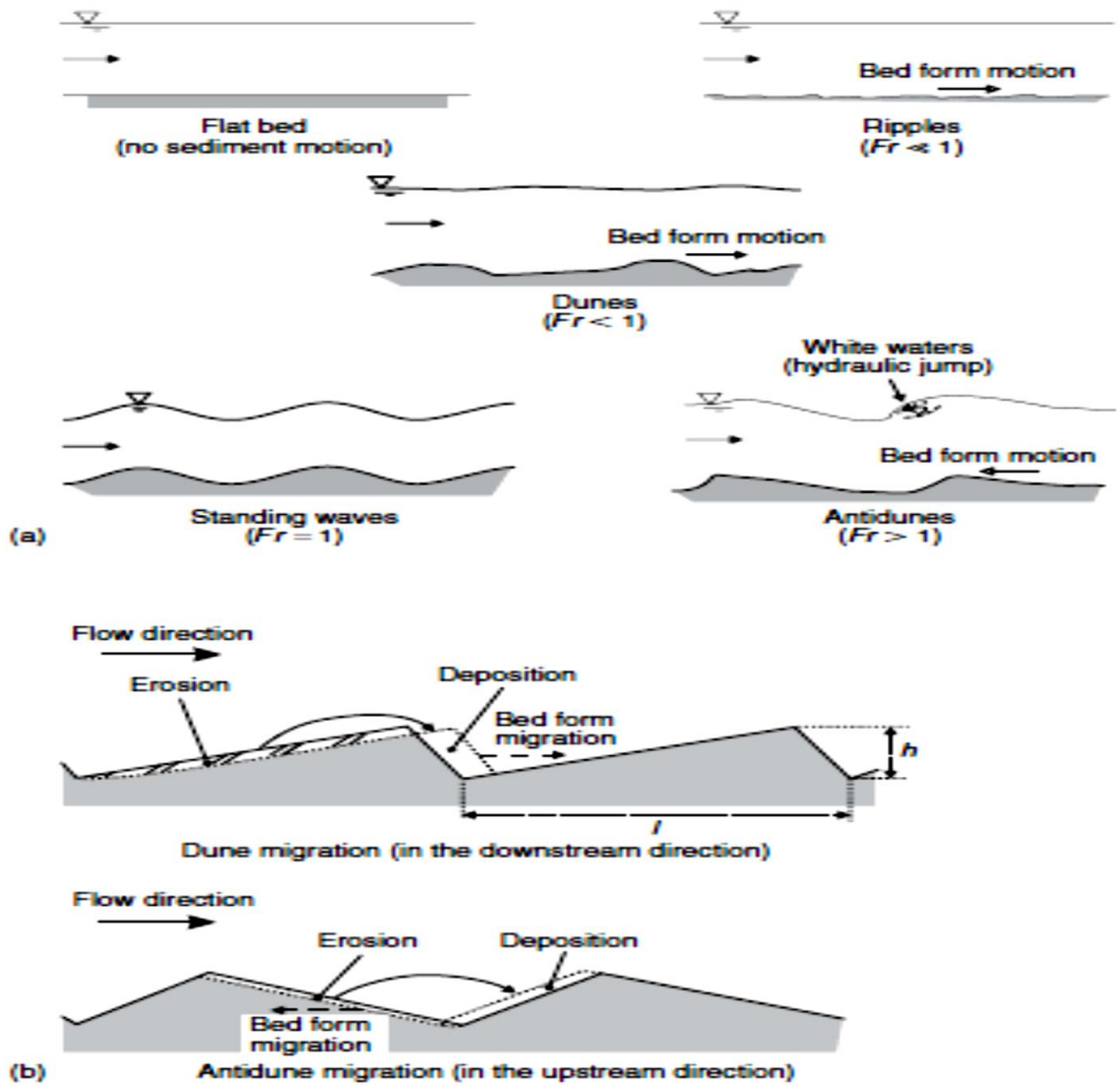

Figure(2- 1): Bed forms in movable boundary hydraulics: (a) typical bed forms and (b) bed form motion(Chanson,2004).

2.1.2 Physical properties of sediments.

There are two types of sediments; cohesive (e.g. clay and silt) and non-cohesive (e.g. sand and gravel). Sediments differentiate based on the relative density, and sediment size as shown in table (2-2).

The relative density equals: $$s = \frac{\rho_s}{\rho}$$

Where ρ_s is the sediment density and ρ is the fluid density.

Class name (1)	Size range (mm) (2)	Phi-scale (ϕ) (3)	Remarks (4)
Clay	$d_s < 0.002$ to 0.004 mm	$+8$ to $+9 < \phi$	
Silt	0.002 to $0.004 < d_s < 0.06$ mm	$+4 < \phi < +8$ to $+9$	
Sand	$0.06 < d_s < 2.0$ mm	$-1 < \phi < +4$	Silica
Gravel	$2.0 < d_s < 64$ mm	$-6 < \phi < -1$	Rock fragments
Cobble	$64 < d_s < 256$ mm	$-8 < \phi < -6$	Original rocks
Boulder	$256 < d_s$	$\phi < -8$	Original rocks

Table(2- 2): Sediment size classification(Chanson,2004).

Several definitions of sediment size are available. The *sieve diameter* is the size of particle which passes through a square mesh sieve of given size but not through the next smallest size sieve: e.g. 1mm < d_s < 2mm. The *sedimentation diameter* is the size of a quartz sphere that settles down (in the same fluid) with the same settling velocity as the real sediment particle. The *nominal diameter* is the size of the sphere of same density and same mass as the actual particle(Chanson,2004).

Particle size distribution.

Natural sediments are mixtures of many different particle sizes and shapes. The particle size distribution is usually represented by a plot of the weight percentage of total sample, which is smaller than a given size plotted as a function of the particle size. The characteristic sediment size d_{50} is defined as the size for which 50% by weight of the material is finer. Similarly, the characteristic sizes d_{16} and d_{84} are values of grain sizes for which 16% and 84% of the material weight is finer, respectively.

The geometric standard deviation based upon a log-normal distribution of grain sizes σ_g, that imply the uniformity of the sediment size distribution, so higher σ_g means wider sediment size distribution.

$$\sigma_g = \sqrt{\frac{d_{84}}{d_{16}}}$$

A typical particle distribution curve is shown in figure (2-2) that represents percentage sampling as a function of sedimentological size parameter Φ and cumulative percentage passing as a function of the particle size d_s.

As the sedimentological size parameter Φ is expressed as following:

$$\phi = -\frac{\ln(d_s)}{\ln(2)}$$

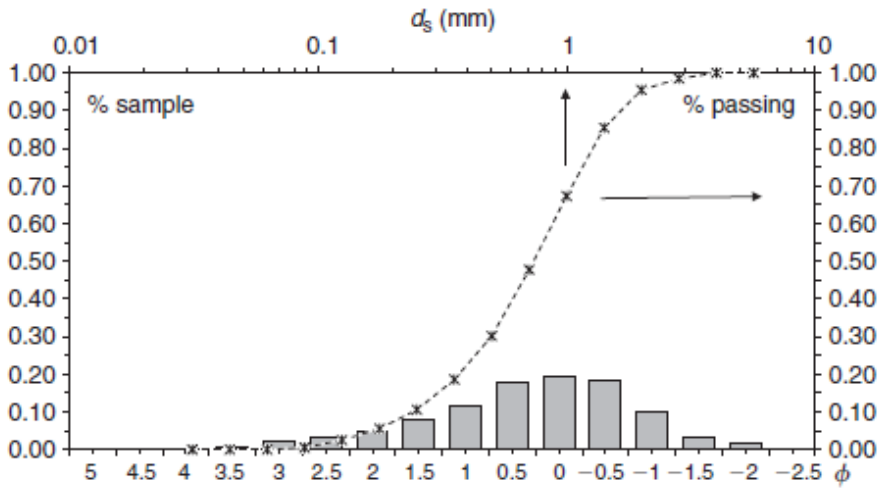

Figure (2- 2): Sediment size distribution sample(Chanson,2004).

Angle of repose.

Considering the stability of a single particle in a horizontal plane, the threshold condition (for motion) is achieved when the center of gravity of the particle is vertically above the point of contact. The critical angle at which motion occurs is called the angle of repose Φ_s. The angle of repose is a function of the particle shape and, on a flat surface, it increases with angularity. The angle of repose ranges usually from 26° to 42°, and for sands, Φ_s is typically between 26° and 34°(Chanson,2004).

Figure (2-3) shows typical examples of angle of repose for different shapes of sediment particles.

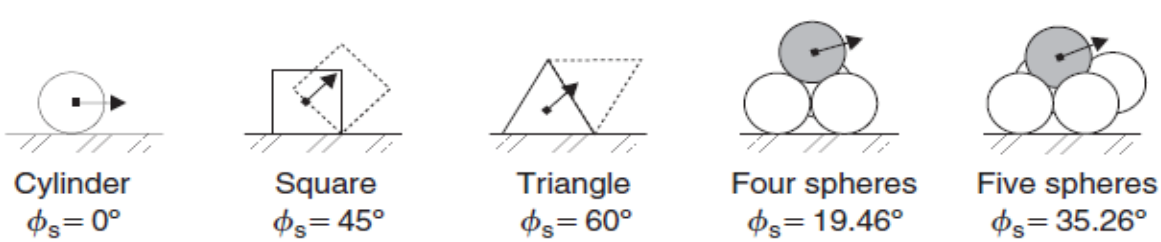

Figure (2- 3): Examples of angle of repose(Chanson,2004).

2.1.3 Bed load transport.

Threshold of sediment bed motion

The condition at which the sediment particles start to move from still. In practice, bed load transport starts occurring at lower velocities than sediment suspension, for a given bed geometry and particle size distribution.

For an open channel flow with a movable bed, the forces acting on each sediment particle are figure (2-4):

_ the gravity force $=\rho_s g v_s$,

_ the buoyancy force $F_b = \rho g v_s$,

_ the drag force $C_d=A_s V^2/2$,

_ the lift force $C_L=A_s V^2/2$,

_ the reaction forces of the surrounding grains,

where v_s is the volume of the particle, A_s is a characteristic particle cross-sectional area, C_d and C_L are the drag and lift coefficients, respectively, and V is a characteristic velocity next to the channel bed.

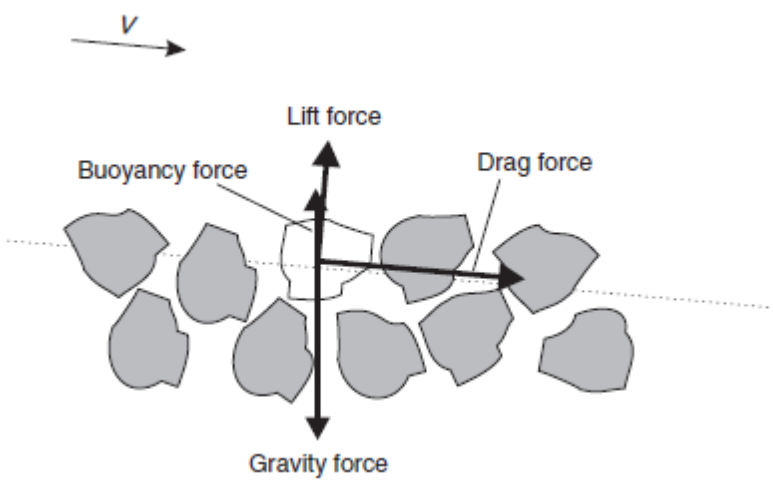

Figure (2- 4): Forces acting on a sediment particle (Chanson,2004).

The gravity force and the buoyancy force act both in the vertical direction, while the drag force acts in the flow direction and the lift force in the direction perpendicular to the flow direction. The inter-granular forces are related to the grain disposition and packing (Chanson,2004).

It is difficult to define the exact threshold with absolute precision. Many experimental observations, however, have provided reasonably accurate and consistent results.

The relevant parameters for the analysis of sediment transport threshold in dimensionless terms:

$$f_2\left(\frac{\tau_0}{\rho g d_s};\ \frac{\rho_s}{\rho};\ \frac{d_s\sqrt{\rho\tau_0}}{\mu}\right)=0$$

The bed shear stress T_o, the sediment density ρ_s, the fluid density ρ, the grain diameter d_s, the gravity acceleration g and the fluid viscosity μ(Chanson,2004):

The shear velocity can be defined as:

$$V_* = \sqrt{\frac{\tau_0}{\rho}}$$

Therefore, the previous equation can be transformed as:

$$f_3\left(\frac{V_*}{\sqrt{g d_s}};\ \frac{\rho_s}{\rho};\ \rho\frac{d_s V_*}{\mu}\right)=0$$

Particle movement occurs when the moments of the destabilizing forces (i.e. drag, lift and buoyancy), with respect to the point of contact, become larger than the stabilizing moment of the weight force. The resulting condition is a function of the angle of repose.

Experimental observations highlighted the importance of the stability parameter T*(which may be derived from dimensional analysis) defined as:

$$\tau_* = \frac{\tau_0}{\rho(s-1)g d_s} \qquad \tau_0 = \rho g R_H S_{f,skin} \qquad S_{f,skin} = \frac{n_{skin}^{\ 2}\cdot V^2}{R_H^{\ 4/3}} \qquad n_{skin} = \frac{d_{90}^{\ 1/6}}{26}$$

In summary: the initiation of bed load transport occurs when the bed shear stress τ_0 is larger than a critical value:

$$(\tau_0)_c = \rho(s-1)g d_s(\tau_*)_c$$

It is worth noting also that, for sediment particles in water as in figure (2-5), the Shields diagram exhibits different trends corresponding to different turbulent flow regimes:

_ the smooth turbulent flow (Re*< 4–5) 0.035 <(T *)c,

_ the transition regime (4–5 <Re*<75–100) 0.03 <(T *)c < 0.04,

_ the fully rough turbulent flow (75–100< Re*) 0.03 <(T *)c <0.06.

For fully rough turbulent flows, the critical Shields parameter (T*)c is nearly constant, and the critical bed shear stress for bed load motion becomes linearly proportional to the sediment size(Chanson,2004).

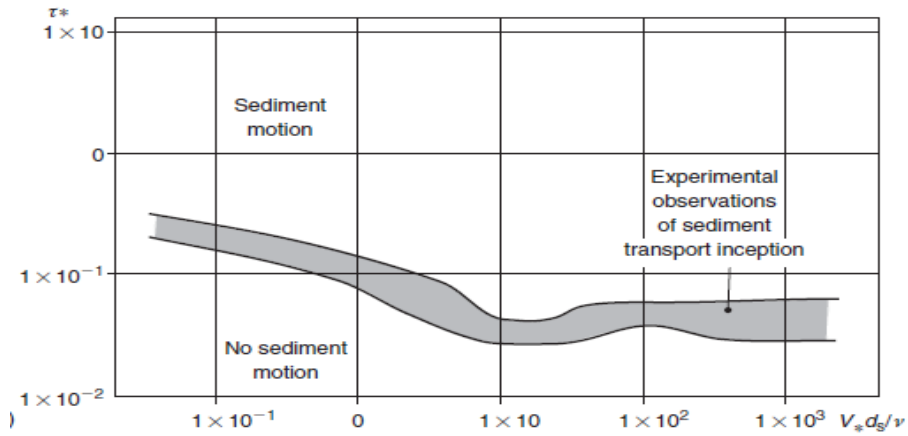

Figure (2- 5): Shields parameter as a function of the particle Reynolds number for sediment in water (Chanson,2004).

Sediment bed motion

Figure (2-6) bed transport mechanism when the bed shear stress exceeds the critical value. For bed-load transport, the basic modes of particle motion are *rolling motion*, *sliding motion* and *saltation motion* (the transport of sediment particles in a series of irregular jumps and bounces along the bed).

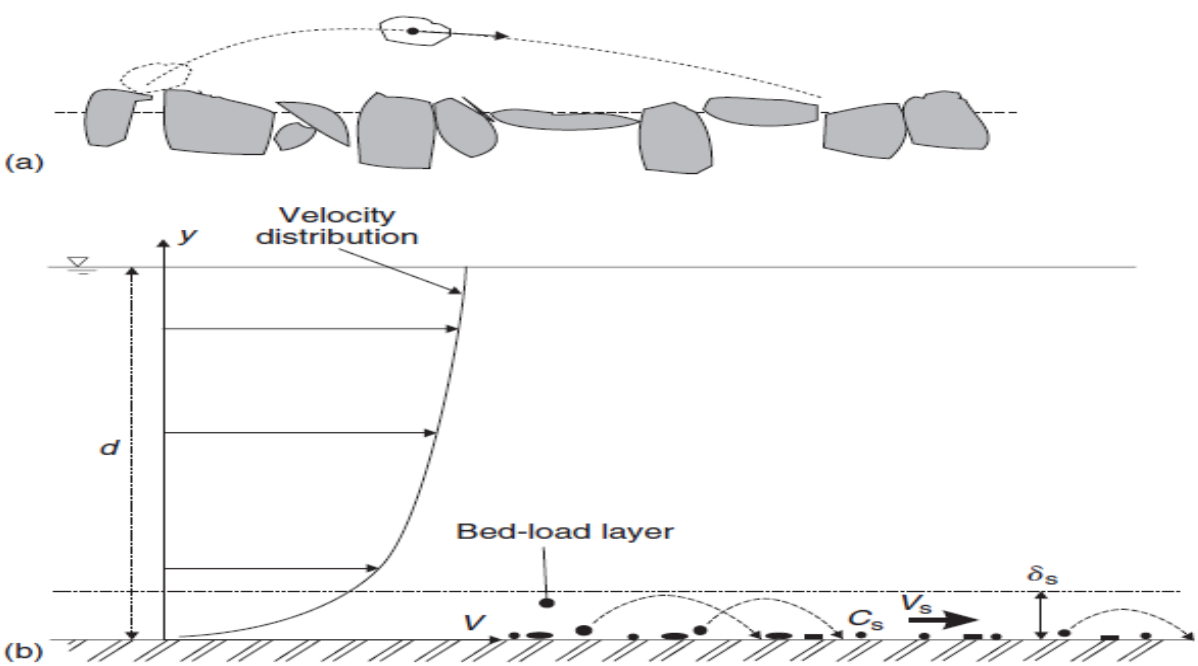

Figure (2- 6): Bed-load motion: (a) sketch of saltation motion and (b) definition sketch of the bed-load layer(Chanson,2004).

The sediment transport rate is often expressed by meter width and is measured either by mass or by volume(Chanson,2004):

$$\dot{m}_s = \rho_s q_s$$

Where $\acute{m}_s$ is the mass sediment flow rate per unite width, ρ_s is the volumetric sediment discharge per unit width and q_s is the specific mass of sediment. In case of exceeding the threshold, the bed load is induced and calculated based on the shear stress value.

2.2 Pier scour.

Scour at bridge crossings is the result of the erosive action of flowing water, when it has the strength to excavate and carry away material from around bridge piers and bridge abutments (Richardson and Davis, 2001). Scour depth is the lowering of the river bed level and is a measure of the tendency to expose bridge foundations (Melville and Coleman, 2000).

2.2.1 Local scour

In the presence of bridge crossings, additional scour (known as Local Scour) is induced by the local change of cross-section geometry due to the presence of the bridge. Local scour results from the removal of material from around piers, abutments, embankments as a consequence of the flow alteration induced by the obstruction of the flow (Richardson and Davis, 2001).

The presence of a bridge structure in a flow channel inevitably involves a significant change to the flow pattern, which in turns induces changes to the stream bed elevation. Flow changes due to bridge piers results in the formation of a scour hole at the piers, which has been recognized by several studies (Melville and Coleman, 2000; Richardson and Davis, 2001) responsible for pier undermining and thus for pier damage or failure. The dominant feature of the flow near a pier is the system of vortices that develops around the pier when unidirectional flow in erodible channel becomes three-dimensional (Graf, 1998; Melville and Coleman, 2000; Shen et al., 1969). Depending on bridge geometry and flow conditions, the system of vortices can be composed by all, any or none of three individual basic systems acting at the pier as shown in figure (2-7): a) the horse-vortex system at the base of the pier; b) the wake-vortex system downstream of the pier; c) the surface roller ahead of the pier.

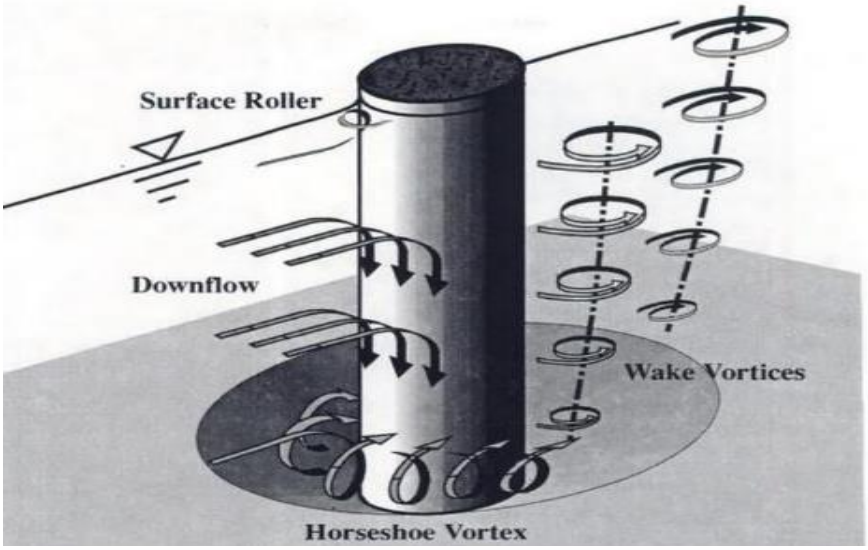

Figure (2- 7): Sketch of the system of vortices at a bridge pier (Melville and Coleman, 2000).

The horseshoe-vortex is due to the vertical component of a downward flow, namely from high to low velocities, observed in front of the pier as a result of the stagnating pressure gradient, as the flow approaches the pier (Raudkvi, 1991). Although the downward flow will be laterally diverted by a pressure gradient around the pier, it is generally agreed upon that it is the vertical component of the flow the one responsible for removing bed material (Graf, 1998). Due to the stagnation pressure, the water surface, in upstream of the pier, increases resulting in a surface roller.

If the pressure field is sufficiently strong, it induces a three-dimensional separation of the boundary layer and the horse-vortex system forms itself at the base of the pier (Graf, 1998; Shen et al., 1969). The downward flow impinging on the bed acts like a vertical jet in eroding a groove immediately adjacent to the front of the pier (Melville and Coleman, 2000). the wake-vortex system is generated due to the rolling up of unstable shear layers at the surface of the pier (Shen et al., 1969). The wake vortices arise from either side of the pier at the separation line and are transported downstream by the flow.

Shen et al. (1969) noticed that this vortex system is stable for low Reynolds numbers (3 to 5 $<R_e<$40 to 50) and form a standing system downstream of the pier; however, for Reynolds number of practical interests, the wake vortices become unstable, are shed alternately from the pier and are translated downstream. The wake-vortex system acts like a vacuum cleaner sucking up stream bed material and transporting downstream of the pier the sediment moved by the downward flow and by the horse-vortex system (Melville and Coleman, 2000). The intensity of the wake vortices decreases rapidly as

the distance downstream of the pier increases: this often results in sediment deposition downstream of a long pier (Richardson and Davis, 2001).

2.2.2 Clear-water and live bed scour.

Local scour depends on the balance between streambed erosion and sediment deposition. To this end two different scour regimes have been defined, namely clear-water scour and live-bed scour. In the former case no sediments are delivered by the river. In the latter case an interaction exists between sediment transport and scour processes, due to bed material being transported from the upstream reach into the crossing.

Moreover, a different evolution in hole scouring is expected: in clear water, the scour depth increases slowly and tends to reach a stable solution; in live bed conditions, the scour depth increases rapidly and, due to the interaction between erosion and deposition, it tends to fluctuate around an equilibrium vale (Brath and Montanari, 2000; Richardson and Davis, 2001). Figure (2-8) shows the scour evolution in clear-water and live-bed conditions.

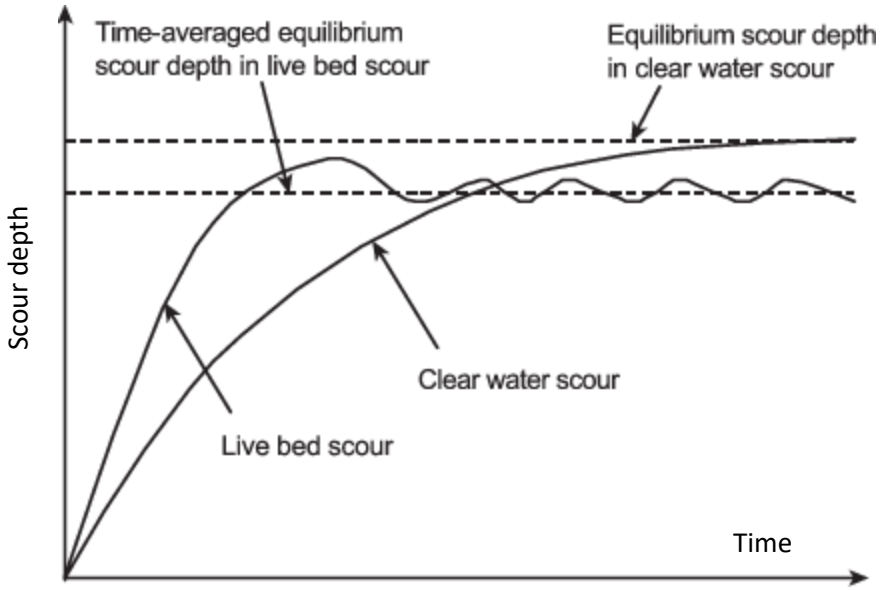

Figure (2- 8): Time evolution of scour depth in clear-water and live-bed conditions (Brandimarte et al,2012).

In order to assess whether scour is clear water or live-bed, a motion criterion can be used (Melville and Coleman, 2000), with reference to the d_{50}, mean diameter representative of the soil particle distribution. By comparing the mean velocity upstream of the bridge, V, with the critical velocity, Vc, of the d_{50} bed material, scour conditions will be:

Clear water $\frac{V}{V_c} \leq 1$

Live-bed $\frac{V}{V_c} > 1$

Factors affecting the scour depth

Factors which affect the magnitude of local scour at piers and abutments are (1) width of the pier/abutment, (1) length of the pier/abutment if skewed to flow, (3) depth of flow, (4) velocity of the approach flow, (5) size and gradation of bed material, (6) angle of attack of the approach flow to a pier or abutment, (7) shape of a pier or abutment, (8) bed configuration, and (9) ice formation or jams, and debris.

The dimensionless scour depth at a circular bridge pier with uniform sediment is expressed by a function:

$$\frac{Sd}{b} = F\left(\frac{h}{b}, \frac{b}{B}, \frac{h}{d}, \frac{Q}{Q_c}, \frac{tV}{b}\right) \qquad \textbf{(I)}$$

where symbols that were not defined previously are: ds = scour depth; 110 b = pier diameter; h = water height; B = channel width; t = time; V = flow velocity. The control parameters on the right-hand side of eq. (I) denote, respectively, the effect of pier slenderness, flow contraction, sediment coarseness, flow intensity, and dimensionless time (Radice and Lauva,2017).

2.2.3 Steady-flow scour studies.

Many studies have been performed to explore the dependency of the scour depth on different parameters in steady conditions (e.g. Chiew and Melville,1987; Chang et al, 2004), some of those experiments with their results are highlighted here:

1) *Scour depth sensitivity to approaching velocity, sediment size and water depth was carried out by Chiew and Melville (1987).*

Three empirical functions which relate equilibrium scour depth with approach velocity, sediment size and flow depth were obtained (Chiew and Melville,1984).

Cylindrical piers made from clear perspex tubes were used for the experiments. Five different sized, non-cohesive as presented in table (2-3), uniform sediments were selected for the experiments. For each sediment size, three different sized piers with size b, equal to 31.8 mm (1.3 in.), 40 mm (1.6 in.) and 45 mm (1.8 in.) were investigated.

mean particle size, in millimeters (inches)	specific gravity	critical shear velocity, in metres per second (feet per second)	critical mean velocity, in metres per second (feet per second)	geometric standard deviation
0.24 (9.45×10^{-3})	2.65	0.013 (0.041)	0.27 (0.89)	1.33
0.60 (2.36×10^{-2})	2.65	0.019 (0.062)	0.34 (1.12)	1.18
0.85 (3.35×10^{-2})	2.65	0.022 (0.072)	0.39 (1.28)	1.23
1.45 (5.71×10^{-2})	2.65	0.028 (0.092)	0.45 (1.48)	1.24
3.20 (1.26×10^{-1})	2.65	0.049 (0.161)	0.73 (2.39)	1.28

Table (2- 3): Properties of sediments used in experiments (Chiew and Melville,1984).

Knowing that Sd is the average scour depth, b is the pier diameter, V is the mean approaching velocity, V_c is the critical velocity for d_{50}, sediment size, and yo is the flow depth. The study deduced that When the relative equilibrium scour depth, Sd/b, is plotted as a function of the velocity excess, V/V_c under the condition where the approach flows were subcritical and the Froude number less than unity, the results show an initial reduction in scour depth for condition just exceeding the threshold velocity of the bed sediment. The reduction continues until a minimum scour depth is reached at $V/V_c = 2$. Thereafter, the local scour depth increases again, but at a decreasing rate, until a second peak is reached at $V/V_c = 4$, which corresponds to the condition where transition flatbed is formed as shown in figure (2-9).

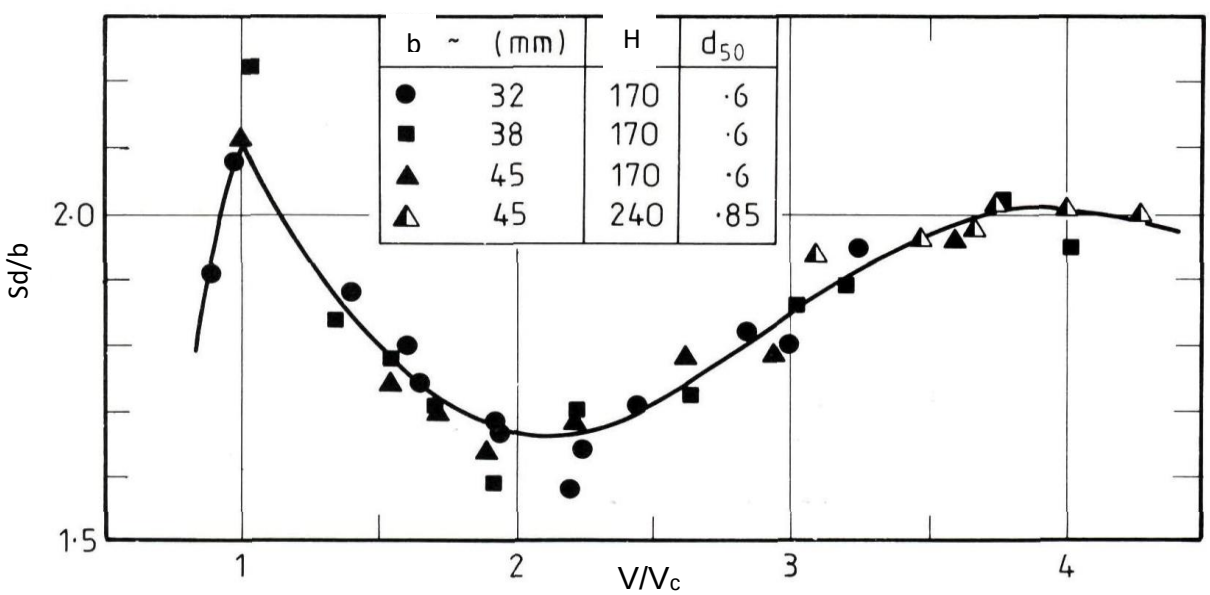

Figure (2- 9): Relative equilibrium scour depth, Sd\b versus velocity excess, V/V_c for d_{50} = 0.6 and 0.85 mm. (Chiew and Melville,1984).

The equilibrium scour depth is also dependent on the size of the bed sediment. Ettema (1980), for the case of clear-water scour, showed that the scour depth is influenced by the relative size of the pier to sediment, b/d_{50}. He concluded that the depth of scour is reduced with decreasing values of b/d_{50} and is independent of b/d_{50}, when b/d_{50} is greater than or equal to 50. Replots of Ettema's data and Chee's (1982) clear-water scour results are gathered together with live-bed scour results obtained from this study are shown in figure (2-10). Each curve shows the value of b/d_{50} increasing almost linearly with increasing value of b/d_{50} until a maximum at b/d_{50} equals to 50, indicating that the scour depth is independent of the relative size of the pier to sediment for b/d_{50} > 50 (Chiew and Melville, 1987).

Considering the effect of water depth, the decrease in scour depth in shallow flow is primarily due to the reduction in the strength of the downflow. This is because erosion of the scour hole is due to the momentum of fluid impinging as downflow at the base of the scour hole. In a shallow flow, this momentum is reduced resulting in a lesser scour hole.

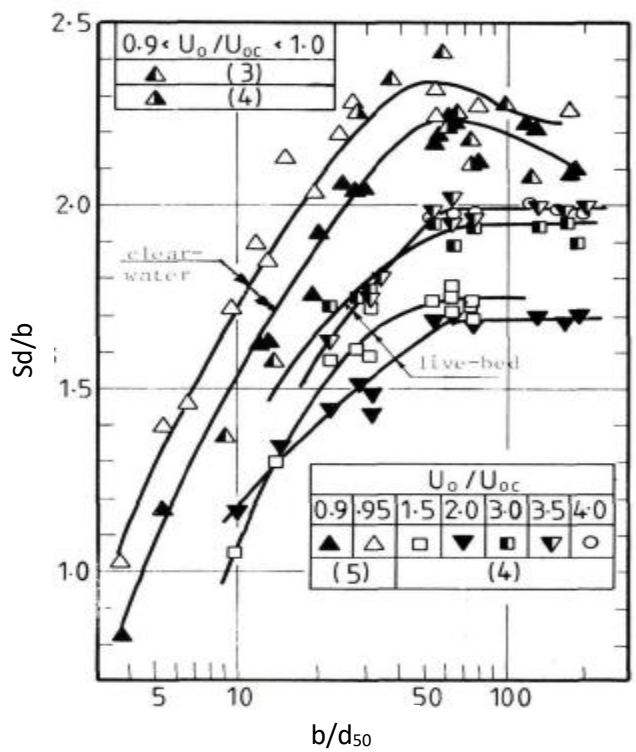

Figure (2- 10): Relative equilibrium scour depth versus D/d50 at various values of V/V_c. (Chiew and Melville,1984).

2) *A study done by Chang et al (2004) for clear water pier scour under steady conditions to explore the effect of sediment uniformity.*

The effects of sediment size gradation on the scour-depth evolution at a circular pier nose under clear-water scour condition have been investigated through laboratory

experiments and simulation model. Uniform sediments having sizes of 1.0 and 0.71 mm, and nonuniform sediments having the same median sizes with σ_g of 2.0 and 3.0, respectively, were used for experiments. All of these sediments had a specific gravity of 2.65.b is the diameter of the cylindrical pier (0.1) m and H is the flow depth. Table (2-4) lists the experimental conditions.

Run number	d_o (mm)	σ_g	H (mm)	V (cm/s)	t_d (h)	Sd/b
S1	1.00	1.2	20.0	39.0	19	1.86
S2	1.00	1.2	20.0	28.0	19	1.18
S3	1.00	2.0	20.0	28.0	56	0.43
S4	1.00	3.0	20.0	28.0	28	0.29
S5	0.71	1.2	30.0	35.5	7	1.54
S6	0.71	1.2	15.0	22.7	7	0.66
S7	0.71	2.0	30.0	35.5	72	0.83
S8	0.71	2.0	15.0	22.7	47	0.24
S9	0.71	3.0	30.0	35.5	38	0.68
S10	0.71	3.0	15.0	22.7	27	0.15

Table (2- 4): Experimental conditions (Chang et al,2004).

In a channel with a movable bed, the materials available for entrainment by flow running over them are those on and near the bed surface. The mixing layer refers to the layer from which the materials can be entrained by the flow. It can also be regarded as an active zone below which the bed material remains undisturbed. During the erosion of nonuniform sediment, fine grains tend to be scoured first, with the coarse grains left behind. Gradually, most of the finer grains are washed out of the active zone, and the bed materials covered by coarse grains become immobile, forming an armored layer to protect the underlying materials.

Considering all the experiments, the scour-depth evolution, as shown in figure (2-10), it can be seen that the scour rate is very high at the early stage of the scouring process, then decreasing quickly as the scour hole develops further. The experimental data are used to derive the time-dependent scour rate, expressed in discrete form as:

$$\frac{dD_s}{dT} = \frac{D_s(T+\Delta T) - D_s(T)}{\Delta T}$$

Where Ds(=Sd/b) dimensionless scour depth;Ds(T+ΔT) and Ds(T)=experimental values of Ds at times T+ΔT and T, respectively; T(=t/te) =normalized time; and te=equilibrium time of scour, which is defined as the time when the incremental scour depth in a succeeding 24-h period of experiment is less than 5% of the pier diameter (Melville and Chiew 1999).

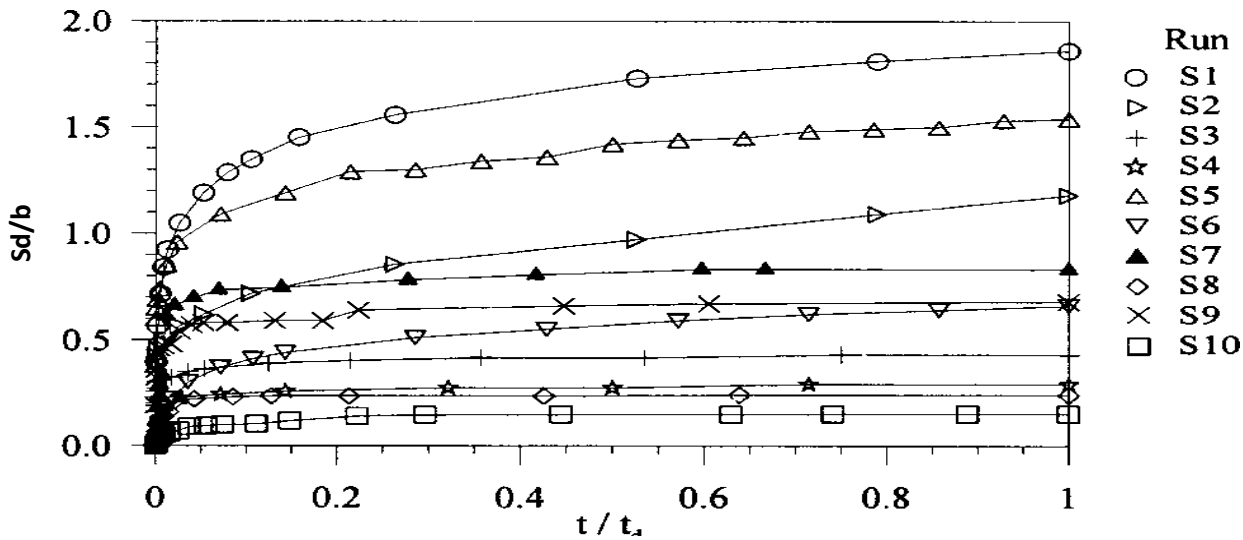

Figure (2- 11): Evolution of dimensionless scour depth at pier nose under steady flow (Chang et al,2004).

3) *A study of steady live-bed scour with measuring different values of scour depth (maximum, minimum and mean) performed by Ettmer et al (2015).*

Experiments on scour at bridge piers were carried out in a sediment recirculating flume with a bed of polystyrene particles. The focus of the research reported in this paper was given to live-bed experiments. All experiments were run until equilibrium conditions with flow velocities u ranging from 0.8–8.5 times the critical velocity for the incipient motion of sediment particles V_c. Maximum scour depth was continuously measured with an endoscopic camera from inside the pier, which was constructed by a plexiglass cylinder. Bed load transport with dunes was identified as the main transport mode for $1 < V/V_c < 4$. For ratios of $V/V_c \geq 4$ entrainment into suspension without development of bedforms dominated. Table (2-5) represents the experimental conditions where b is the pier diameter (7cm) and the critical velocity for the incipient motion of the sediment particles Vc was experimentally determined in preliminary runs to Vc=0.09 m/s.

1	2	3	4	5	6	7	8
Number	t (min)	u (m/s)	F (dimensionless)	u/u_c (dimensionless)	y_{max}/D (dimensionless)	y_{min}/D (dimensionless)	$y_{average}/D$ (dimensionless)
S1	360	0.072	0.069	0.80	0.81	0.81	0.81
S2	360	0.077	0.074	0.85	1.10	1.10	1.10
S3	360	0.081	0.078	0.90	1.23	1.23	1.23
S4	360	0.086	0.082	0.95	1.34	1.34	1.34
S5	360	0.090	0.087	1.00	1.51	1.51	1.51
S6	60	0.135	0.130	1.50	1.67	1.31	1.54
S7	60	0.180	0.173	2.00	1.77	1.09	1.48
S8	60	0.225	0.217	2.50	1.96	1.53	1.79
S9	60	0.270	0.260	3.00	2.26	1.79	2.07
S10	60	0.315	0.303	3.50	2.37	1.97	2.22
S11	60	0.360	0.347	4.00	2.51	2.13	2.40
S12	60	0.405	0.390	4.50	2.64	2.44	2.57
S13	60	0.450	0.433	5.00	2.84	2.59	2.73
S14	60	0.495	0.477	5.50	3.01	2.73	2.88
S15	60	0.540	0.520	6.00	3.09	2.84	2.99
S16	60	0.585	0.563	6.50	3.21	2.99	3.10
S17	60	0.630	0.606	7.00	3.23	2.99	3.15
S18	60	0.675	0.650	7.50	3.29	2.94	3.18
S19	60	0.720	0.693	8.00	3.29	3.00	3.21
S20	60	0.765	0.736	8.50	3.33	2.99	3.22

Note: Flow depth was $h = 0.11$ m during all runs.

Table (2- 5): experimental conditions (Chang et al,2004).

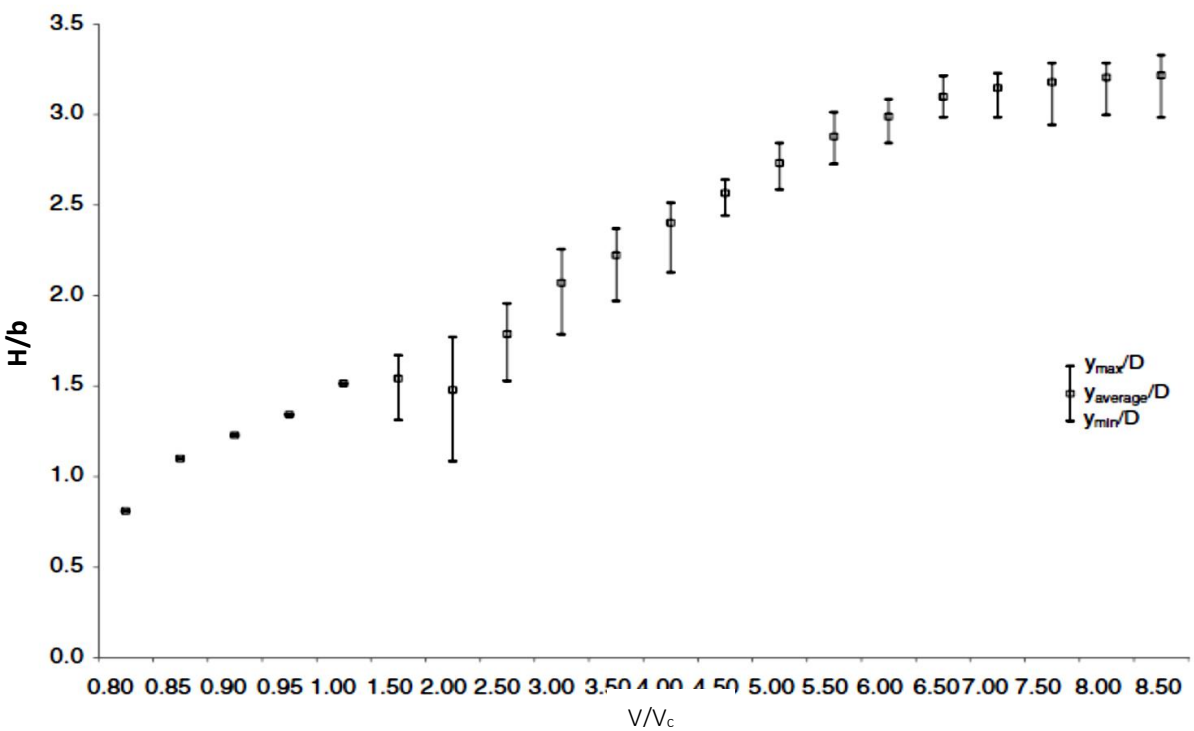

Figure (2- 12): Measured equilibrium scour depth H/b over flow intensity V/Vc (Ettmer et al, 2015).

Figure (2-11) shows equilibrium scour depth Sd/b over flow intensity V/V_c. The fluctuation of scour depth for $V/V_c > 1$ is additionally plotted as minimum and maximum value. For $V/V_c < 1$ minimum, averaged and maximum scour depths coincided and increased with flow intensity up to a peak by $V/V_c=1$. For $1 < V/V_c < 2$ average scour depth decreased with flow intensity until a local minimum and increased continuously for $V/V_c > 2$. The same tendency is observed in the context of the minimum scour depth. In contrast, maximum scour depths increased continuously with flow intensity for $V/V_c > 1$ reaching its highest value of 3.33 at $V/V_c = 8.5$. These value is significantly higher than the clear-water scour depth equal 1.51 observed at u/uc =1.0. Minimum and average scour depths exhibit a local minimum at $V/V_c =2.0$ and an envelope curve of those minimum and average equilibrium depths coincides well with results of previous investigations, i.e., Melville and Coleman,2000). Furthermore, it was detected that under bed-load conditions with $1 < V/V_c < 4$ the maximum scour depth was approximately 10–20% deeper than the average, while for $V/V_c \geq 4$ maximum scour depths were approximately 5% deeper than the average. That results accords well with results by Richardson and Davis (2001) who remark that maximum scour depth under sediment transport conditions can be significantly deeper than under clear-water conditions.

2.2.4 Unsteady-flow clear-water scour studies.

Few experiments have been carried out to explore the behavior of scour depth associated with imposed flow pattern that simulates the reality. Even though, most of the experiments were performed in clear-water conditions. Herein some of experimental campaigns descriptions and results that enlighten the effect of flow hydrograph on the scour depth evolution and variation.

1) *Experiments of bridge pier scour are carried out by Chang et al (2004) under steady and unsteady clear-water scour conditions with uniform and nonuniform sediments.*

the same sediment size and characteristics as well as pier diameter are used as previously mentioned in steady conditions. Furthermore, the hydrographs of unsteady flow for Runs U1– U13 listed in table (2-6) are shown in figure (2-12). The bed slope of the flume was kept constant during each run of unsteady flow experiments. The prescribed stepwise discharge and its corresponding depth were controlled by adjusting the inlet valve and tailgate. Runs U1, U2, and U3 were designed to investigate the effect of peak-flow velocity V_p (=35.5, 33.1, and 29.2 cm/s, respectively); and Runs U1, U4, and U5 were designed to investigate the effect of time to peak flow t_p (=2.5, 3.5, and 4.5 h, respectively).

Run number	d_o (mm)	σ_g	H (mm)	V (cm/s)	t_d (h)	Sd/b
U1	0.71	1.2	15.0–30.0	22.7–35.5	7	1.39
U2	0.71	1.2	15.0–25.0	22.7–33.1	7	1.25
U3	0.71	1.2	15.0–20.0	22.7–29.2	7	1.06
U4	0.71	1.2	15.0–30.0	22.7–35.5	7	1.42
U5	0.71	1.2	15.0–30.0	22.7–35.5	7	1.40
U6	0.71	2.0	15.0–30.0	22.7–35.5	7	0.76
U7	0.71	2.0	15.0–25.0	22.7–33.1	7	0.64
U8	0.71	2.0	15.0–20.0	22.7–29.2	7	0.39
U9	0.71	2.0	15.0–30.0	22.7–35.5	7	0.82
U10	0.71	3.0	15.0–30.0	22.7–35.5	7	0.58
U11	0.71	3.0	15.0–25.0	22.7–33.1	7	0.38
U12	0.71	3.0	15.0–20.0	22.7–29.2	7	0.20
U13	0.71	3.0	15.0–30.0	22.7–35.5	7	0.59

Table (2- 6): Experimental Conditions for the unsteady conditions (Chang et al, 2004).

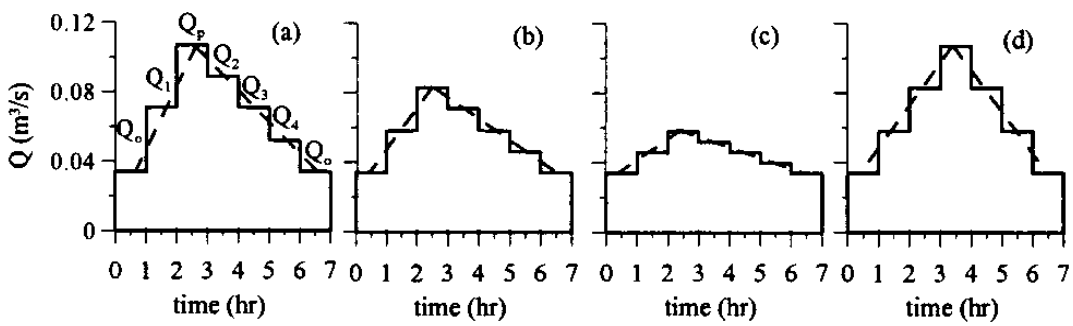

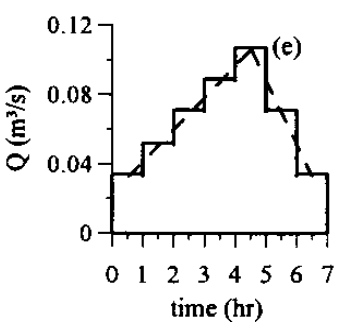

Graph	Run	V_o	V_1	V_2	V_3	V_4	V_p
(a)	U1,U6,U10	22.7	31.3	33.8	31.3	27.9	35.5
(b)	U2,U7,U11	22.7	29.2	31.3	29.2	26.4	33.1
(c)	U3,U8,U12	22.7	26.4	27.9	26.4	24.7	29.2
(d)	U4	22.7	29.2	33.1	33.1	29.2	35.5
(e)	U5,U9,U13	22.7	27.9	31.3	33.8	31.3	35.5

unit : cm / s

Figure (2- 13): Stepwise hydrographs for Runs U1–U13 (Chang et al, 2004).

In the unsteady flow experiments, general observations show that the scour depth increases steadily during the rising period of the hydrograph, and changes only slightly during the recession period as shown in figure (2-13) In Runs U1, U4, and U5 with the same peak-flow velocity V_p of 35.5 cm/s, but different t_p , the scour depths developed at the end of peak-flow discharge ranged from 92.8 to 98.6% of those at the end of the hydrograph, with t_p increasing from 2.5 to 4.5 h. This indicates that the influence of tp on scour depth is not of great importance. In Runs U1, U2, and U3 with the same tp of 2.5 h, but different V_p, the results showed that there was an increase of scour depth of 31% with V_p increasing by 22%. This reveals that Vp plays a much more important role than t_p in affecting the development of scour depth.

In addition, careful observations of the scouring processes indicate that the scour rate increases significantly as the discharge changes to a higher value. From the scour-depth evolution shown in figure (2-13), one can see that the scour depth increases rapidly after stepwise increase in discharge. With close examination, the scour-depth evolution for uniform sediment under a given segment of the stepwise hydrograph is quite similar to that under steady flow having the same discharge.

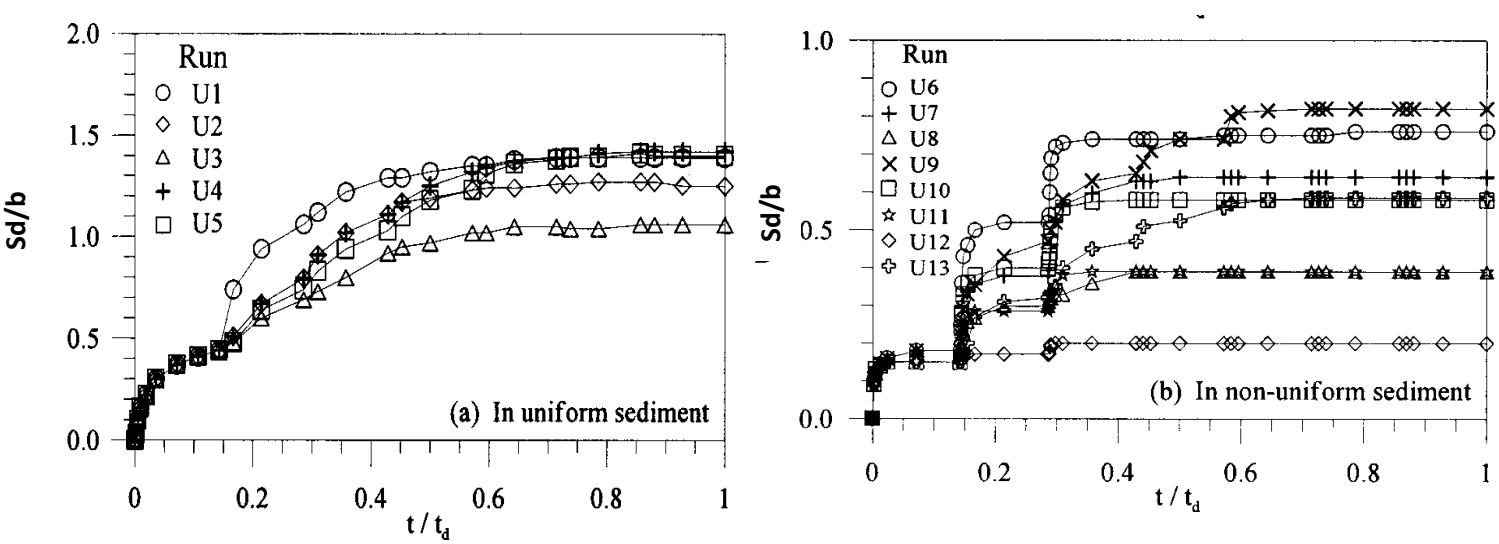

Figure (2- 14): Evolution of dimensionless scour depth at pier nose under stepwise hydrograph (Chang et al, 2004).

2) *An estimation of scour depth evolution and final value has been done by Lopez et al (2014) under the condition of clear-water by applying a flood wave.*

The sediment is characterized by a median grain size d_{50}=1.65 mm, a standard deviation of sediment grain distribution σ_g= 1.32, and specific gravity, ρs/ρ= 2.65. A PVC cylindrical pier with a diameter b=0.09 m was located in the center of the working cross section (20m downstream from the water entrance). 10 unsteady experiments have been run representing seven symmetric stepwise hydrographs as shown in table

(2-12), where tp is the experimental time, Q is the discharge, H is the water depth, Ip is the peak flow intensity that is the ratio between the imposed velocity and the critical one, n is the number of hydrograph steps, Δt (h) is the step duration, and Sd (cm) is the final scour depth.

Run	t_p (h)	$Q_1, Q_2, \ldots, Q_p$ (l/s)	$h_1, h_2, \ldots, h_p$ (cm)	I_p	n	Δt (h)	Sd (cm)
U1a	4.500	40.6, 55.2, 69.2	18.3, 19.4, 20.4	0.82	5	1.00	12.51
U1b	4.250	40.3, 47.1, 55.2, 62.3, 70.1	18.0, 18.5, 19.1, 19.5, 20.1	0.85	9	0.50	12.34
U1c	4.125	38.4, 42.3, 45.5, 49.5, 54.1, 57.6, 61.0, 64.5, 68.8	17.8, 18.1, 18.4, 18.7, 19.0, 19.2, 19.4, 19.7, 20.0	0.84	17	0.25	12.08
U2a	2.250	42.6, 55.0, 69.7	17.9, 19.1, 20.0	0.85	5	0.50	11.31
U2b	2.125	40.4, 47.0, 55.0, 62.3, 69.8	17.9, 18.4, 19.0, 19.5, 20.1	0.85	9	0.25	11.16
U3	8.500	38.8, 46.1, 54.4, 61.1, 69.4	17.7, 18.2, 18.8, 19.3, 19.8	0.85	9	1.00	13.19
U4	1.125	39.2, 55.2, 70.2	18.0, 19.0, 20.1	0.85	5	0.25	10.74
U5	1.125	24.9, 39.8, 54.3	11.5, 14.7, 18.3	0.73	5	0.25	7.73
U6	0.750	24.9, 39.7, 54.0	11.3, 14.8, 18.2	0.73	5	0.17	7.41
U7	4.500	25.1, 39.8, 54.6	11.4, 14.7, 18.1	0.74	5	1.00	11.30

Table (2- 7): Conditions for Unsteady Tests (Lopez et al,2014).

Figure (2-14) shows the experimental scour depth evolution for an unsteady test together with the evolution of the scour depth under steady conditions for the flow discharges that correspond to each hydrograph step of the unsteady test. The agreement between both scour depths confirms the validity of the procedure proposed by Kothyari et al. (1992) and Chang et al. (2004).

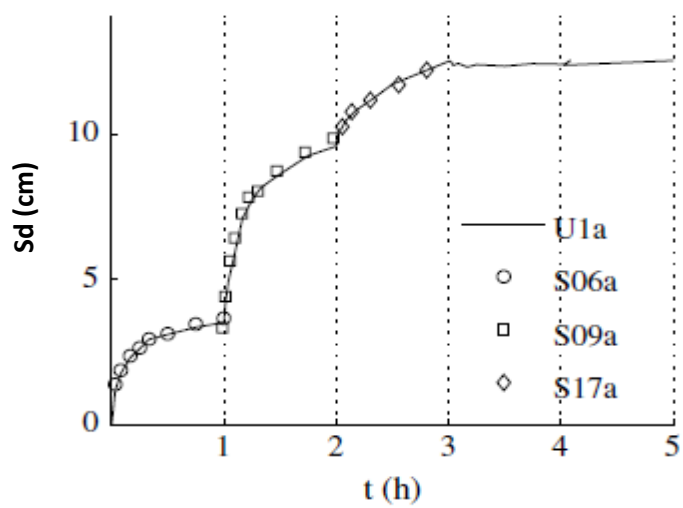

Figure (2- 15): Superposition of scour evolution under stepwise hydrograph (line) and steady flow conditions for each step (circles, squares, and diamonds) (Lopez et al,2014).

2.2.5 Conclusion of pier scour studies and motivation.

In conclusion, in steady conditions, the evolution of the scour depth is faster in live bed with more fluctuation compared to the clear-water conditions. At high velocities ($V/V_c>4$) (ettmer et al,2015), the scour depth fluctuation decreases as shown in figure (2-15). In unsteady condition, the scour depth increases during the rising limb with slight increase during the recession one. This is evident for clear-water as proved by many studies. However, in live-bed, the behavior of the scour depth evolution and variation is not deeply discovered and further exploring needed to enlighten the boundaries associated with the local scour phenomenon.

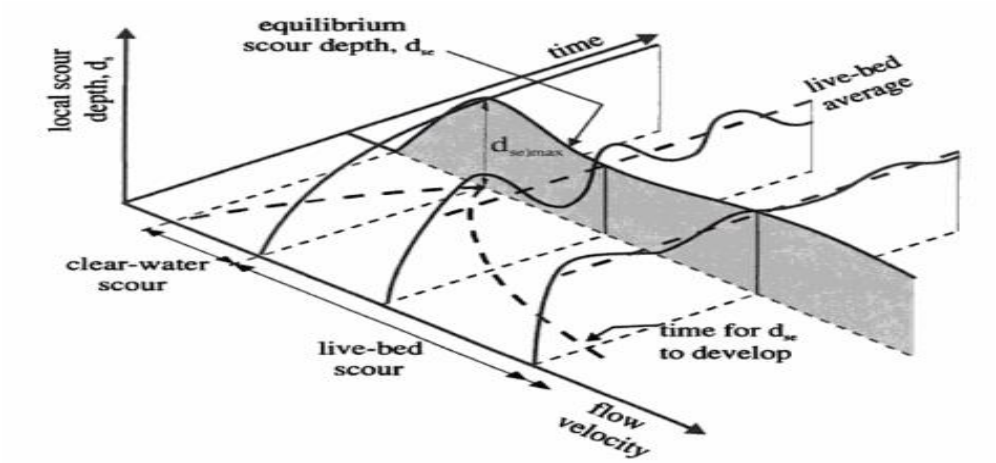

Figure (2- 16): The temporal scour depth fluctuation change with the flow velocity (Melville and Coleman,2000).

3. Laboratory Description.

The experimental work that reported here is performed in the Hydraulic Lab G.Fantoli that is located in the 4A Building inside the Leonardo Campus in the Politecnico di Milano (Milano, Italy) that shown in figures (3-1) and (3-2).

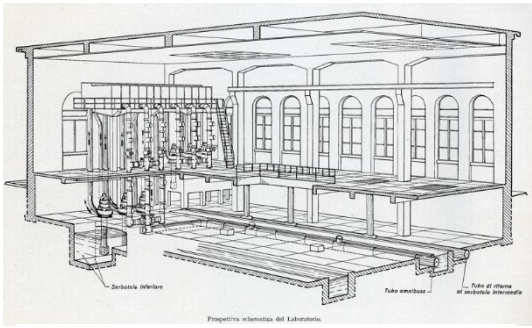

Figure (3- 2): Hydraulics laboratory

Figure (3- 1): Hydraulics laboratory

3.1 Experimental facilities.

channel.

The experiments were performed using a transparent pressurized duct with rectangular section. Dimensions of the duct were: length of 5.8 m, width of 0.40 m and height of 0.16 m. the channel sides were connected to the channel cover by steel bolts, as shown in figure (3-3).

Figure (3- 3): Experiment's channel

The installed system consists of many components attached together in order to satisfy the system functionality and the experimental campaign purpose. First, the flow is discharged from an underground storage tank by a submerged pump which feeds a tank that subsequently feeds the channel from upstream with the adequate flowrate; whilst, the live bed condition is satisfied by operating a fixed hopper upstream of the

channel to feed the channel with the designed sediment discharge (wither equilibrium or not) based on the water discharge and purpose of the experimental run. Moreover, water recirculating system has been installed in the laboratory; therefore, supposedly the water losses is significantly diminished. Additionally, the supplied sediment particles from upstream is ultimately trapped by a permeable in the downstream tank. Figure (3-4) represents a sketch for configuration of all components which are installed together.

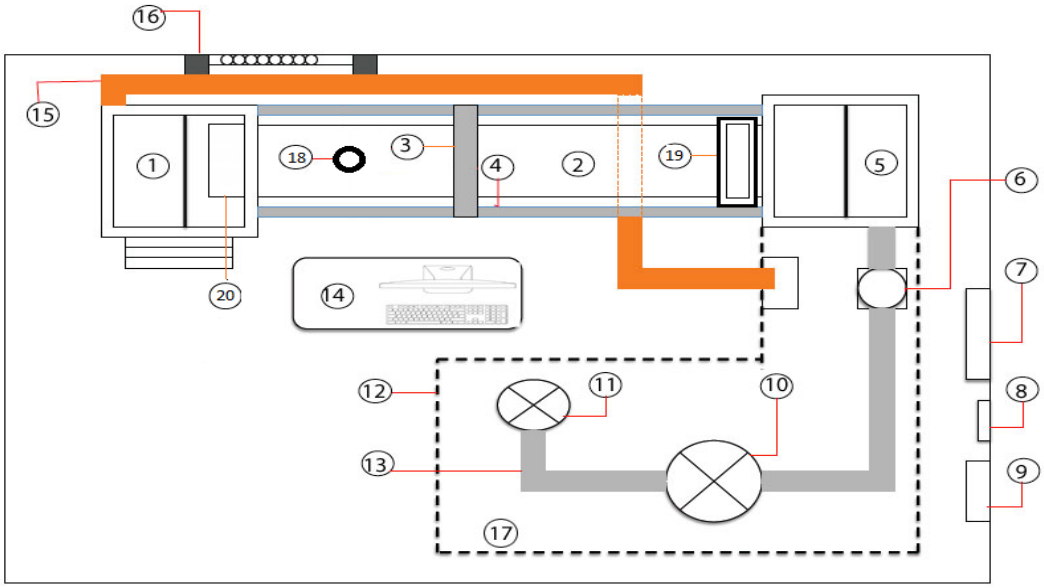

Figure (3- 4): Experiment's units plan sketch

1. The outlet Tank
2. A rectangular duct(channel)
3. Transverse positioning system
4. Longitudinal positioning system(roller)
5. The inlet Tank
6. Magnetic flow meter device
7. Hopper operator and time controller
8. Magnetic flow meter reader
9. Electric power controller
10. Main-stream Valve
11. By-pass Valve
12. Pumping and water discharge control unit.
13. inlet-Pipe
14. Desktop-PC
15. outlet Plastic pipe to recirculate water
16. Gauges and piezometers (aren't used in the present study)

17. underground Water Storage
18. Cylindrical Pier.
19. Hopper for sediment feeding.
20. sediment's trap basket.

3.1.1 water discharge measurements and components.

The flow rate Q is measured by an electro-magnetic flowmeter installed on the supply pipe that discharges water in the upstream tank. The channel inlet is rounded and a 0.3-m long first reach is equipped with a flow straightener made by an array pipes with a diameter of 1.6 cm.

The inlet units, as in figures (3-5), (3-6) and (3-7), consist of an underground storage tank which is the source of flow discharged to the inlet tank (1m length x 1m width x 1.8m depth) by using a submerged pump connected with a steel pipe of diameter 15 cm with a control valve that controls the discharge flowing to the inlet tank. A by-pass pipe that attached with a control valve that used to discharge the excess flow back to the underground storage tank in case that the submerged pump is operated while the main pipe valve is not allowing the flow to pass through.

Figure (3- 6): Inlet pipes' connection

Figure (3- 5): Inlet tank

Figure (3- 7): Channel's Inlet straightener pipes

The magnetic flowmeter was working based on the magnetic field that is applied to the metering tube, which results in a potential difference proportional to the flow velocity perpendicular to the flux lines. The physical principle at work is electromagnetic induction; the magnetic flow meter has two units to measure and display the discharge (device, and reader) as shown in figures (3-8) and (3-9).

Figure (3- 8): Flow meter reader

Figure (3- 9): Flow meter device

Two control valves, as in figure(3-10), are installed on the inlet and By-pass pipes, the main-stream valve is used to control the discharge from the submerged pump to the inlet tank; while the other Valve is fixed on the by-pass pipe in case there is no desire to supply the inlet tank while in the same time the pump is operated.

Figure (3- 10): Control valve

In the channel's downstream, there is an outflow tank that placed mainly to capture the sediment particles which discharged out from the channel and to recycle the water flow back to the underground storage tank. The tank is divided into two parts by a metal vertical sheet. Firstly, sediment trapping where the sediment particles are trapped in a specially designed cubic basket with wooden structure supporting metal permeable net, which hinders the transport of the particles out from the system to the storage tank; therefore, the particles retained on the net can be taken in order to feed the system again through the hopper. The metal sheet works as a weir to let the water flows freely to the second part of the tank, where the water is recirculated through a plastic pipe Ø 200 to the storage tank where the water is pumped back in to the system through the inlet tank. A control valve Ø40 was inserted on the outlet of the tank to adjust properly the water level downstream the weir as well as emptying the system in case of shutting down.

3.1.2 sediment particles' properties

The sediment used in this work was made of Polybutylene Terephthalate (PBT). Uniform, quasi spherical particles with an aspect ratio of 2 were used. Three samples of sediment have been mixed together to have a sufficient quantity to perform the experiment based on their properties' similarity. The Sediment mix density was ρ_s = 1,317 kg/m3 Porosity= 0.41.

the equivalent diameter was determined using the following formula:

$$\mathbf{d_{eq}=(\,d1\ \times\ d2\ \times\ T\,)^{\frac{1}{3}};}$$

where;
d1= first dimension.
d2= second dimension.
T= particle thickness.

Three samples of sediment were used and mixed together based on their similarity of properties as will be shown later; The first sample was completely white that used previously on the same experiment, the second one was totally black, and the third one was white that was bought recently and available for the usage for the experiment. Figure (3-11) shows the CDF(Cumulative Distribution Function) that calculated for each sample.

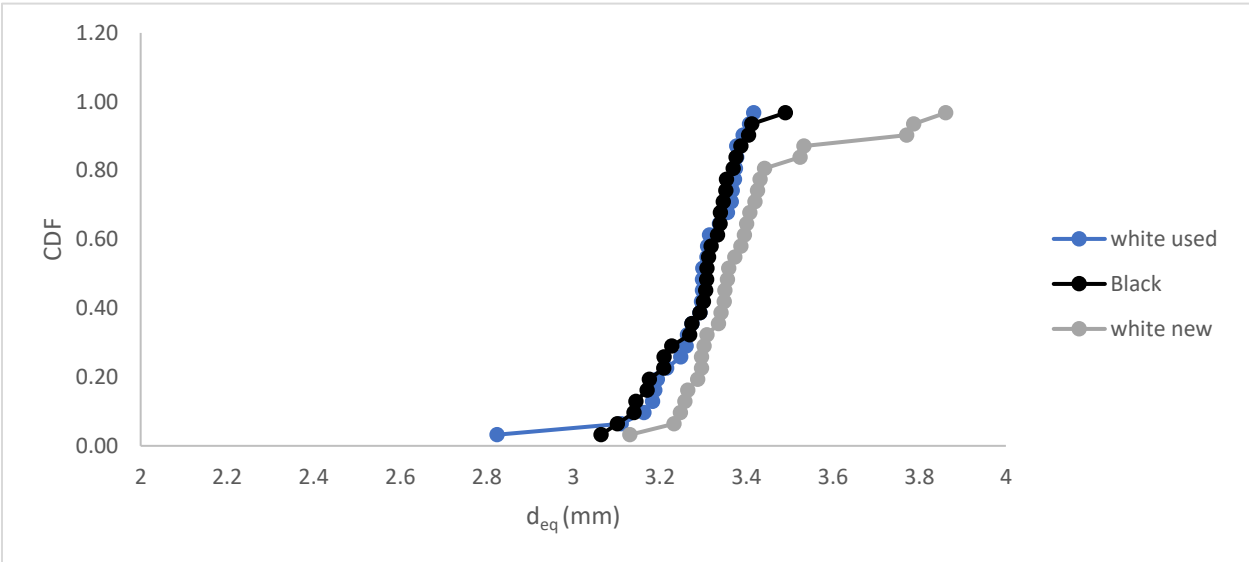

Figure (3- 11): CDF of sediment samples

Table (3-1) shows the equivalent diameter and particle diversity indicator for each sample:

	white used	Black	White New
	Sample#1	Sample#2	Sample#3
d_16	3.18	3.17	3.26
d_50	3.29	3.3	3.357
d_84	3.37	3.37	3.52
σ_g	1.029	1.032	1.039

Table (3- 1): Sediment properties

3.1.3 sediment feeding component.

A system for feeding and trapping the sediment particles was set up. Firstly, the feeding phase is operated by using a hopper with volume 3102.5 cm^3 , as shown in figure (3-12), which has a variable slot dimension allows setting different values for the sediment transport, the slot length is always38cm and height is 1 cm; however, the width is varying incrementally by 1 cm from 1cm to 5 cm based of on the desired sediment

flowrate. The trapping phase is based on attaching a permeable metal net to channel downstream on a wooden frame to collect the amount of sediment that going out from the channel.

Figure (3- 12): Hopper (Sediment feeder)

The Hopper has an electronic controller for operation and setting the time of feeding is depending of the designed sediment flow rate as in figure (3-13).

Figure (3- 13): Hopper controller

The determination of the slot dimension and feeding time increment is based on the designed Qs (live bed load). The relation is $Qs=\frac{Vslot}{\Delta t}$ as V_{slot} is the volume of the slot opening and Δt is the cycle duration; the following table shows the slot width and feeding time corresponding to Qs under equilibrium conditions with respect to the ratio between the flowrate and the critical flowrate when the incipient sediment motion starts. The calculation of the slot width and Δt was done in a previous work, table (3-2), on the same system components and properties for different condition of Q/Q_c.

Q/Qc	Qs (m2/s)	$\Delta t_{sediment\ feeder}$(s)	slot width(cm)
1.2	7.81E-07	79	1
1.4	6.18E-06	20	2
1.6	2.61E-05	12	5

Table (3- 2): Hopper slot width and cycle duration for different Q/Qc(Radice and lauva,2017).

The sediment particles must be introduced into the system moistened to simulate the real condition, there for a small pump has been installed to supply the sediment particles with enough water by a perforated nose and the inlet tank is the intake as illustrated in figure (3-14).

Figure (3- 14): Perforated pipe for wetting sediment

3.2 Measuring devices.

An automatic concept is introduced to measure the water depth, obtain the scour depth, and figure out the bed elevation alteration. Laser beams were used that fixed on the channel cover in the place where finding out the bed elevation is desired; the signal is transmitted to the PC to be presentable by an acquisition tool attached on the way between the lasers and the PC.

3.2.1 measuring tools and accuracy.

Lasers

Figure (3-15) represents four Optical displacement sensors have been placed on the experiment channel in order to measure the water depth, consequently the local scour depth and bed elevation through the channel. The placement of the lasers on the channel is differing based on the desired output; For example, distant placement of the lasers allows obtaining the profile of bed variations and dunes' shape and motion; however close placing in front of the pier allows checking out and understanding the scour hole shape.

Figure (3- 15): Lasers

Figure (3-16) shows the concept of laser's work is based on the incident laser beam and the reflected one received after hitting the channel bed; a certain voltage is obtained based on this incident and received beam; consequently, by using the calibration equation the depth is determined.

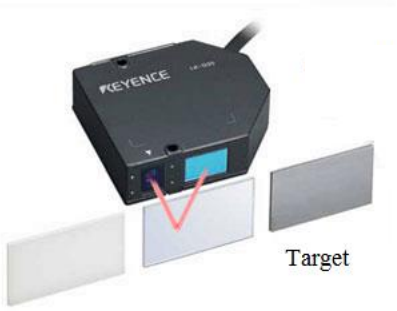

Figure (3- 16): Laser measuring concept.

The lasers' beam is passing through two different media In order to calibrate the laser to measure the water depth through two different medias that are Plexiglas which is represented in the laser's holder and the channel cover, and the water represented inside the channel till the bed as a target of the measurement , a gauge and simulated target inside a water bucket were used to determine the linear relation between the measured depth and volts obtained by the laser according to the following linear equation (Y=aX + b) where Y is depth in mm while X is the voltage measured by the laser , in order to determine the constants (a,b), 13 points have been measured using the gauge and laser then a plot has been developed between measured distance after excluding the reference depth(where the laser starts to read) and the measured volts by the laser to find out the relation between both arrays; consequently, constants (a,b) for each laser are obtained as shown in tables (3-3) and (3-4), and figure (3-17):

calibration of laser 1 in still water				
reference gauge reading at plate touch 27.28				
gauge	tester	voltage	dist(cm)	distance(mm)
19.61	0.200	0.18	7.67	76.7
18	0.5	0.51	9.28	92.8
16.5	0.78	0.76	10.78	107.8
15	1.09	1.09	12.28	122.8
13.5	1.39	1.39	13.78	137.8
12	1.66	1.66	15.28	152.8
10.5	1.93	1.95	16.78	167.8
9	2.21	2.23	18.28	182.8
7.5	2.48	2.48	19.78	197.8
6	2.77	2.77	21.28	212.8
4.5	3.07	3.07	22.78	227.8
3	3.39	3.41	24.28	242.8
2	3.66	3.58	25.28	252.8

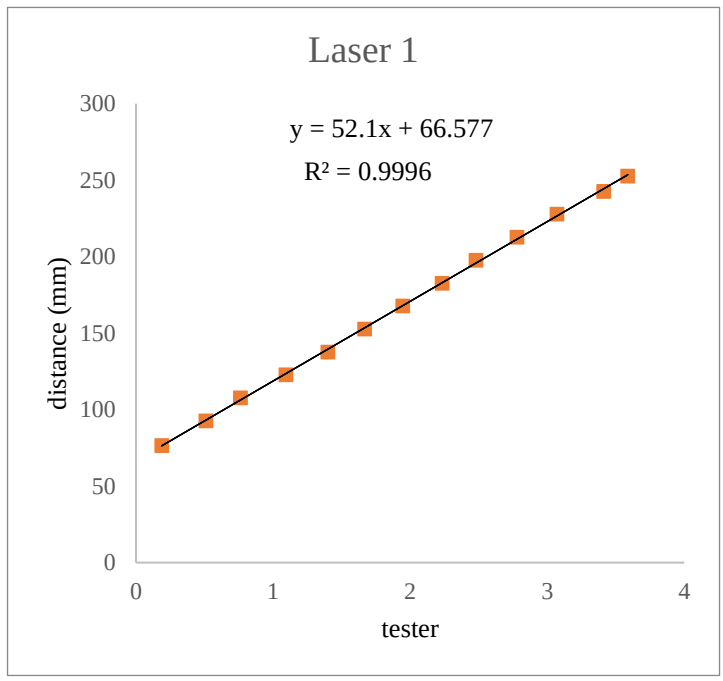

calibration of laser 2 in still water				
reference gauge reading at plate touch 27.28				
gauge	tester	voltage	dist(cm)	Distance(mm)
19.5	0.220	0.21	7.78	77.8
18	0.44	0.443	9.28	92.8
16.5	0.67	0.675	10.78	107.8
15	0.91	0.904	12.28	122.8
13.5	1.13	1.139	13.78	137.8
12	1.35	1.349	15.28	152.8
10.5	1.58	1.58	16.78	167.8
9	1.81	1.82	18.28	182.8
7.5	2.05	2.051	19.78	197.8
6	2.27	2.2863	21.28	212.8
4.5	2.5	2.517	22.78	227.8
3	2.74	2.779	24.28	242.8
2	2.92	2.95	25.28	252.8

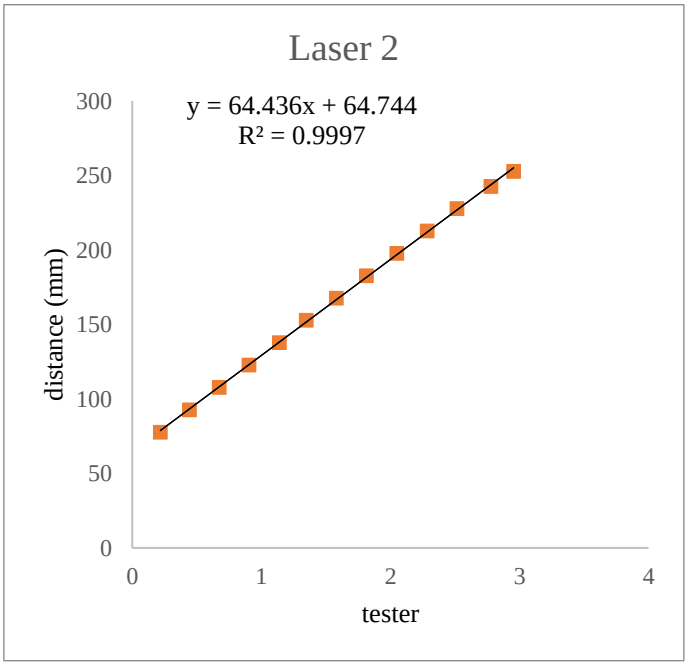

calibration of laser 3 in still water				
reference gauge reading at plate touch 27.28				
gauge	tester	voltage	dist(cm)	Distance(mm)
19.5	0.160	0.161	7.78	77.8
18	0.39	0.399	9.28	92.8
16.5	0.62	0.628	10.78	107.8
15	0.85	0.856	12.28	122.8
13.5	1.08	1.089	13.78	137.8
12	1.3	1.312	15.28	152.8
10.5	1.52	1.529	16.78	167.8
9	1.74	1.752	18.28	182.8
7.5	1.97	1.982	19.78	197.8
6	2.2	2.209	21.28	212.8
4.5	2.42	2.423	22.78	227.8
3	2.65	2.664	24.28	242.8
2	2.8	2.818	25.28	252.8

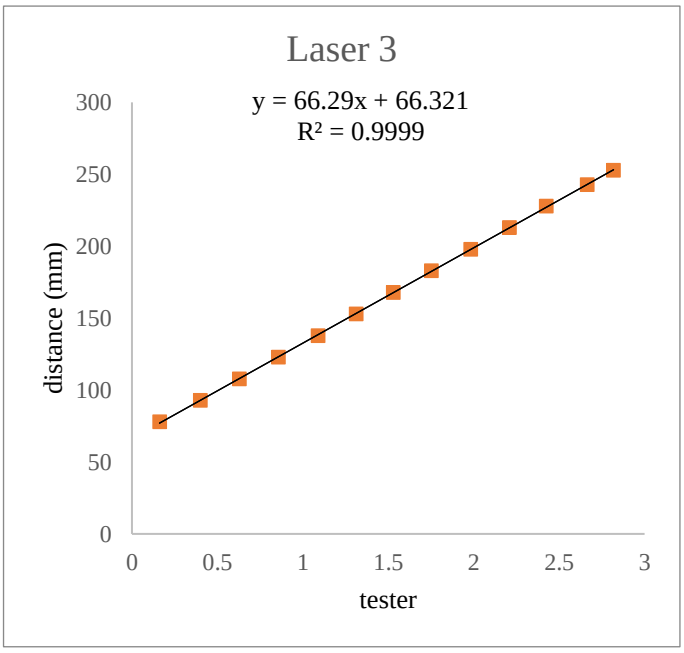

calibration of laser 4 in still water				
reference gauge reading at plate touch 27.28				
gauge	tester	voltage	dist(cm)	distance(mm)
19.5	0.170	0.171	7.78	77.8
18	0.4	0.403	9.28	92.8
16.5	0.62	0.628	10.78	107.8
15	0.85	0.863	12.28	122.8
13.5	1.08	1.092	13.78	137.8
12	1.32	1.322	15.28	152.8
10.5	1.54	1.549	16.78	167.8
9	1.77	1.783	18.28	182.8
7.5	2	2.009	19.78	197.8
6	2.23	2.239	21.28	212.8
4.5	2.46	2.476	22.78	227.8
3	2.69	2.702	24.28	242.8
2	2.84	2.856	25.28	252.8

Table (3- 3): Lasers' calibration computations.

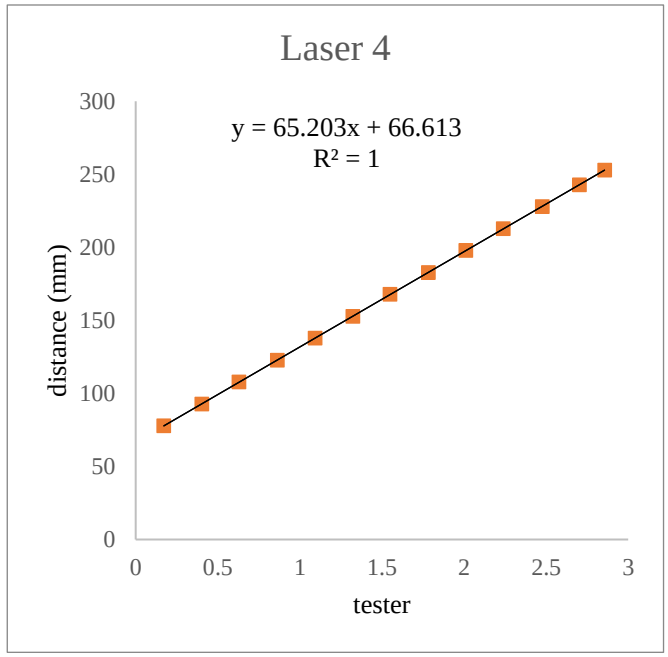

Figure (3- 17): Lasers' calibration curve.

Laser	Parameters	
	a	b
1	52.1	66.57
2	64.43	64.74
3	66.29	66.32
4	65.2	66.61

Table (3- 4): Lasers' calibration parameters

The previous figures and tables show the difference of calibration parameters are slightly various between the 2nd, 3th, and 4th laser; while the first laser is distinct specially in parameter (a) because the first laser is from a different manufacture than the other three lasers; as the parameter (b) isn't so versatile between all the lasers.

Voltmeter

The Voltmeter, figure (3-18), is used to measure and check the voltage on the power supply as well as on the acquisition tool that connects the lasers to the PC.

Figure (3- 18): Voltmeter

acquisition tool and power supply

An acquisition tool of national instrument is used for acquiring the measured values by lasers and sending them to the attached PC; as the power supply is installed to provide the lasers with the required voltage as shown in figure (3-19).

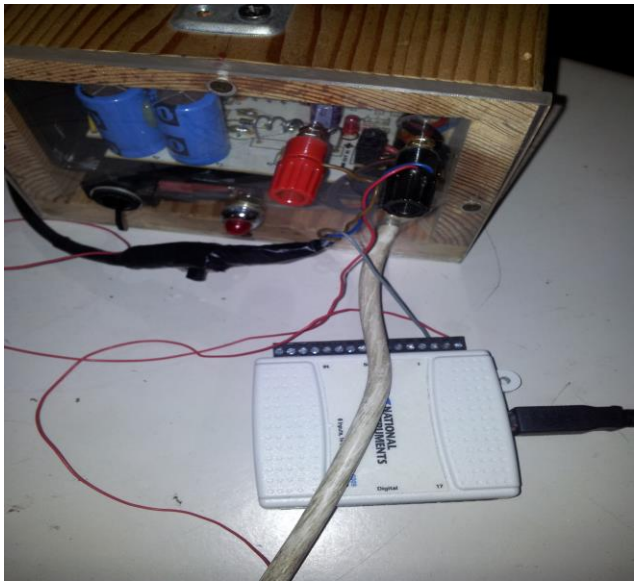

Figure (3- 19): Acquisition tool and power supply

3.2.2 Software process.

The main softwares are used in the operation are Visual Basic 2013 and Labview 2017 for acquisition of the acquired data by the placed lasers and transmitting them to a data file in .csv format to be easily dealt with.

3.3. Experimental Campaign.

Setting up of different experiments based on the purpose of the results and to figure out the phenomena of live bed Pier scour were carried out initially as well as defining the threshold conditions for bed load incipient motion.

3.3.1 experimental set up.

A 2m recess section is present in the last portion of the flume. A telescopic pier was used for the scour runs. The pier was placed in the channel axis at 450 cm from the inlet. The outer part of the pier was a PVC pipe with internal and external diameters of 0.06 m and 0.064 m, respectively. The inner part was a Plexiglas cylindrical bar that could slide within the outer one. The inner part of the pier could be lifted using a fisherman wire that was attached to its top and passed through a pipe attached to the channel lid; it could be instead lowered by pushing it with a stick (Radice and Lauva,2017).

Many experiments were done under different conditions of steady state and unsteady state to by varying versatile constraints to figure out various facets of the live-bed pier scour phenomenon. The placement of the sensors over the flume lid is not constant but changes based on the purpose of each experiment, two main positions were introduced in our experimental process; close placement of the sensor to the pier and between each other's to figure out the behavior and characteristics of the scour hole, and distant placement of the sensor was performed for investigating more characteristics of bed further than just scour depth such as dunes' motion and behavior. Figure (3-20) shows the systemic operation of an experiment showing all the components that involved during the experimental work.

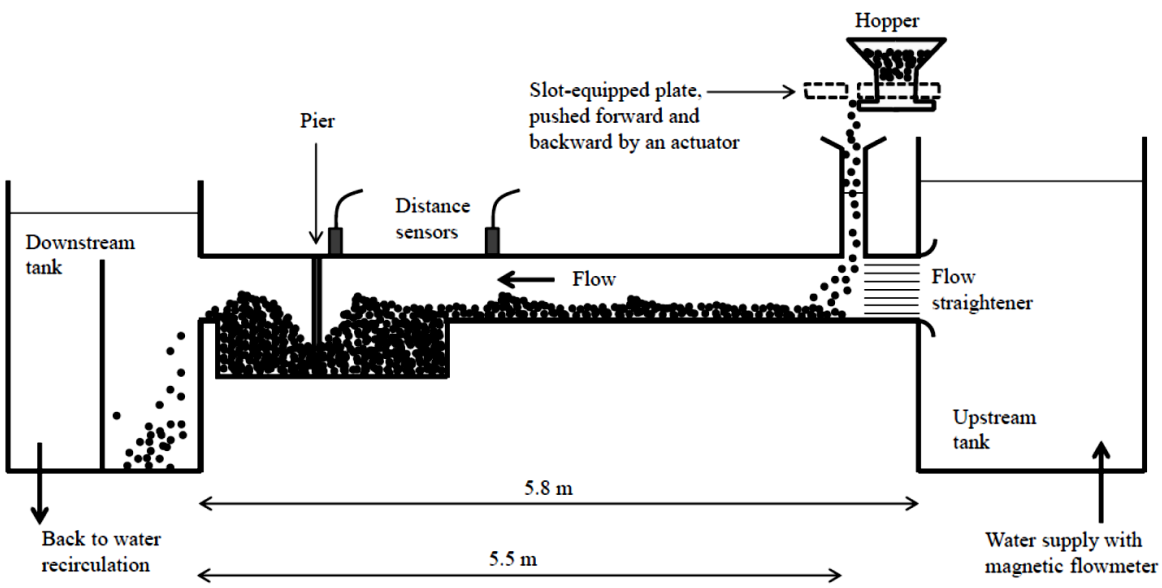

Figure (3- 20): Experimental set up sketch (Radice and Lauva,2017).

The experiments have been operated in a sequential process to operate the experimental components and acquire the measured data. Live-bed experiments could be run as single ones, by:

(i) activating the channel,
(ii) letting dunes develop until a stationary state with the pier buried in the bed,
(iii) lifting the pier and starting the scour until and after equilibrium was reached.

Experiments could be also performed in a sequence if, after a first one;

(iv) the pier was lowered,
(iv) discharge and feeding rate were changed until a new equilibrium configuration of dunes,
(v) the pier was lifted again.

3.3.2 Threshold conditions.

The estimation of threshold conditions for sediment motion is, as well known, affected by large uncertainties (see, among many others, Buffington and Montgomery, 1997). A definition of incipient particle motion based on a 'small' sediment transport rate (e.g., Schvidchenko and Pender,2000) has been proposed for the determination of the threshold conditions. In this study, a threshold discharge for particle motion was determined following a definition proposed by Radice and Ballio (2008), according to which the incipient motion corresponds to a dimensionless sediment transport rate per unit width Ø = 6 × 10-5 [Ø = Q_s /(gΔ_d^{3})$^{0.5}$, with Q_s as the solid discharge per unit width, g

as the acceleration due to gravity and $\Delta = (\rho_s - \rho)/\rho$ where ρ is the water density. A 3-cm thick sediment layer was placed into the channel along its entire length to create a movable bed. The critical discharge was determined during preliminary experiments as Q_c = 13.2 l/s (Radice and Lauva,2017).

Figure (3-21) shows the tests that have been done in a previous experimental work on the same sediment sample and flume, to determine the incipient motion due to a critical flow rate.

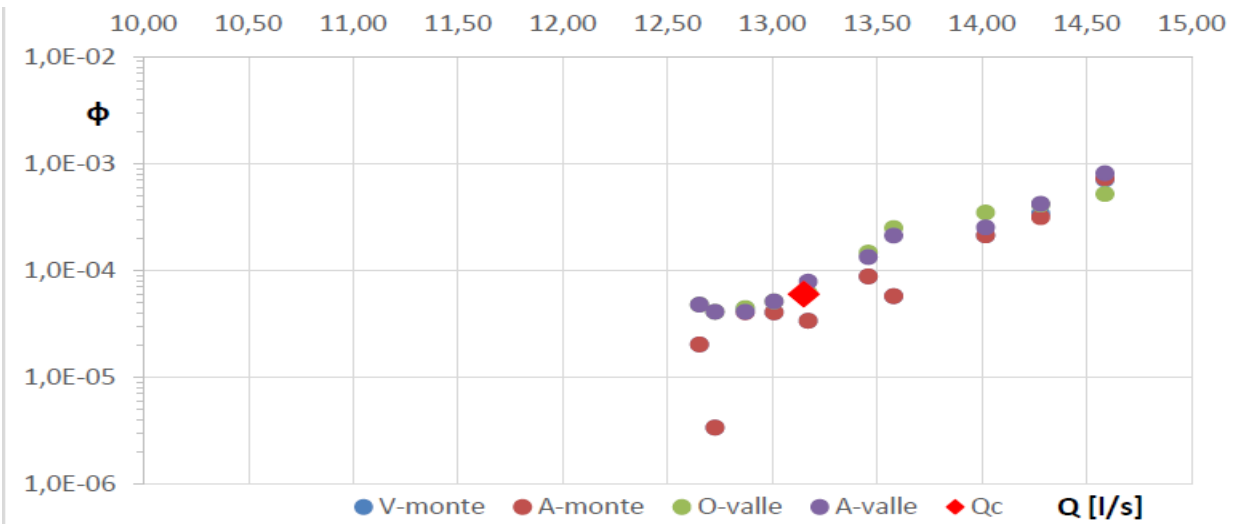

Figure (3- 21): Critical flow for incipient motion (Veronica, 2015).

4. Steady experiments and analysis.

4.1 Steady experimental runs.

In contrast to clear-water scouring conditions, live-bed scour occurs when there is general bed-load transport, at which point the incoming rate of sediment transport into the scouring zone ≠ 0. In other words, the undisturbed approach mean velocity exceeds the critical velocity for bed sediment entrainment, i.e., $V > V_c$. The definition of the live-bed scour condition simply describes a nonzero rate of sediment transport from the upstream, Qs_{in}, into the scour hole (hong et al,2016).

The imposed flow rates to the present live-bed experiments are corresponding to Q/Q_c ratios of 1.4 and 1.6. Higher transport rates were prevented by the feeding technology and sediment availability while lower flow rate has difficulty in evolving bed formation based on previous experiments done under the same conditions. The feeding rates that were employed in these tests were determined by trial and error in order to maintain a stationary bed elevation at the measuring locations upstream of the pier (Radice and lauva,2017). Water heights H correspond to the average distance measured from the lid to the bed during the stationary stages. The bulk flow velocity V was also computed with reference to this average distance. furthermore, the bed forms were characterized by a steep front and mild tail and migrated downstream, thus meeting the general description of fluvial dunes (Radice and lauva,2017).

When the inner part of the pier was in the lower position, the obstacle was however exposed to the flow during the passage of dune troughs, with some local scour appearing. In order to maintain a uniform initial condition for the scour experiments, the pier was lifted when the bed level was approximately at the top level of the lower part, thus starting from a zero-scour depth. Additionally, some experiments are done by replacing the lasers in different spots for further investigation such as E2 is lasers' rearrangement of E1, and E4 and E5 are repositioning of E3 with different angles to the flow direction.

This work is a follow up to what has been started by Radice and lauva (2017) for further investigation and analysis of the live-bed conditions. Table (4-1) shows the performed experiments and their water flow characteristics as well as sediment feeding. The sediment feeding characteristics was taken from Radice and lauva (2017) work, that determined based on the method of Ballio and Radice(2008).

The performed experiments differentiate based on two boundary conditions: first, the positioning of the measuring points, at which many spots of the channel were detected to have a wide understanding of the interrelation between the different features that induced by the application of live-bed conditions; second, two different flow rates were

assigned to this experimental campaign under steady condition to widen the literature background about steady live-bed analysis and more understanding of the process in addition to found for the unsteady live-bed investigation.

Table (4-2) is the plan for the present study campaign, in which stated the description of each experiment with the prescribed sketch that allows a better envisage of the measuring points positions with respect to the pier.

Experiment	Q (l/s)	Q/Qc	H (mm)	V (m/s)	Fr	Qs (m2/s)	T_s (s)	$\Delta s_{sediment\ feeder}$(s)	slot width(cm)
E1	18.38	1.39	138.4	0.332	0.28	6.18E-06	7740	20	2
E2	18.36	1.39	138.4	0.332	0.28	6.18E-06	5420	20	2
E3	18.43	1.40	142.4	0.324	0.27	6.18E-06	5510	20	2
E4	18.43	1.40	142.4	0.324	0.27	6.18E-06	4550	20	2
E5	18.43	1.40	142.4	0.324	0.27	6.18E-06	5570	20	2
E6	21.12	1.60	129.7	0.407	0.36	2.61E-05	7285	12	5
E7	21.12	1.60	129.7	0.407	0.36	2.61E-05	4395	12	5

Table (4- 1): Steady Experiments.

test	positioning Sketch	Description
E1		Distant placement of measuring points on the central axis of the channel was performed to check the behavior and the characteristics of the bedforms as well as the development of the scour hole.
E2	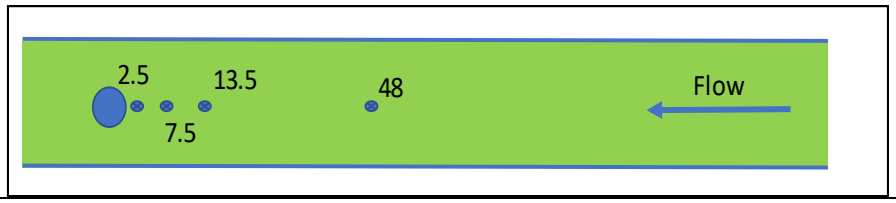	close placement of three measuring points inside and on the edge of the scour hole to visualize and analyze the temporal fluctuation of the scour hole as well as the fourth point used to continue measuring the fluctuation of normal bed elevation and evolution of bedforms on the central axis of the channel
E3	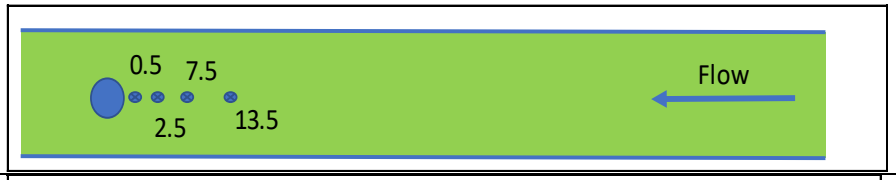	the measuring points were placed inside and on the edge of the scour hole to investigate the evolution of the scour hole and to understand the temporal behavior on the central axis of the channel
E4	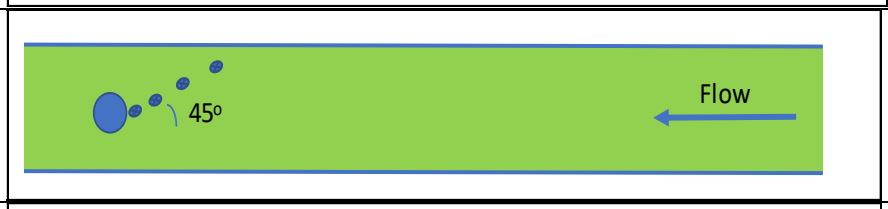	the measuring points were inclined to the central axis by 45º anti- clockwise with the same distances between them to check the characteristics of the scour hole and the fall of bedforms inside within this direction
E5	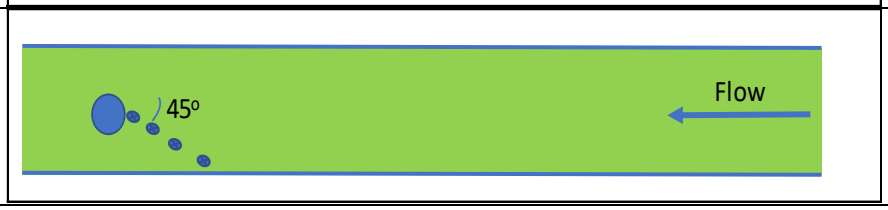	the measuring points were inclined to the central axis by 45º clockwise with the same distances between them to check the characteristics of the scour hole and the fall of bedforms inside within this direction
E6	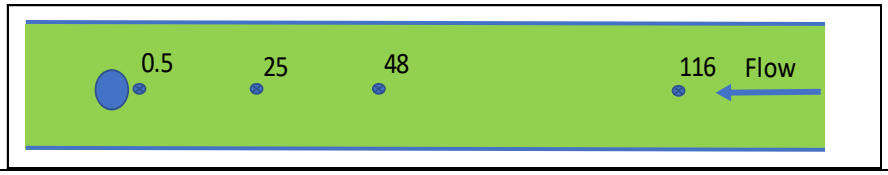	Distant placement of measuring points on the central axis of the channel was performed to check the behavior and the characteristics of the bedforms as well as the development of the scour hole in higher flow rate and sediment feeding.
E7	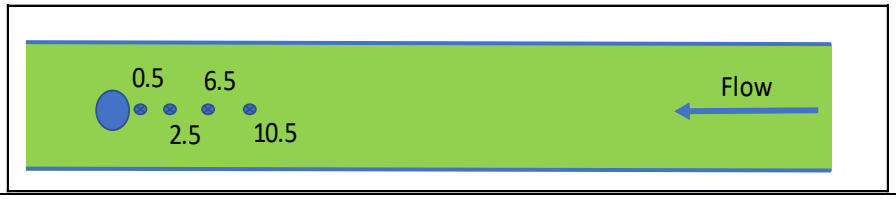	the measuring points were placed inside and on the edge of the scour hole to investigate the evolution of the scour hole and to understand the temporal behavior on the central axis of the channel with higher flow rate.
Legend	Pier Measuring point **Note:** the written distances are measured in centimeters from the pier nose.	

Table (4- 2): Experiments description and measuring points placement.

To have a general envisage of what can be expected form a measuring point , figure (4-1) shows the temporal fluctuation of the depth measured by the placed laser at 13.5 cm upstream of the pier that was on the edge of the scour hole during experiment E3, at which the bed features(dunes) are clearly represented.

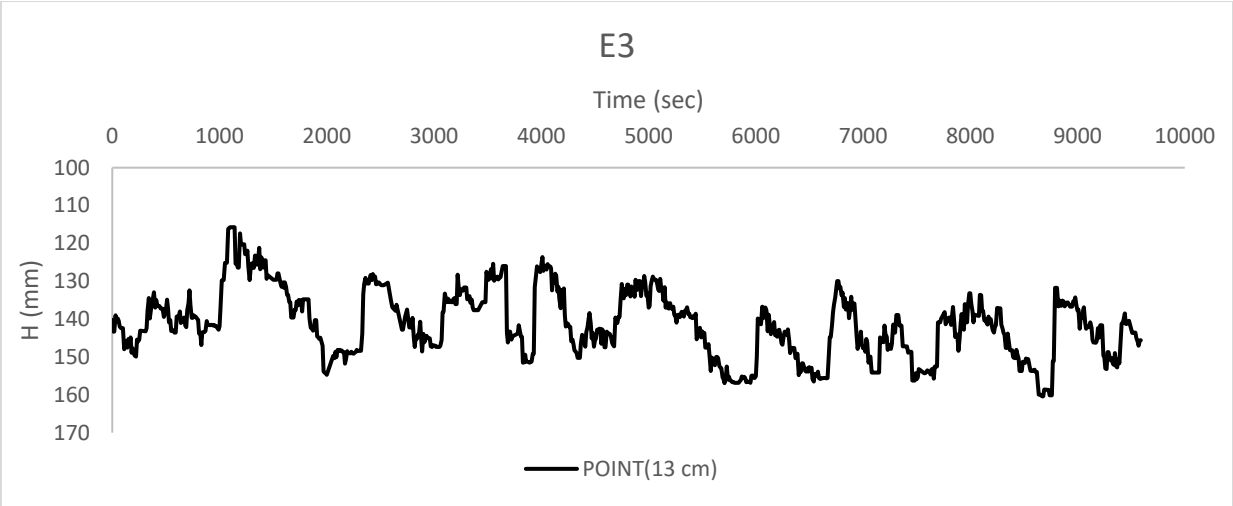

Figure (4- 1): Bed fluctuation sample in E3

On the other hand, Figure (4-2) depicts the depth obtained by the placed laser at 2.5 cm upstream of the pier nose during experiment E3, there are five stages describe the variation of the scour through the time: (1) hole refilling after changing the flow and feeding rate, (2) bed adjustment, (3) stationary bed fluctuations before starting the scour, (4) pier extraction and the scour development,(5) scour fluctuation after equilibrium.

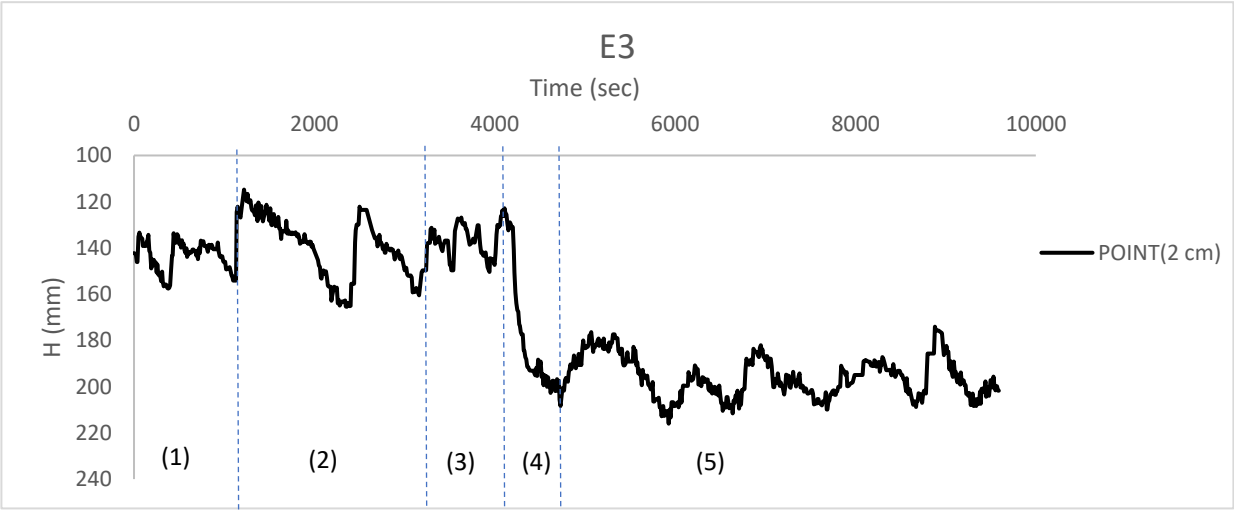

Figure (4- 2): Scour evolution phases.

4.1.1 data despiking.

The used lasers for measuring the water depth were calibrated to work in the present media which is made of glass with 1.5 cm thickness covering the water. Due to the air bubbles formed under the channel lid and the relative weakness of the incident laser signals which interrupted by these bubbles, false and anomalous values are recorded sometimes within the acquired data as shown in figure (4-3) that shows the raw data at the measuring point placed 25 cm upstream of the pier nose for experiment E1. Therefore, data despiking is applied to all the obtained measuring points.

Despiking involves two steps:
(1) detecting the spike.
(2) replacing the spike.

The two steps are independent, so they are considered separately here. Indeed, in most cases, the methods for spike detection can be mixed interchangeably with any of the methods for spike replacement. However, for the iterative methods, spike replacement can affect spike detection in the subsequent iterations (Goring and Nikora,2002).

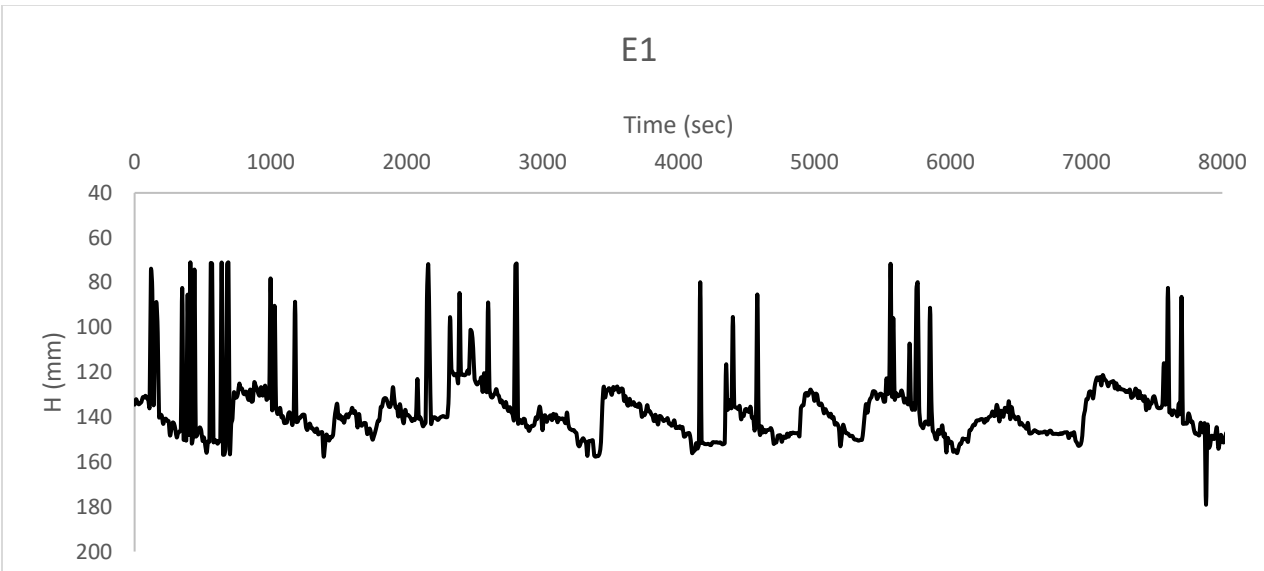

Figure (4- 3): Raw data sample.

Tukey 53H method of eliminating anomalous values was used which uses the principle that the median robust estimator of the mean to generate a smooth time sequence that can be subtracted from the original signal.

The steps were used as following (Goring and Nikora,2002).:

1. Construct a sequence ui(1) from the median of the five data points from ui-2 to ui+2 ;
2. Construct a sequence ui(2) from the median of the three data points from ui-1(1) to ui+1(1) ;
3. Construct the Hanning smoothing filter ui(3)= $\frac{1}{4}$(ui-1(2) + 2ui(2) + ui+1(2));

4. Construct the sequence $\Delta I = |ui - ui(3)|$ and reject the point if $\Delta I > N\,\sigma_d$, where N is a predetermined threshold and σ_d is the standard deviation of ui ;
5. Replace the spike with the preceding record.

However, when applying the mentioned method in case of consecutive anomalous records, a value can be evidently constant on a certain time span. Therefore, further manual intervention by linearly interpolating values over this time span based on a set of preceding and following records must be done to keep the consistency of the data.

The despiked data is shown in figure (4-4).

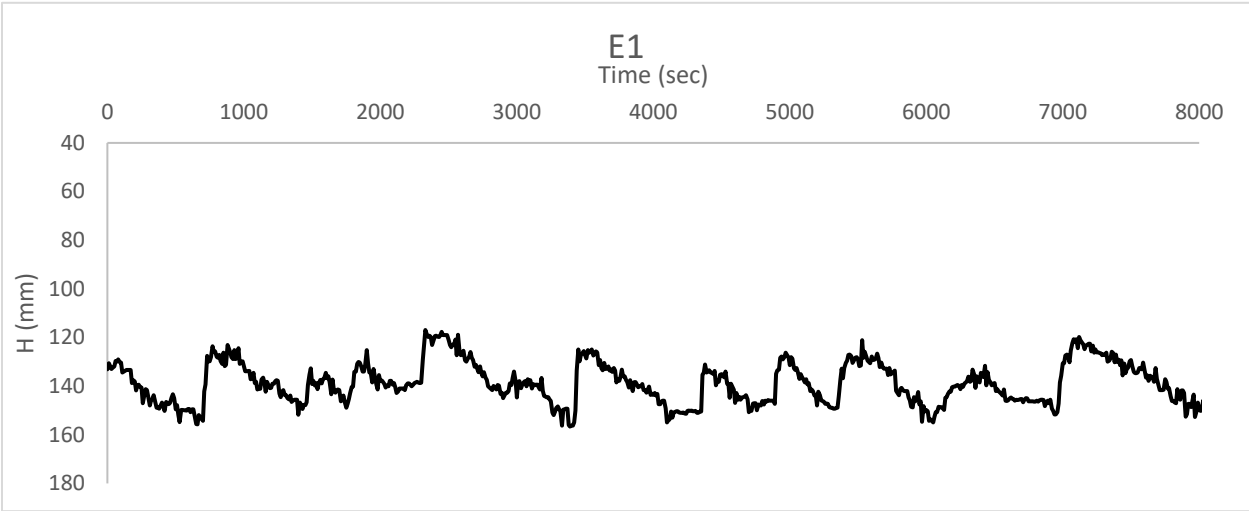

Figure (4- 4): Despiked data

Sometimes the despiking process does not work properly to eliminate all the anomalous data; therefore, further manual refinement by linear interpolating the part of anomalous data by the way mentioned beforehand. Figure (4-5) shows the measuring point placed at the pier face for experiment E1 after applying the despiking method.

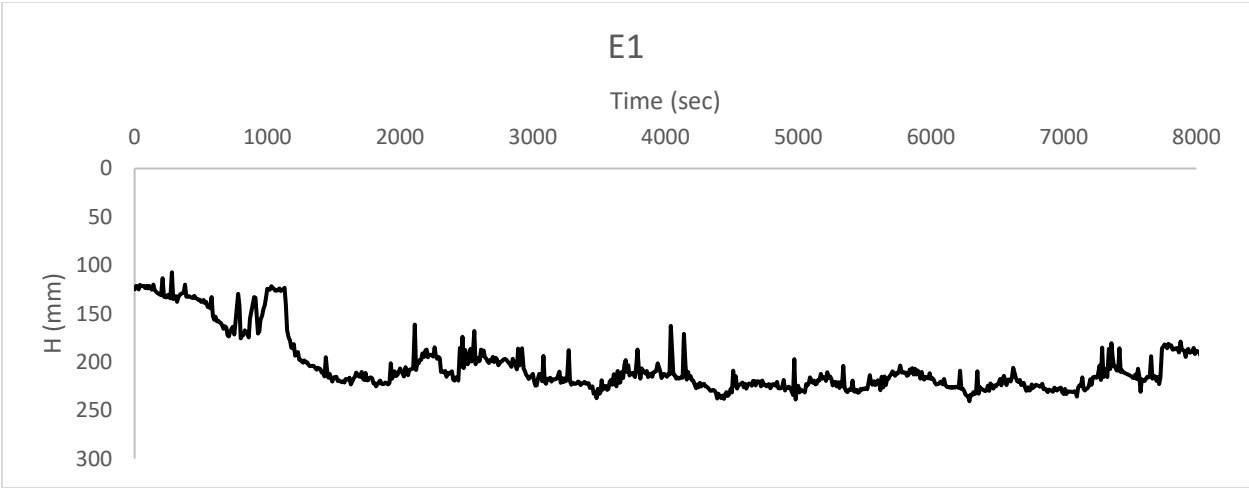

Figure (4- 5): Unrefined despiked data

As shown in the figure, some spikes were not eliminated by just despiking process. By applying the manual refinement, the data series became more consistent as shown in figure (4-6).

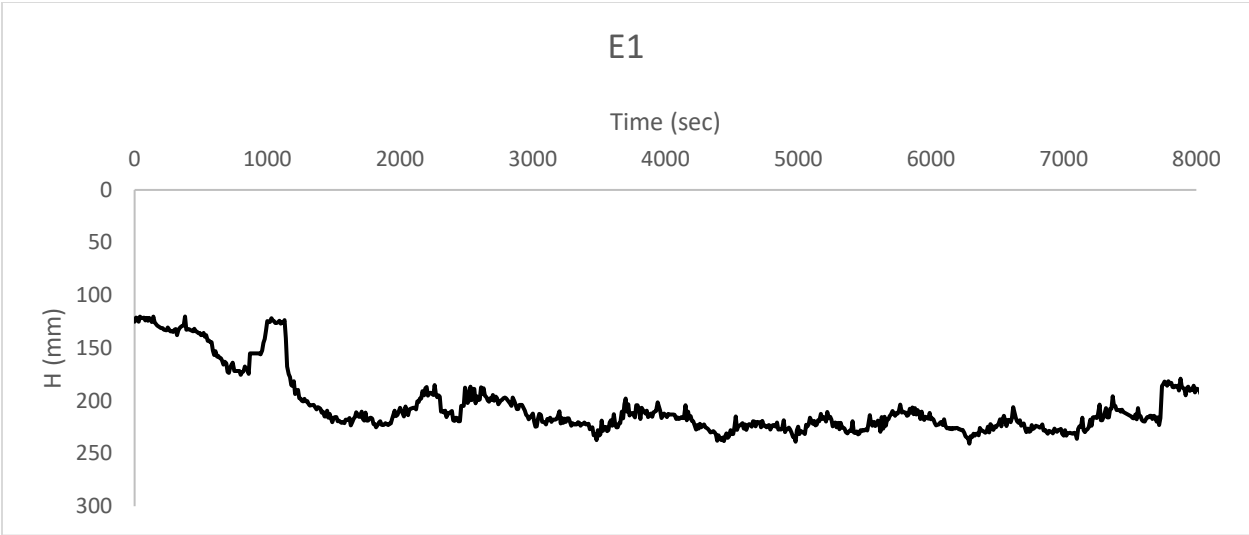

Figure (4- 6): Refined and despiked data

4.2 Scour experiments analysis.

The investigation of scour characteristics was done by different positioning of the measuring points to acquire the corresponding water depth, thereby, many analyses were performed based on the acquired data to understand the phenomena of circular pier scour.

4.2.1 Scour equilibrium time and depth.

Equilibrium time

In the equilibrium state of scour, for a given size of sediment, the flow around the pier is unable to move any more sediment away from the scour hole (chang et al,2004).

The temporal evolution of the scour depth starts at the time of lifting the pier, a progressive increase of the scour depth upstream of the pier is evident until reaching the equilibrium condition stated previously after an equilibrium time t_e. In live-bed scour, the equilibrium time depends on the flow rate, as it is an inverse relationship of flow rate. The equilibrium time is estimated in two steps: first, computing the mean scour depth at the end phase of temporal scour oscillation; second, computing the time required to reach this calculated value starting from the development phase. Figure (4-7) shows a representation of scour evolution at the pier for two experiments that were performed under two different conditions of water discharge ($1.4Q_c$ and $1.6Q_c$) for experiments E1 and E6, respectively.

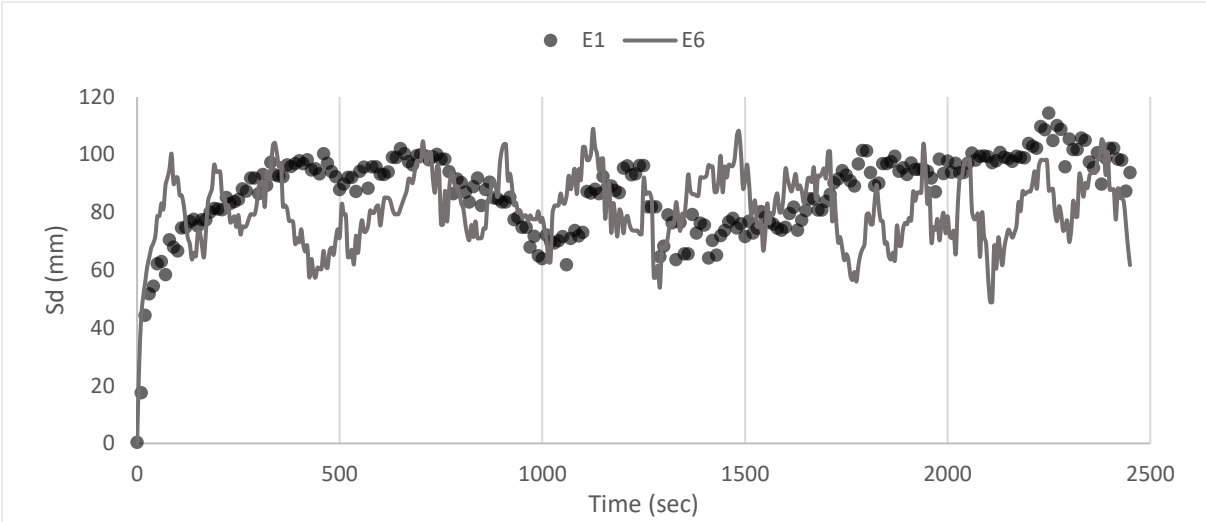

Figure (4- 7): Scour depth evolution at different discharge.

At higher flow rate, less time needed to reach the equilibrium phase. Obviously, a milder scour evolution is present at lower flowrate as a consequence of sediment transport rate that increases by higher flow rate. Therefore, the ripely evolved dunes cause more fluctuating progression phase in case of E6 that associated with higher flow rate.

Moreover, the progression phase was observed only for experiments E1, E3, E6 and E7; therefore, the dimensionless equilibrium time was calculated for both discharges (1.4 Q_c and 1.6 Q_c) based on four mentioned experiments. The value of dimensionless equilibrium time (te*v/b) is computed, as t_e is the equilibrium time measured from the experimental output while V is the mean water velocity inside the channel, and b is the diameter of the pier. Table (4-3) and figure (4-8) show the results of the calculated dimensionless equilibrium time. Evidently, higher values were observed in E1 and E3 with marginal difference, than E6 and E7 that are identical.

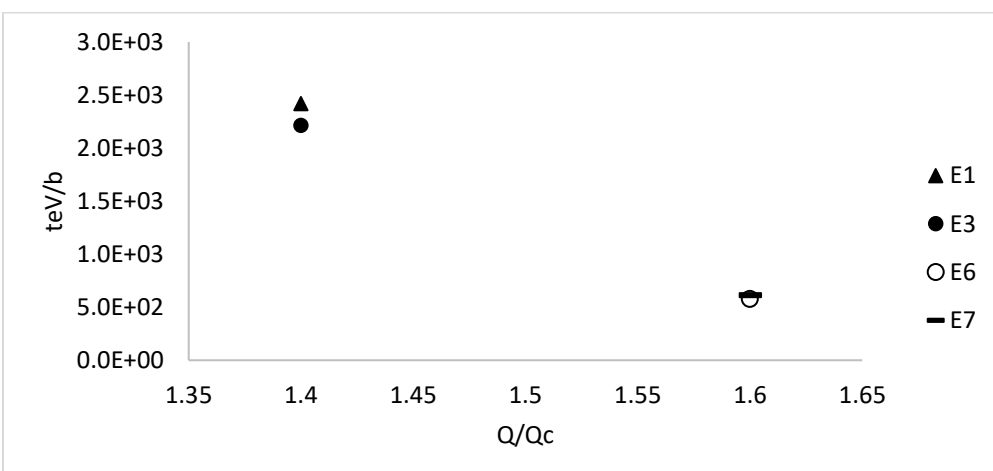

Figure (4- 8): Dimensionless equilibrium time at different discharge.

Experiment	Q/Qc	t_e(sec)	V	b	T_e*V/b
E1	1.4	440	0.33	0.06	2420
E3	1.4	410	0.32	0.06	2214
E6	1.6	85	0.41	0.06	576.58
E7	1.6	90	0.41	0.06	610.5

Table (4- 3): Dimensionless equilibrium time for different experiments

Scour Depth

The measuring point at 0.5 cm from the pier nose was used to measure the temporal evolution of the scour depth as it is the deepest point in the hole. Figures (4-9) and (4-10) depict the temporal oscillation and the development of the scour depth at this point. The first figure shows the scour depth at Q/Q_c=1.4 for experiment E1, while the second one is under condition of higher flow rate (Q/Q_c=1.6) for experiment E6. Obviously, the difference between the pattern observed in both experiments that is based on the water discharge is interpreted by the explanation introduced by chiew and Milvelli (1987), that the minimum equilibrium scour depth (live-bed) occurs at the velocity which produces the steepest dunes translating past the scour hole. With a large dune height and short wavelength, the downflow and horseshoe vortex have relatively little time to remove sediment from the scour hole before the next dune arrives to replenish it. With increasing velocity, the bed features progressively flatten with increasing wavelength and decreasing height reducing the frequency of replenishment of the scour hole by on-coming bed features.

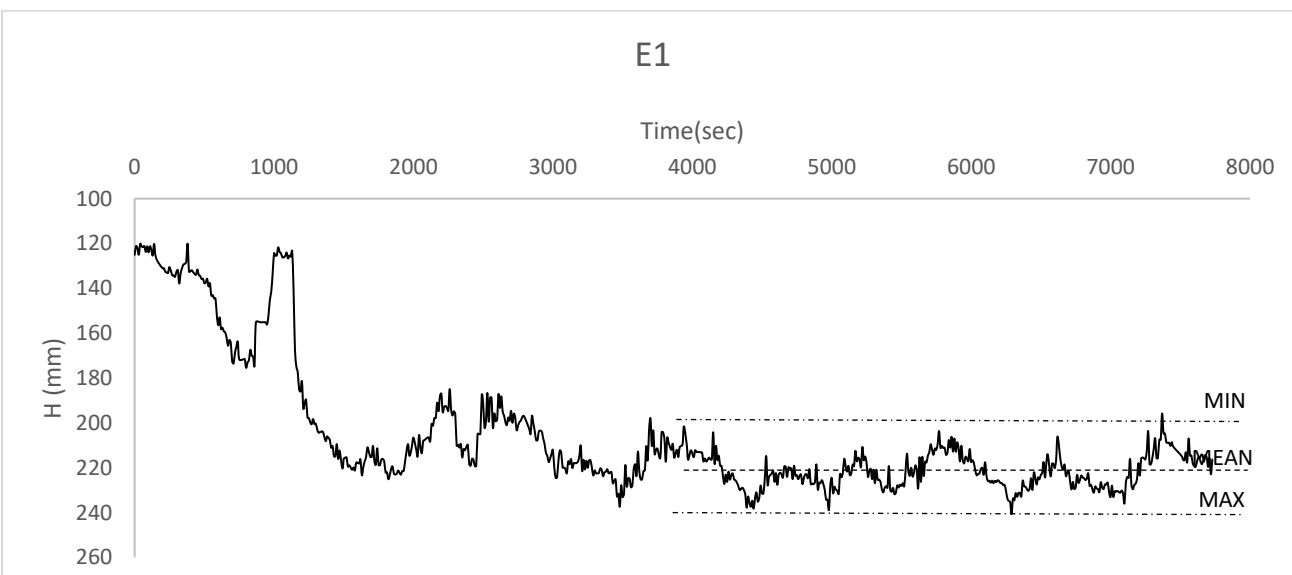

Figure (4- 9): Scour depth fluctuation for Q=1.4Qc

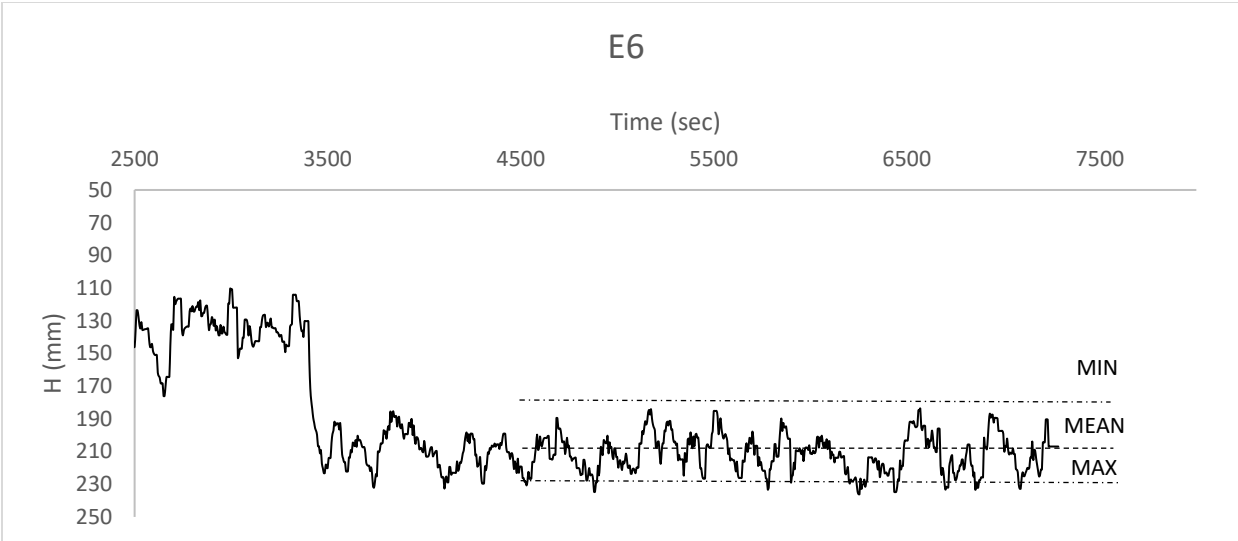

Figure (4- 10): Scour depth fluctuation for Q=1.6Qc

It has been a long debate on which scour depth should be consider for further engineering purposes like structure design or vulnerability assessment. It is claimed by Chiew and Melville that the data should be considered based on the mean depth. However, others instead stated that the maximum scour depth should be consider as the most critical for the safety purpose. Here, the equilibrium scour depth was evaluated based on its minimum, mean and maximum values to quantitively determine the difference between the different values associated with the scour depth. Table (4-4) illustrates the mean, maximum and minimum scour depth of the two-different flow rate of Q/Q_c=1.4 and Q/Q_c=1.6 in mm for experiments E1, E3, E6 and E7.

	E1(1.4Qc)	E3(1.4Qc)	E6(1.6Qc)	E7(1.6Qc)
mean(mm)	86.23	84.36	80.65	78.67
max(mm)	103.56	106.48	113.60	109.61
min (mm)	66.54	61.33	45.74	47.29

Table (4- 4): Scour depth values for different experiments

While table (4-5) shows the dimensionless scour depth with respect to pier's Diameter which is 60 mm.

	E1(1.4Qc)	E3(1.4Qc)	E6(1.6Qc)	E7(1.6Qc)
mean(Sd/b)	1.48	1.40	1.36	1.34
max(Sd/b)	1.65	1.58	1.77	1.73
min(Sd/b)	1.15	1.02	0.90	0.91

Table (4- 5): Dimensionless scour depth for different experiments

Figure (4-11) shows the value of the dimensionless scour depth computed for E1, E3, E6 and E7. the charts represent a comparison between the mean, minimum and maximum values of scour depth based on both discharge values.

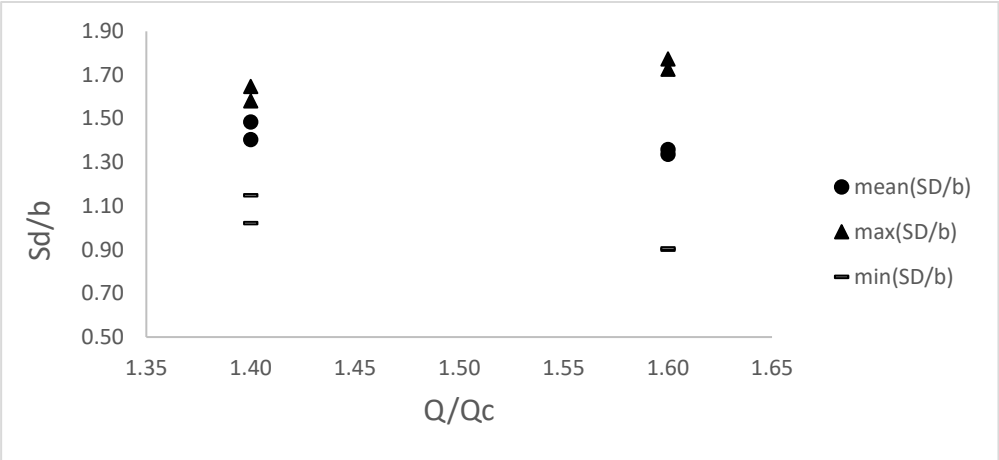

Figure (4- 11): Dimensionless mean, maximum and minimum scour depth change with discharge ratio.

The previous figures conclude that the mean and minimum values of the dimensionless equilibrium scour depth at less discharge value ($1.4Q_c$) is higher than the depth at higher discharge value ($1.6Q_c$). However, the maximum value of scour depth is an increasing function of the discharge value which means higher fluctuation is present at higher discharge. This change was interpreted by Hong et al (2016) that the scour depth attains its deepest value when the dune trough reaches the pier, followed by depth reduction when the crest arrives, consequently, due to the bigger dunes that evolved in higher discharge, the control exerted on the scour depth is considerably high. When the dunes' crest arrives at the scour zone, a sudden decrease occurs in the scour depth; thereby, the force induced by horseshoe vortex reacts to drag more sediment from the active zone around the pier that results in a progressive increase in the scour depth to reach its highest value before the arrival of the consecutive dune.

4.2.2 Scour depth and bed fluctuation.

the scour depth and its variations for velocities greater than threshold are related to the rate of sediment transported into and out of the scour hole. Since a dynamic equilibrium exists between the scouring process and the influx of sediment, the time available for scouring is controlled by the successive bed forms arriving at the scour hole, which in turn, is related to the wavelength of the bed features (chiew and Melville,1987). The water depth was measured at different spots to investigate the spatial bed fluctuation, dunes shape and scour hole evolution through the time as well as the interrelation between the depth variation at different spots. The measuring points were placed at different distances upstream of the pier and inclined to the flow direction in experiments E4 and E5. The amplitude of the scour depth and dunes fluctuation (Δ_{ds} and Δ_d, respectively) were computed form the cumulative frequency distribution (CFD) of measured elevations using different probability ranges (80%, 90%, 95% and 98%). The analysis presents various trends of each probability either for different locations of

measuring points at the same flowrate, or for different flowrates (Q/Q_c=1.4, 1.6) at the same spot.

The time increment which used for estimating the amplitude of a measuring point was selected on the time span after the equilibrium state was achieved. However, the data were not taken immediately after the equilibrium time, but after larger time to guarantee the elimination of any possible interference with the progression phase. For experiment E1 the time interval from 3800s to 7000 was determined to perform the amplitude computations. Figure (4-12) depicts the bed fluctuations at different distances upstream of the pier. Points 2, 3 and 4 show the migrating dunes at distances (25, 48 and 116, respectively) from the pier, while point 1, the stagnation point, shows the evolution of scour depth at 0.5 cm from the pier in addition to the scour depth fluctuation on the whole period. .

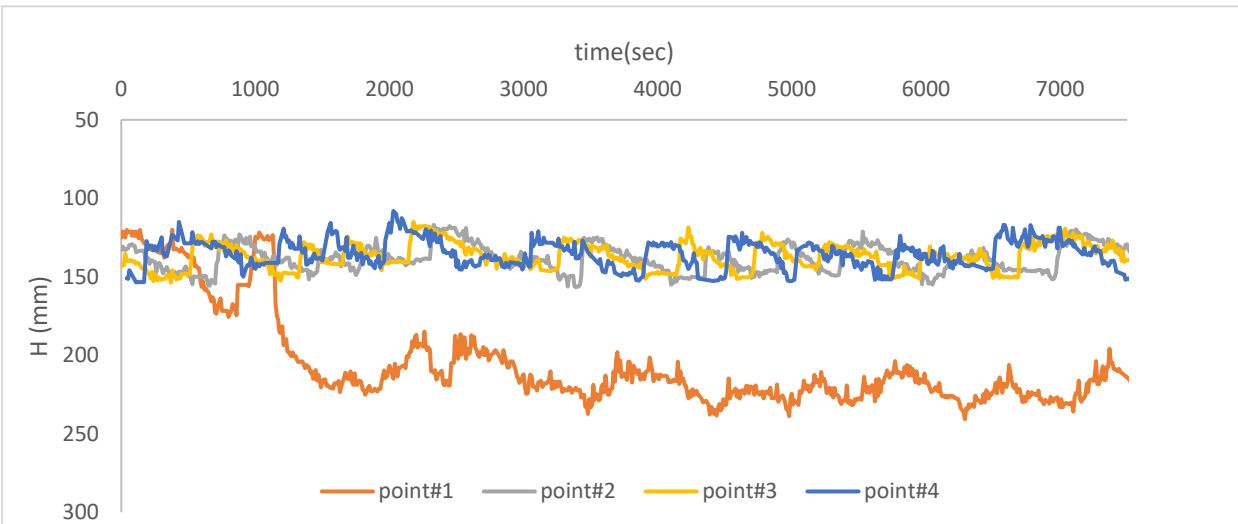

Figure (4- 12): Experiment E1 measurements.

A new position of lasers was introduced in experiment E2 to investigate the characteristics and geometry of the scour hole using that new placement of the measuring points, three points were placed close to the pier where the scour hole is formed, while the last one was placed relatively distant upstream of the pier. Figure (4-13) shows the scour hole fluctuation inside the scour hole and on its edge to have a bed fluctuation profile at those spots; however, the fourth point was far upstream from the pier to measure the dunes' fluctuation. The location of points (1,2,3 and 4) was (2.5,7.5,13.5 and 48 cm) upstream of the pier nose, respectively. The data were taken for calculating the amplitude, were the time increment from 8000s to 13160s for all the measuring points.

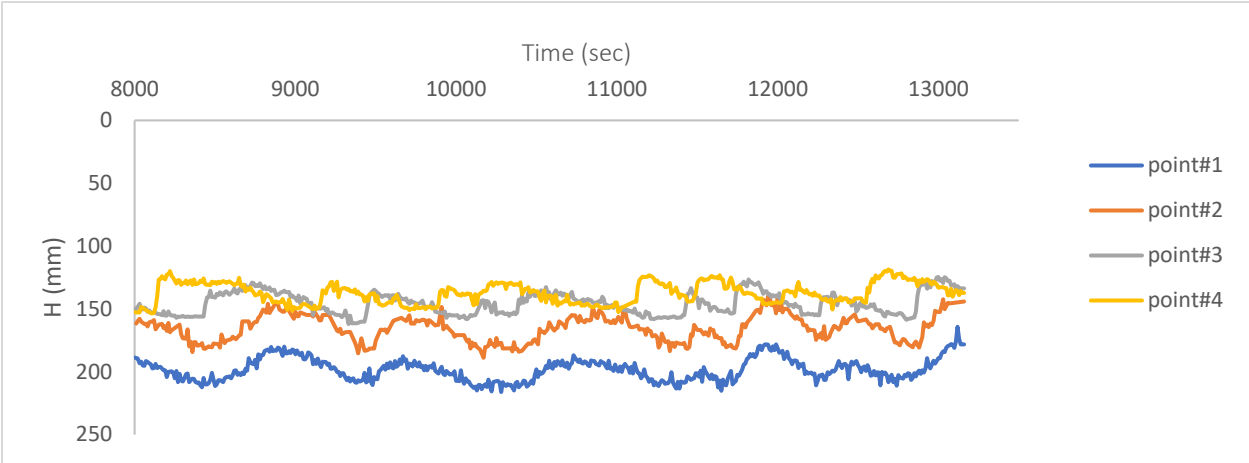

Figure (4- 13): Experiment E2 measurements.

The change of the dune shape is noticed in the previous figure, as the dunes upstream of the scour hole has a triangular shape with steep from and mild tail, while a deformation of the dunes into a more rounded shape is started on the inclined surface of the scour hole before arriving to the bottom of the hole.

Another argument raised on the interdependency of the scour fluctuations and the incoming dunes. For example, Melville (1984) stated that the scour fluctuation corresponds to the dunes through the scour hole. However, Jain and Fisher (1979) mentioned that the scour fluctuations were not always consistent with the passing dunes. a mechanism of dune coalescence was hypothesized by Radice and Lauva (2017) based on the union of consecutive bed-forms as indicated by Ballio et al.(2010), by assuming that the horseshoe vortex could be strong enough to erode the small dunes so that they could be reached by the following ones and merge with the latter into a larger dune. However, the spatial records show that the change of the dunes shape occur gradually as soon as they enter to the scour hole, that behavior may be has no dependency on the horseshoe vortex but a mechanism of sediment avalanche occurs on the hole slope due to the dune's load exerted on the hole edge , that can be investigated deeper in the analysis of slope stability.

By combining the points of both experiments (E1 and E2), we can have a spatial representation of dimensionless amplitude values (Δ_{ds}/b and Δ_d/b) through the bed profile. The amplitude of the scour depth as well as dunes were computed based on probability ranges (80%,90%,95% and 98%) as shown in figure (4-14), as the points depicted placed at 0.5, 2.5, 7.5, 25, 48, 116 cm from the pier face.

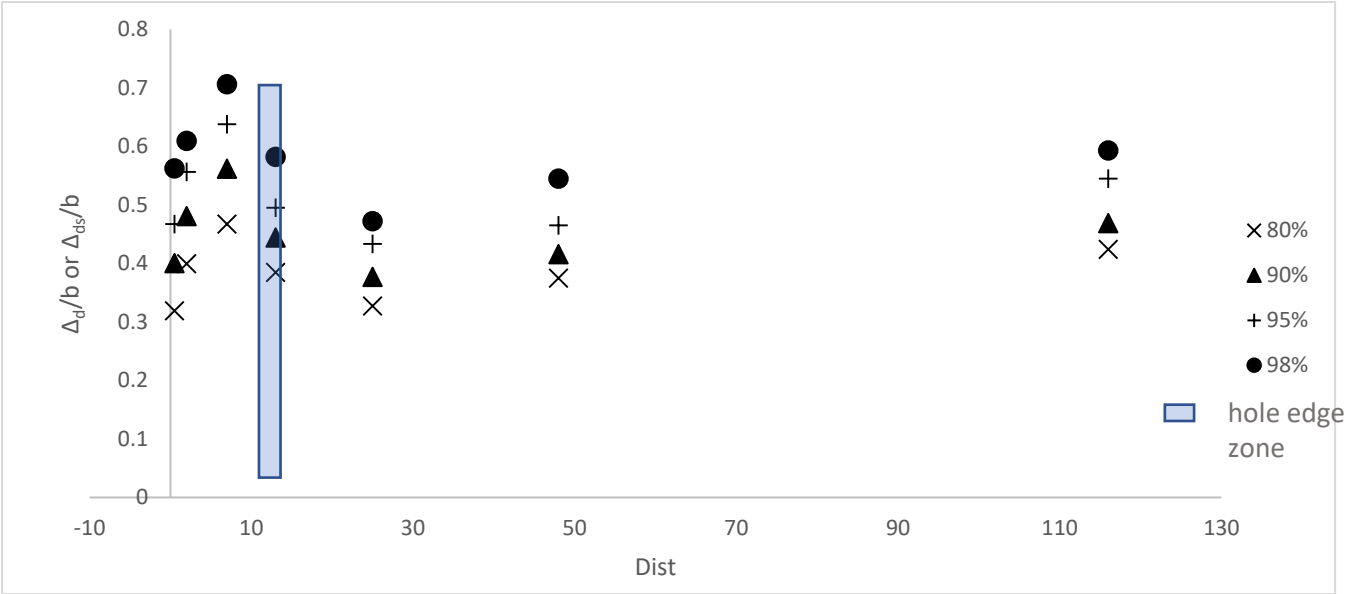

Figure (4- 14): Dimensionless amplitude profile for Q=1.4Qc.

Unlike E1 and E2, for experiments E3, E4 and E5 the measuring points were located totally inside the scour hole and on its edge to investigate the evolution of the scour hole and the depth fluctuation inside. The first point was placed at 0.5 cm from the pier; while the second one was 2 cm distant from the first one, the third one is 5 cm from the second, and the forth one is located 6 cm away from the previous point to be located just upstream of the hole. For E3, the measuring points were aligned along the hole stream wise axis; however, E4 and E5 are inclined 450 to the right direction and 450 to the left direction, respectively.

E3, E4 and E5 were set up to run under the condition of discharge Q=18.433 l/s; where Q/Q_c=1.4. The flow was adjusted, and the experiments started for 4190 seconds prior to the pier lifting to let the bed to be flattened. At time of 4190s the pier was lifted, and scour hole started to form up to reach the equilibrium state, thereby, equilibrium condition was reached, and bed fluctuation is obtained within the time span after the equilibrium time until 9590s for E3. Additionally, E4 and E5 were run for the time periods of 4550s and 5570, respectively.

Figure (4-15) represents the measures obtained by the measuring points 1,2,3 and 4 for E3 fixed at 0.5 cm, 2.5 cm, 7.5 cm, and 13.5 cm, respectively.

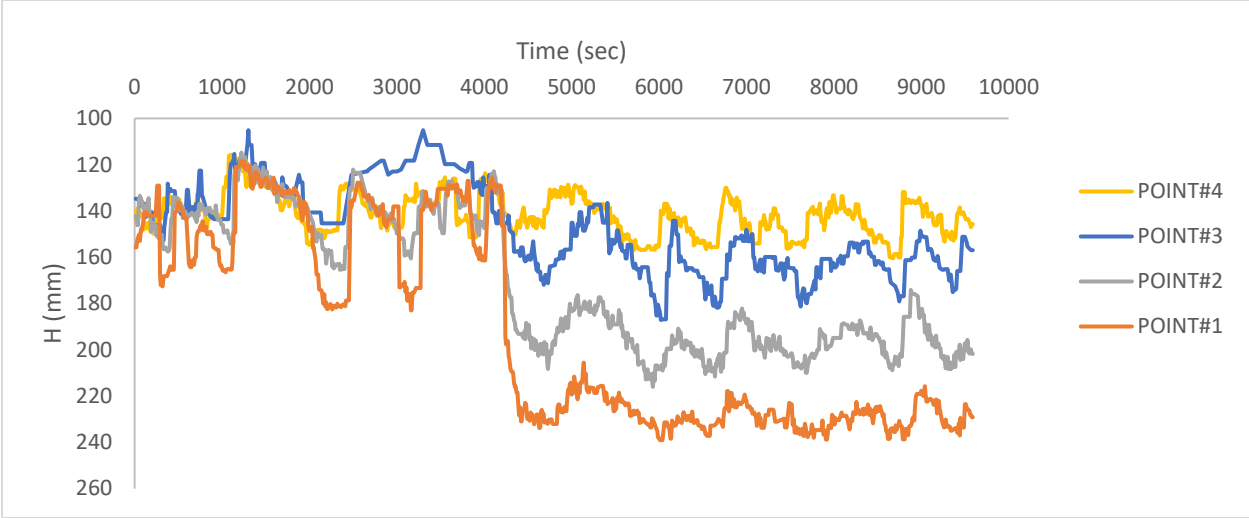

Figure (4- 15): Experiment E3 measurements.

For E4, the measuring points were inclined by 45º to the flow direction to the right side of the channel to observe the change of the scour hole shape with time. Figure (4-16) represents the measures obtained by the measuring points for E4.

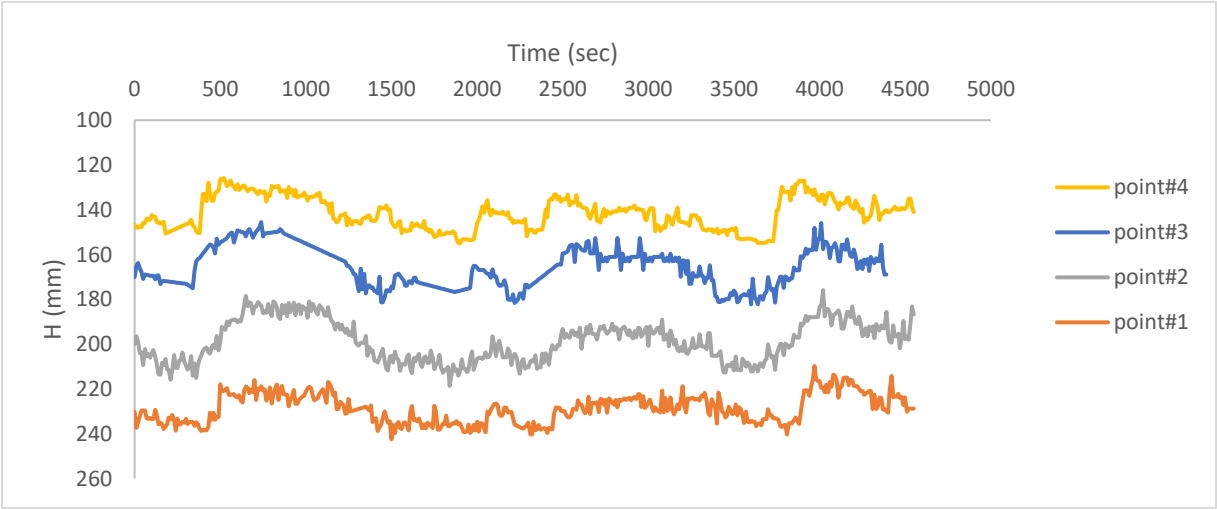

Figure (4- 16): Experiment E4 measurements

Noting that the acquired data at point#3 is not so reliable because of high existence of anomalous records. However, it clearly represents the fluctuation of the scour hole at 7.5 cm from the pier nose.

Like E3, a gradual change in the dune shape is observed between point#4 that located on the edge of the scour hole and point#1 that is located at the bottom of the scour hole to be more flattened and smooth.

For E5, the measuring points were inclined 45º the flow direction towards the left side of the channel to observe the change of the scour hole shape with time. Figure (4-17) illustrates the data records obtained by the measuring points.

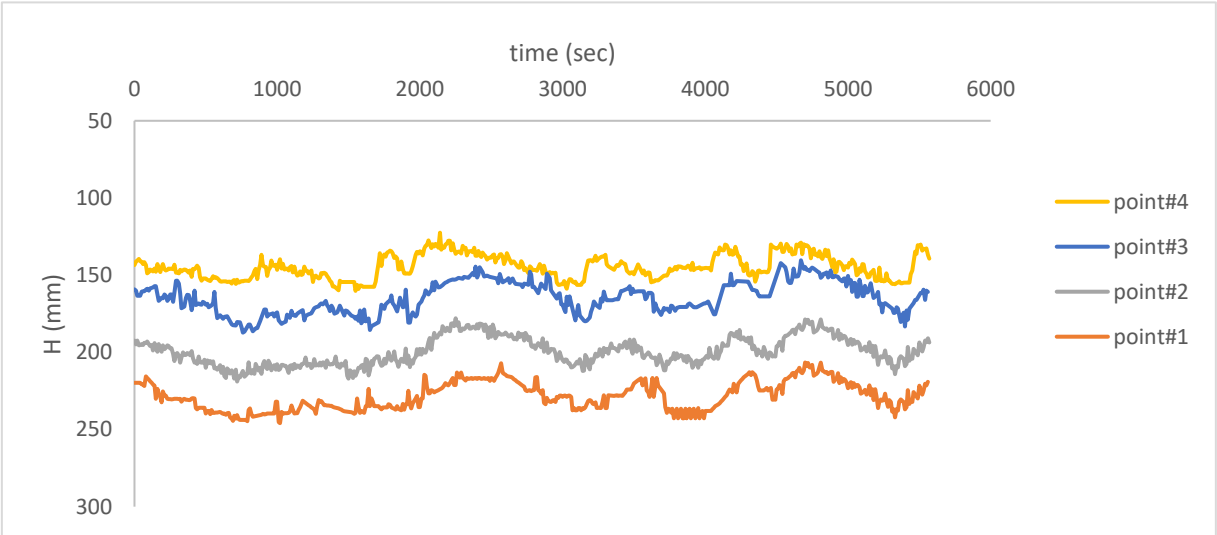

Figure (4- 17): Experiment E5 measurements.

Therefore, for all the directions, the dunes reshape is happening on the beginning of the inclined surface before the arrival to the vortices area at point#1 that is located at the bottom of the scour hole.

For computing the amplitude of probability ranges (80%,90%,95%, and 98%), a period has been chosen between 6080s and 9080s for all the placed measuring points for E3. However, for E4 and E5, the whole-time period of the run was considered in the calculation of the amplitude. Figure (4-18) depicts the calculated amplitude with respect to pier diameter (b) for different probability ranges for the three experiments at all the placed measuring points.

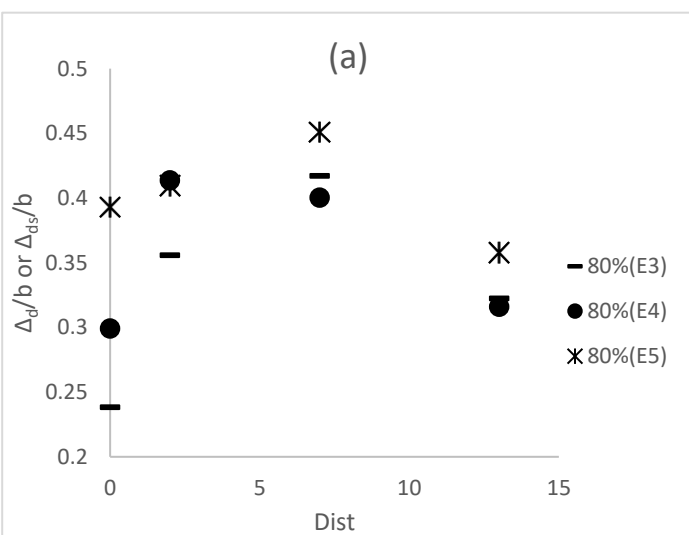

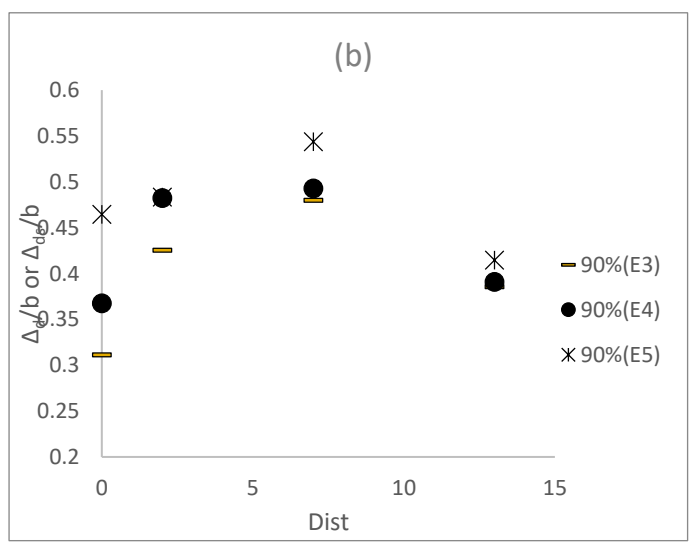

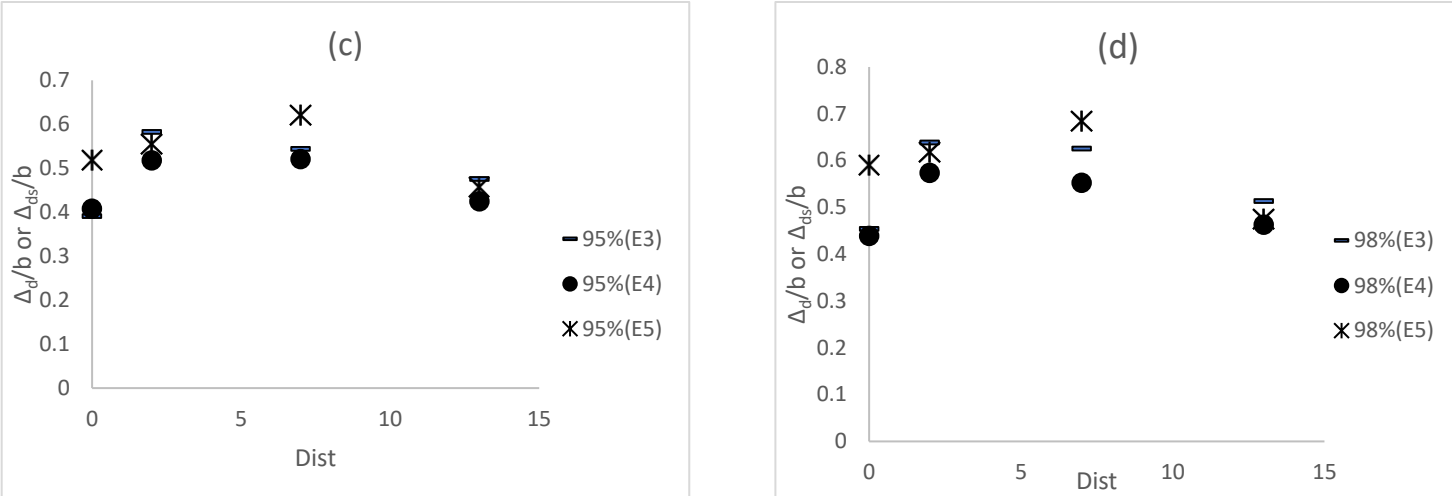

Figure (4- 18): Dimensionless amplitude for measuring points of E3,E4 and E5;(a) probability range 80%,(b)probability range 90%, (c)probability range 95%,(d) probability range 98%.

The results demonstrate that for the probability range of 80%, at points 2, 3 and 4, the amplitude values are in the same range and highly similar; however, at point 1, the amplitude values are slightly different for the three positions, and Similarly for the probability range of 90%. For 95% and 98%, the amplitude values for the third position E5 is slightly different at the nearest point to the pier as the highest amplitude is always calculated at E5 compared to the other positions, also the point that located 7.5 cm upstream of the pier face. Therefore, mostly at all the points upstream of the pier, have the same fluctuation behavior at the three imposed positions. However, the fluctuation at the pier face varies based on the direction of the incoming dunes. Additionally, the amplitude values on the inclined surface of the scour hole are always higher than those points in front of the pier and upstream of the hole.

In conclusion, the amplitudes for all the probability ranges inside the scour hole, are an increasing function of the distance. However, for most probability ranges, the points at 0.5 cm from the pier nose and upstream of the hole edge have the same range of amplitude values. Therefore, the pattern of scour fluctuation is induced by the bed-forms upstream of the hole and passing through it. In contrast, the amplitude values on the inclined surface have no strong relation with the approaching dunes nor the scour depth, that can be related significantly to the sliding mechanism of the dunes into the scour hole that is not consistent with the migrating behavior upstream of the hole and the accumulation and erosion occur at the horseshoe vortex zone in front of the pier.

Different flow discharge with its equilibrium sediment feeding was applied for E6 and E7, the new discharge is Q=21.12 l/s (1.6 Q_c). The equilibrium sediment feeding was adjusted and the allocated time for experiment E6 was 7285 seconds, and 4395 seconds for E7. The experiments were set up to analyze the scour depth as well as the dune formation. Thus, the lasers positioning in E6 was the same as E1 where the first

point placed at 0.5 cm from the pier followed by the second one that is distant by 25 cm upstream, and in the same direction, points 3 and 4 were placed on distance of 48 cm and 116 cm from the pier nose respectively. However, for the investigation of the scour hole and scour depth under the new condition of water discharge, E7 was set up with the same approach of E3 by placing all the lasers in the scour hole and on the edge of the hole. Point1 was placed at the face of the pier, while points 2 to 4 were placed on distances (2.5, 6.5 ,10.5 cm respectively) from the pier face as shown in table (4-2).

For E6, the variation of the scour depth and the bed elevation was observed by the four placed lasers. Firstly, the adjustment of the bed lasted for 3340 seconds when the bed became even, consequently, the pier was lifted, and the scour hole started to develop. The evolution of the scour hole and its variation was measured until 7285 after the starting of the experiment as illustrated in figure (4-19).

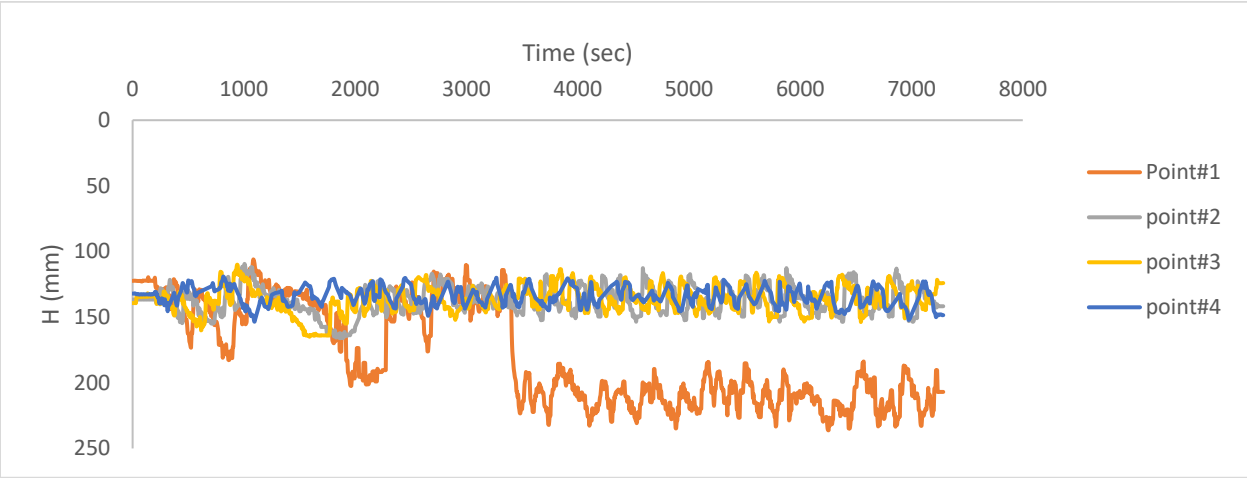

Figure (4- 19): Experiment E6 measurements.

At 3400 seconds, the pier was lifted after bed adjustment, a progressive scour was rapidly formed around the pier.

E7 was conducted for 4395 seconds, and bed adjustment lasted for 1900s before the pier lifting. Figure (4-20) shows the records of the four lasers throughout the experiment that show the variation of the bed elevation and scour depth evolution.

Due to the high flowrate (1.6 Q_c), the change of the dunes' shape between the edge of the scour hole and the bottom of the scour hole is not significant, unlike the lower flowrate (1.4Q_c) where the change of dunes' shape inside the hole was evident. This behavior can be explained by either the time that spent by the dune inside the hole is not adequate to induce any shape variation, or the size of the dune is relatively big compared to the scour hole that consequently dominates the scour hole; therefore, no tangible change of the dune characteristics inside the hole can be noticed.

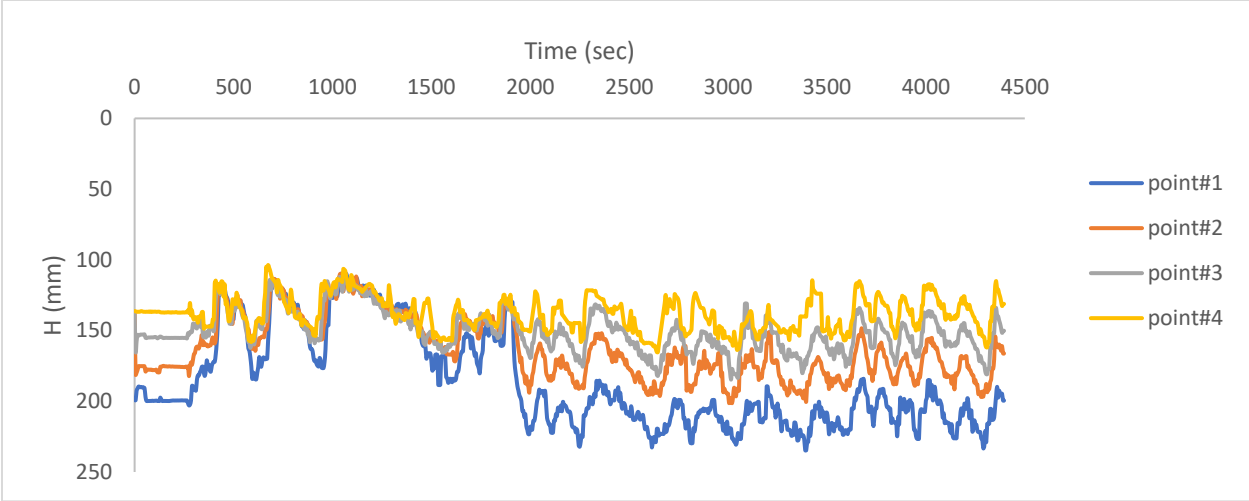

Figure (4- 20): Experiment E7 measurements

The amplitudes for probability ranges (80%, 90%, 95% and 98%) were calculated based on the increment from 4000s to the end of the experiment 7285s for E6 and from 2500s to the end of the experiment 4395s for E7.

By combining E6 and E7, figure (4-21) depicts a spatial profile of a dimensionless amplitude values at different points upstream of the pier.

Figure (4- 21): Dimensionless amplitude profile for Q=1.6Qc

For all the probability ranges, the highest amplitude is present at the points placed inside the scour hole and on its edge, while the lowest amplitude is observed at the furthest point from the pier (116 cm). Therefore, the amplitude value of the dunes is a decreasing function of the distance upstream of scour hole due to the gradual evolution of the migrating dunes spatially when they are approaching the scour hole. However, the same amplitude values are present on the scour hole edge and within the scour hole because of the domination of the dune on the scour hole,

In comparison with amplitude values corresponding to discharge 1.4Q_c, they are always higher for all the probability ranges due to higher fluctuation of the dunes upstream of the hole as well as the scour fluctuation inside the scour hole.

Amplitudes comparison based on discharge value.

The analysis was performed for both distant placement as well as close placement of the measuring points to understand the similarity level between the scour depth fluctuation and the bedforms.

Measuring points placed upstream of the scour hole.

The placement of the four measuring points is at 0.5 cm from the pier nose, 25 cm ,48 cm and 116 cm upstream of the pier. Figure (4-22) shows the amplitude of probability ranges (80%, 90%,95% and 98%) for both discharge values carried out in the experiment.

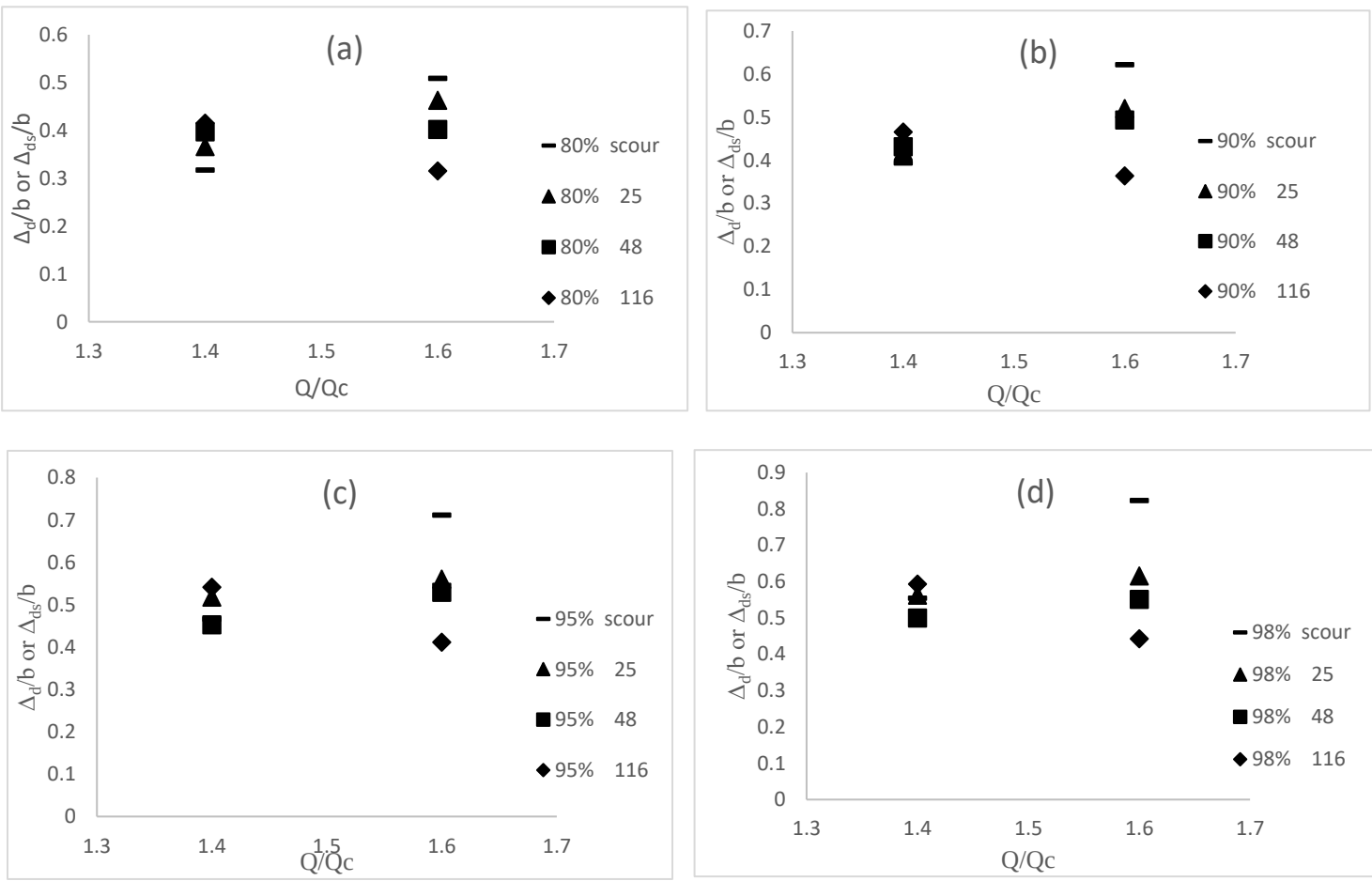

Figure (4- 22): Dimensionless amplitude at far distances for different discharge;(a) probability range 80%, (b) probability range 90%,(c) probability range 95%, (d) probability range 98%.

For all the probability ranges at discharge Q=1.4 Q_c, amplitude values at all the points are in the same range; therefore, the fluctuation of the scour depth are induced by bed-forms entering the scour hole and passing through it, and the failure mechanism on the hole does not affect on the interrelation between the dunes and the scour depth fluctuation. Instead, for Q=1.6Q_c, the difference of the amplitude is high except for points placed at 25 and 48 cm. Having less amplitude at the furthest point is due to variation in developing dunes between the beginning of the channel and at a mediocre distance from the pier; therefore, the dunes are gradually developing as a function of the distance, these developed dunes have no big influence on the scour variation that highly induced by the mechanism of sediment sliding on the scour hole.

Measuring points placed within the scour hole.

The placement of the four measuring points is slightly changed based on the discharge value, for Q=1.4Q_c, the hole is wider, consequently, the points are located at 0.5 cm from the pier, 2 cm, 7 cm and on the edge of the hole (13cm) upstream. However, for Q=1.6 Q_c, the scour hole is narrower, and the placement will be at 0.5 cm, 2 cm, 6 cm, and on the edge of the hole (10 cm) upstream of the pier. Figure (4-23) shows the amplitude of probability ranges (80%, 90%,95% and 98%) for both discharge values carried out in the experiment.

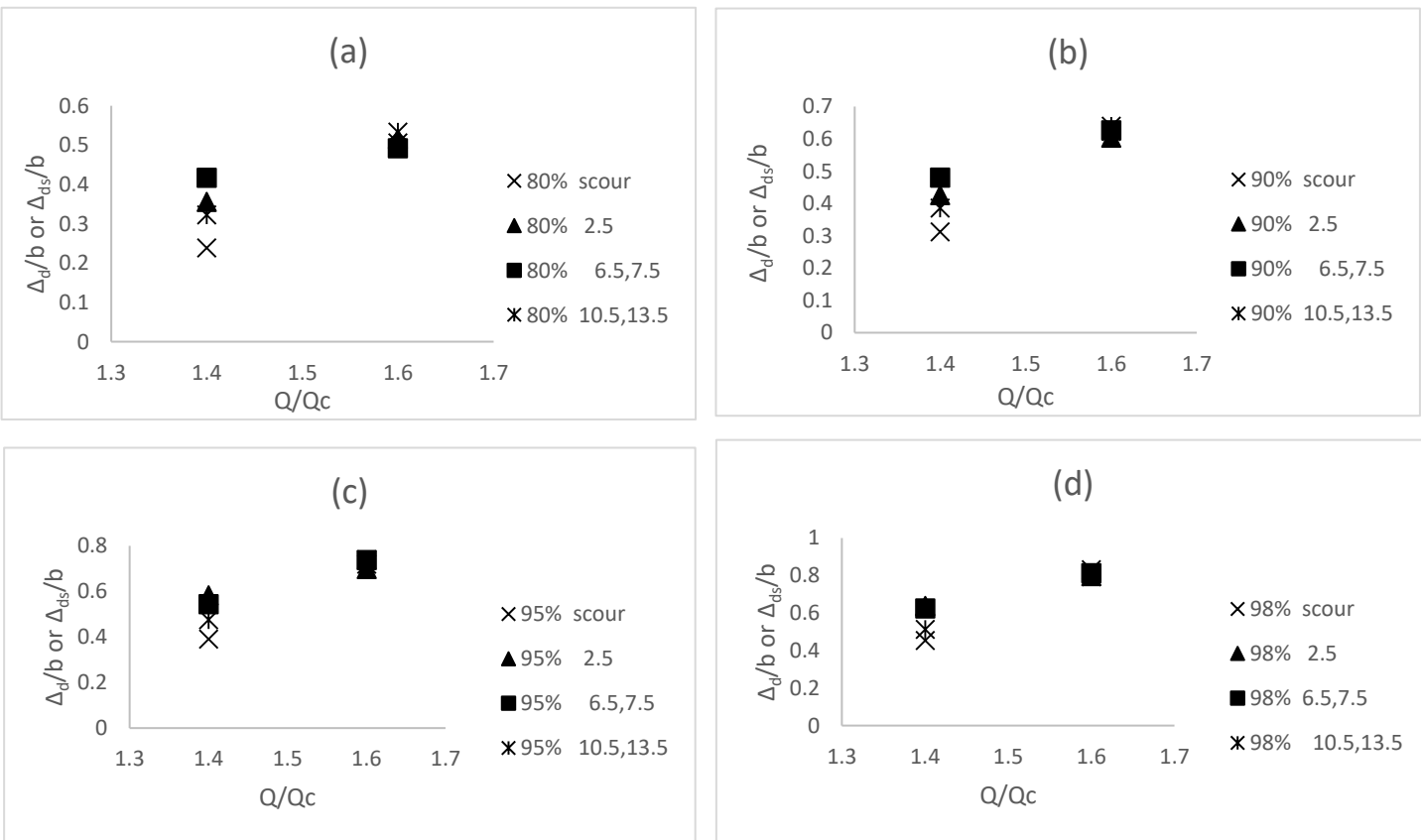

Figure (4- 23): Dimensionless amplitude at close distances for different discharge;(a) probability range 80%, (b) probability range 90%,(c) probability range 95%, (d) probability range 98%.

The amplitudes of the points within the scour hole are not highly overlapping in case of lower discharge (Q=1.4 Q_C). However, for higher discharge (1.6Q_c), the points are similar and overlapping while the hole is smaller. Because of higher speed of the flow with faster dunes and smaller scour hole, the time that a dune spends inside the hole is not enough to perform any tangible variation in its shape as well as the relatively big dunes to scour hole may interpret the high similarity of points' amplitude values inside the hole.

For lower discharge value(Q=1.4Q_c), the amplitudes of all points in the system are strongly related and the fluctuation of the scour depth is clearly induced by the bed-forms. On the contrary, for higher discharge value (Q=1.6Q_c), the bed-forms have no effect on the scour depth, as each of them follows a separate trend.

4.2.3. scour hole slope analysis.

The analysis of temporal variation the scour hole slope is due to the observed different patterns of fluctuations at different points as shown beforehand. To understand this behavior, four experiments (E3, E4, E5 and E7) were dedicated to investigating the scour hole slope characteristics.

Slope with time

The analysis of temporal slope variation was done on experiments E3, E4 and E5 to find out the difference in the scour hole slope in different directions. Figure (4-24) depicts the slope variation measured in degrees with time for the three positions introduced in E3, E4 and E5.

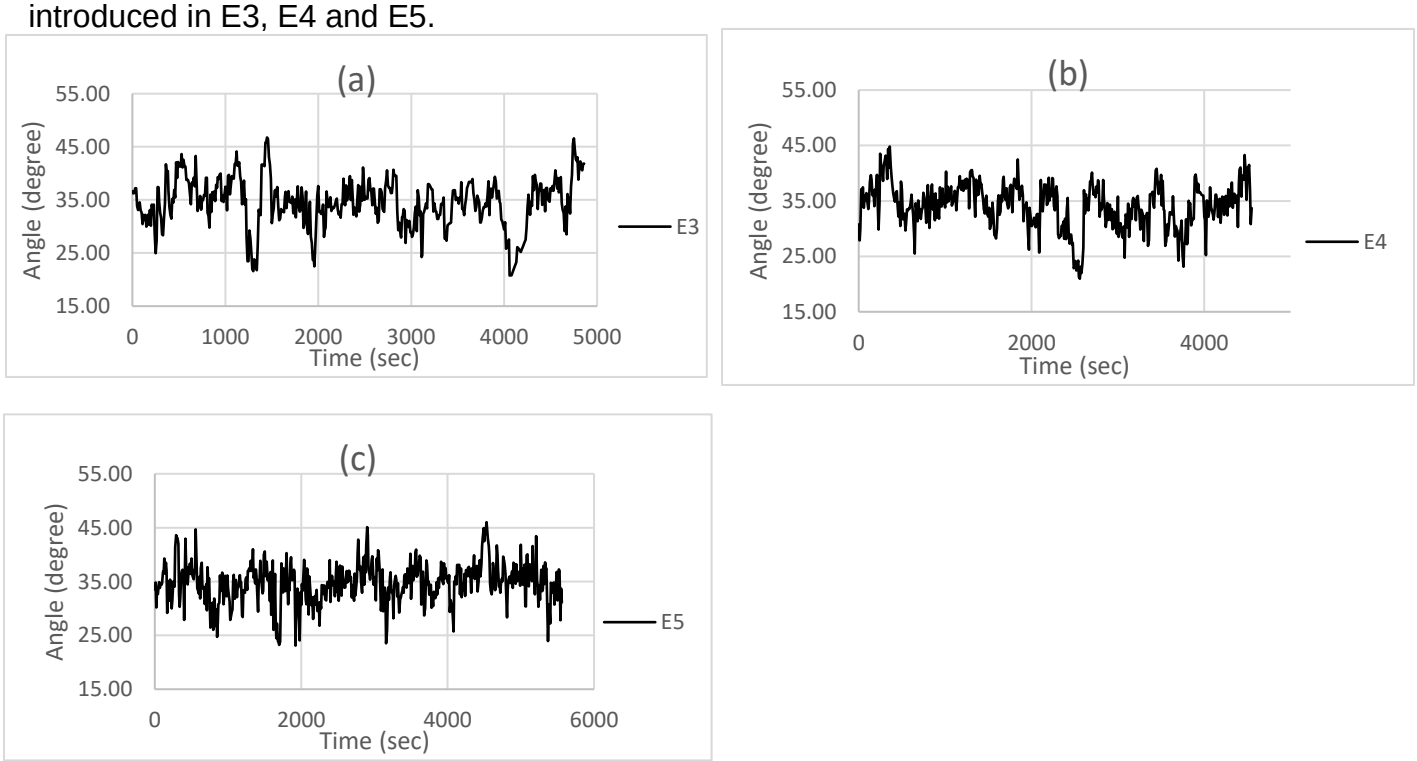

Figure (4- 24): Temporal scour slope variation at different directions;(a) on the central axis, (b) on 45o inclined direction to the right side, (c) on 45oinclined direction to the left side.

Clearly, the trend of slope variation is uniform, as it starts to increase gradually before the arrival of the new dune because of the horseshoe vortex that exert an entrainment force on the bottom part of the scour hole that results in increasing the slope. At the time of dune load exerted on the scour hole edge and instant sediment avalanche occurs, a sudden decrease of the slope observed until it passes the hole, thereafter, the slope starts to increase again.

Figure (4-25) illustrates comparatively the values of mean, maximum and minimum of scour hole slope for the three imposed positions.

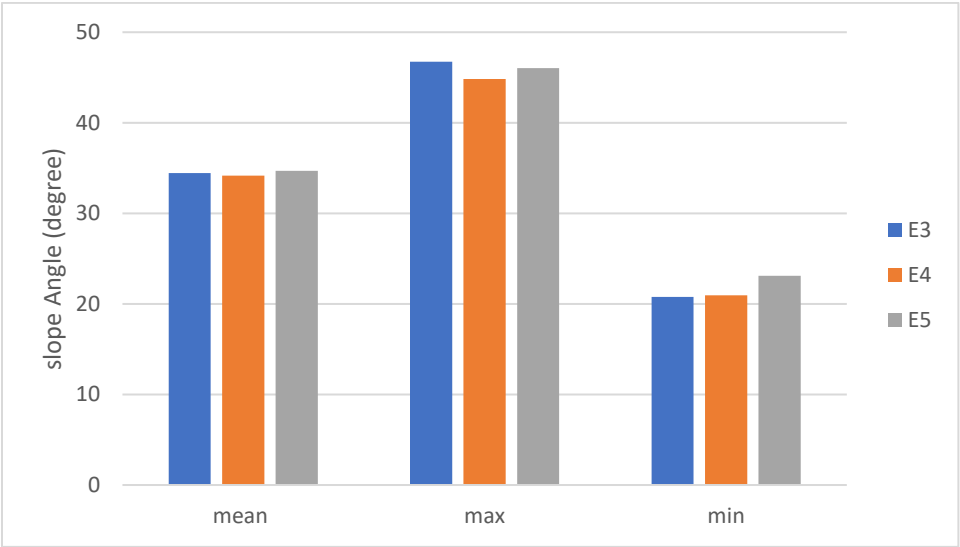

Figure (4- 25): Scour slope mean, minimum and maximum values at different directions.

No significant difference between the values of mean, maximum and minimum between the three positions. Therefore, the falling behavior of the migrating dunes inside the scour hole is highly similar in the three imposed directions. Additionally, the scour hole slope was computed for the higher flow rate ($1.6Q_c$). Figure (4-26) illustrates the mean, maximum and minimum temporal scour slope variation.

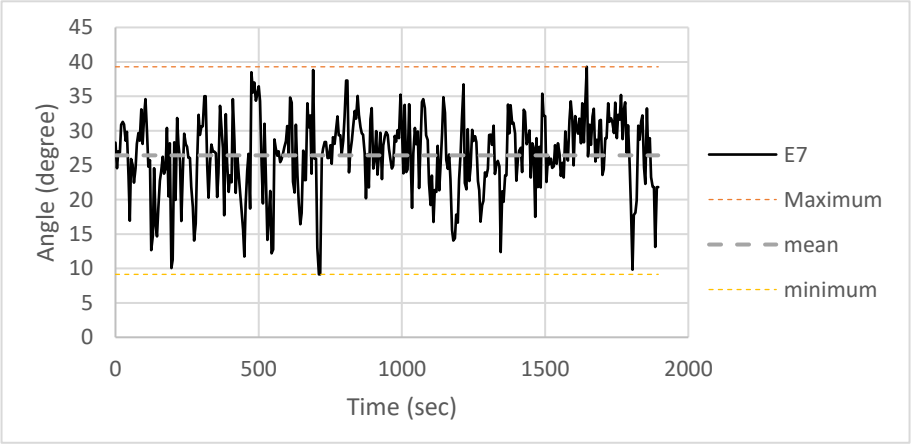

Figure (4- 26): Scour slope variation during E7.

Obviously, the slope variation in higher flow rate is rapidly varying due to the higher dune celerity entering and leaving the scour hole.

The comparison of slope values between E3 and E7 is shown in figure (4-27). The scour hole slope is a decreasing function of the flow rate, which implies that the scour hole for discharge $1.6Q_c$ is always shallower than this of discharge $1.4Q_c$.

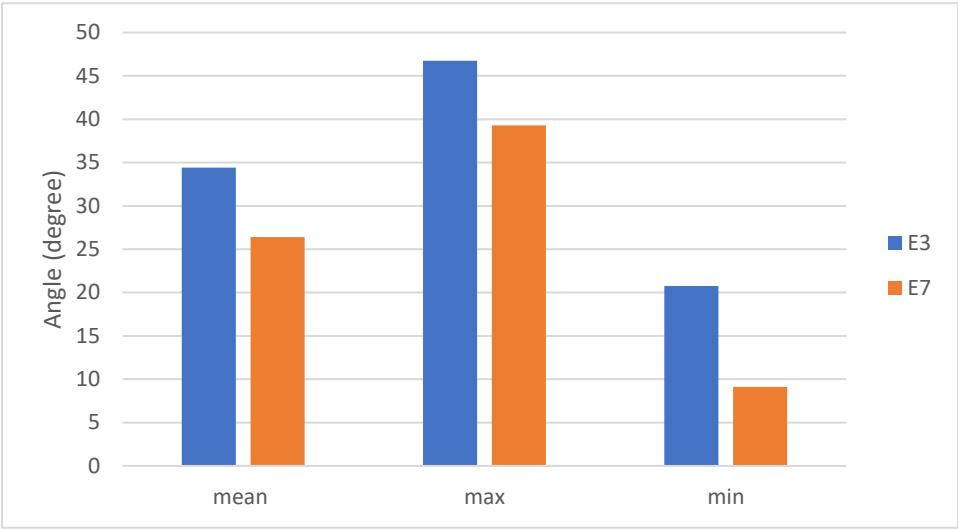

Figure (4- 27): Scour slope comparison between E3 and E7.

Scour hole slope vs scour depth

The analysis of the dependency of the scour hole slope on the scour depth at different points inside the scour hole and on its edge was performed by plotting the slope variation with the water depth at each measuring point. For the four experiments E3, E4, E5 and E7, the measuring points were placed at 0.5 cm from the pier, on the edge of the hole and two measuring points were inside the hole to allow the computation the temporal slope variation. Figure (4-28) represents the variation of the slope with depths of the four measuring points for experiment E3. Where, points 1, 2, 3 and 4 are placed at 0.5 cm, 2.5 cm, 7.5 cm and 13.5 cm upstream of the pier as mentioned in table (4-2).

Due to the high level of noise that associated with the series, a method of barycenter was introduced to have a relatively clear trend of the relation between points' depths and slope.

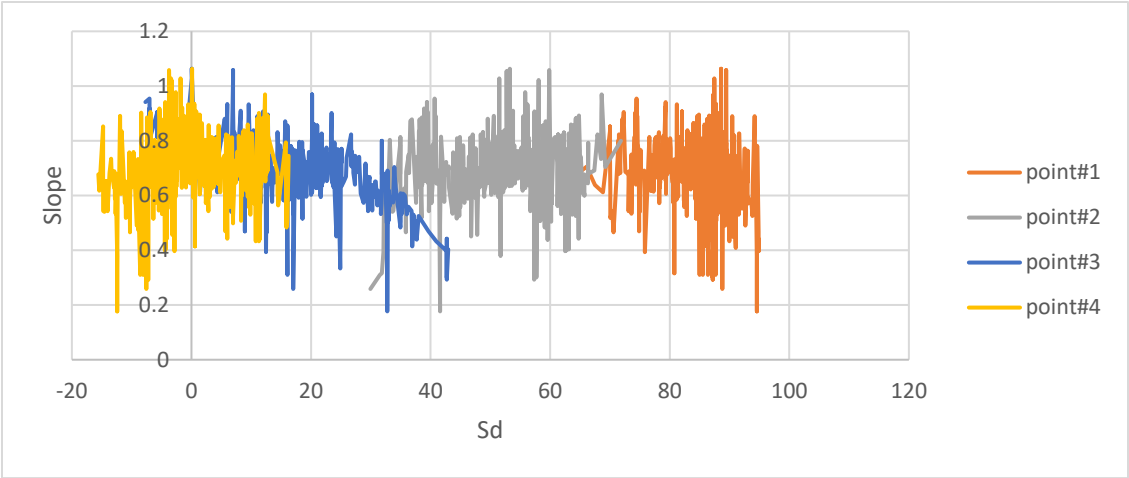

Figure (4- 28): Scour slope variation with scour depth at different point.

The method of barycenter is dividing the data series to a set of intervals and compute the mean slope of each depth interval. Figure (4-29) shows the relation between points' depths and scour hole slope with a refined linear trend.

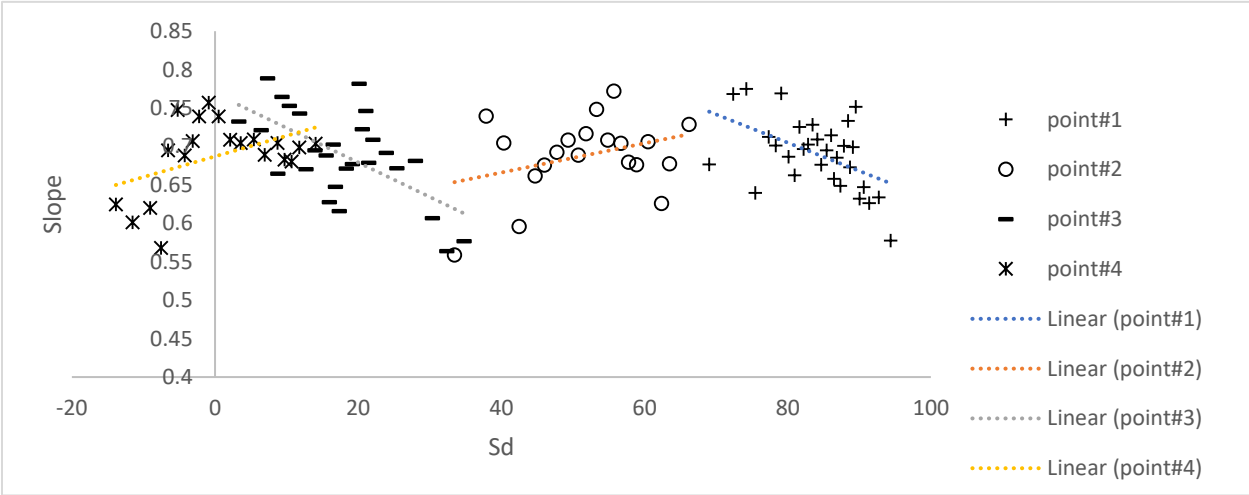

Figure (4- 29): Slope variation trend vs scour depth at points within the scour hole in E3.

Knowing that points 2 and 3 are placed on the inclined surface and used to compute the slope of the inclined surface as a representation of the scour hole slope, while point#1 is installed directly in front of the pier nose and point #4 is placed on the edge of the scour hole. Consequently, increasing the scour depth of point#2 results in increasing the slope; however, increasing the scour depth of point#3 leads to decrease the slope. points 1 and 4 were not involved in the calculation of the slope of the hole, and they are following different trends than the closest point to each of them. This change of trend can be interpreted, when the dune front arrives at the scour hole edge, the sediment avalanche on the hole surface starts to occur, thereby, the crest slides with the sliding mass, and consecutive points of the crest are present at point#4, while at point #3 instead, the highest depth is exist due to the translation of the mobilized volume that

leads to a sudden decrease in the slope and increasing in the scour depth at point#3. When the avalanche arrives at point#1, it exerts control over the scour depth to be undermined, consequently, the scour depth decreases while the slope increases due to the sediment displacement from point #2 to point#1 until the sediment particles washed out by the horseshoe vortex, while the slope is peaking.

The same trend and behavior of depth-slope relation was observed for the other two experiments (E4 and E5), therefore, the same behavior is followed at all the directions upstream of the cylindrical pier.

This interrelation and scour depths was carried out for experiment E7. where Q=1.6 Q_c as figure (4-30) shows the trend after applying the method of barycenter.

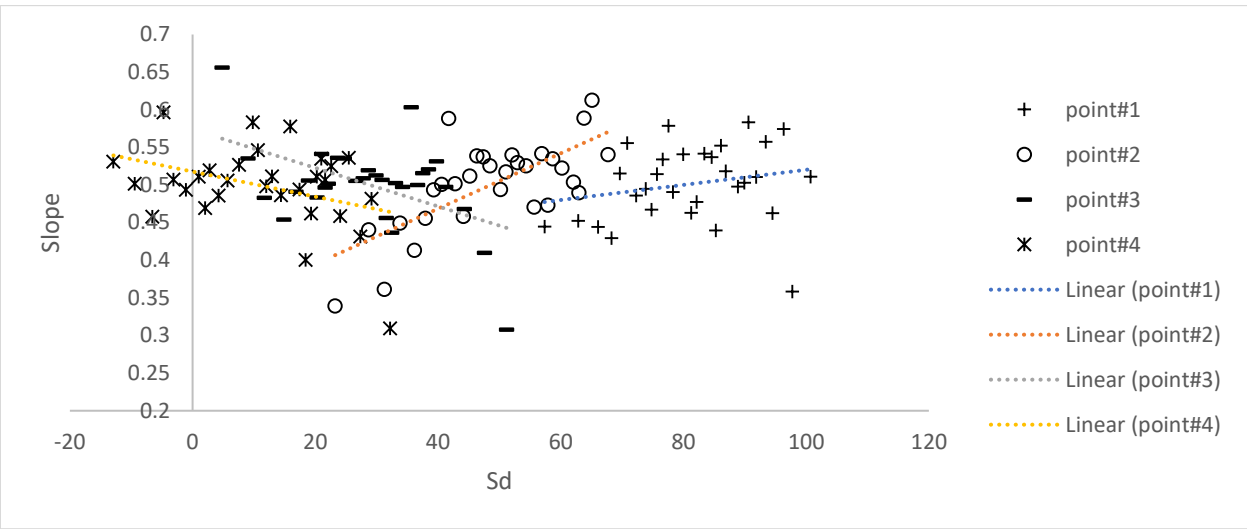

Figure (4- 30): Slope variation trend vs scour depth at points within the scour hole in E7.

Like the experiments of Q=1.4Q_c, points 2 and 3 have the same trend, as the slope is an increasing function of the scour depth at point 2 ; however, it is a decreasing function of scour depth at point#3. On the other hand, points 1 and 4 have same behavior as points 2 and 3, the only difference between points 1 and 2 as well as points 3 and 4 is the slope of trend line that implies that the dune size is relatively big and fast; therefore, the migrating dune can occupy two consecutive points at the same time but with a difference in the dune's height (crest or tail).

Scour hole slope stability analysis (geotechnical modeling).

To explain the slope variation of the scour hole and the sediment failure occurring within the hole, a simplified geotechnical model is introduced based on the Fellenius method. Figure (4-31) represents a schematic view of the scour hole in the flow direction before the arrival of dunes.

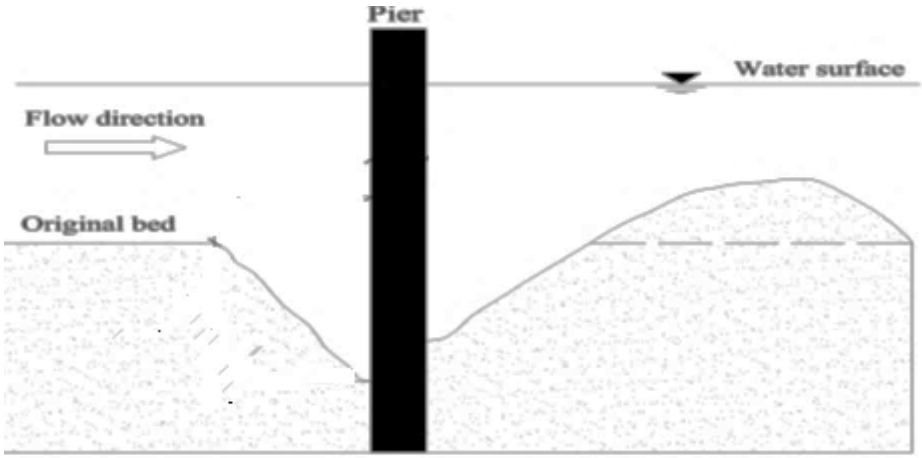

Figure (4- 31): Schematic of scour hole in flow direction (Wu et al,2016).

is almost at the edge of the hole. The sediment avalanche starts to move when the safety factor is at unity. The factor of safety is commonly thought as the ratio of the maximum shear stress that soil can sustain to the mobilized shear stress along a given failure surface. Referring to figure (4-32) the factor of safety Fs, with respect to strength, may be expressed as follows:

$$F_S = \frac{\tau_{ff}}{\tau}$$

where τ_{ff} is the maximum shear stress that the soil can sustain at the value of normal stress of σ_n, τ is the actual shear stress applied to the soil.

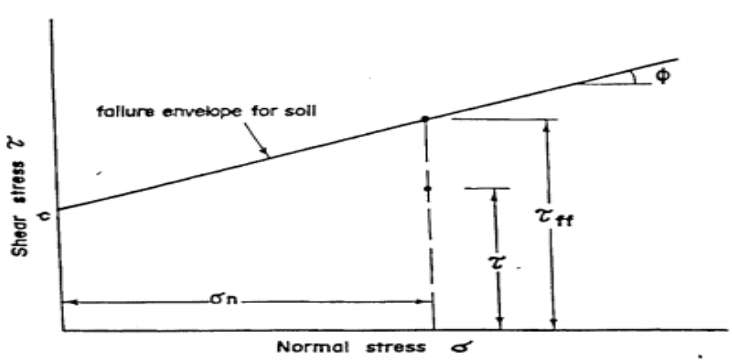

Figure (4- 32): Definition Diagram for Factor of Safety.

The assessment of the mobilized volume and the critical surface is based on the 2D Fellenius method as the simplest approach of methods of slices. In the method of slices,

the sliding mass above the failure surface is divided into a number of slices as shown in figure (4-33). The forces acting on each slice are obtained by considering the mechanical (force and moment) equilibrium for the slices as illustrated in figure (4-34).

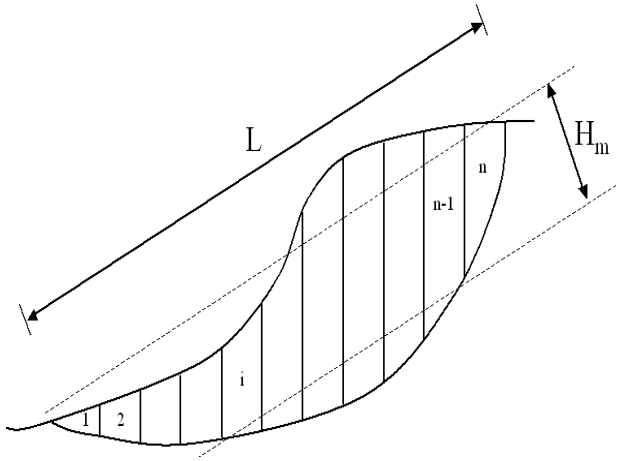

Figure (4- 33): Dividing the sliding mass into n slices

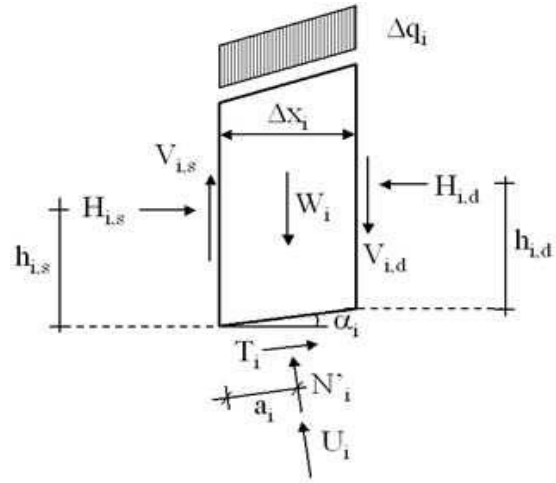

Figure (4- 34): Forces acting on each slice.

Where $V_{i,d}$ and $V_{i,s}$ are the shear forces acting between adjacent elements, $H_{i,d}$ and $H_{i,s}$ are the total normal forces on the sides of the element, T_i is the shear force on the base, N'I is the normal force on the base, U_i is the water pressure at the base and Δq_i is the external distributed load.

In Fellenious method, the simplification has been made by assuming that:

- Circular failure surface
- a_i is a half of the base $\Delta x / 2cos\alpha i$
- $H_i = V_i = h_i = 0$ (neglecting the interaction between the slices).

The equations that are used in the calculation of Fs (safety factor) are:

- Local equilibrium of each slice along N direction.

$$W_i \cos\alpha_i = N'_i + U_i$$

- Failure criterion at the base of each slice.

$$T_i = \frac{1}{Fs}\left[\frac{c'\Delta x}{\cos\alpha_i} + (W_i \cos\alpha_i - U_i)\tan\phi'\right]$$

- Global rotational equilibrium of the soil mass.

$$R \cdot \sum W_i \sin\alpha_i = R \cdot \sum T_i = \frac{R}{Fs}\sum \frac{c'\Delta x}{\cos\alpha_i} + (W_i \cos\alpha_i - U_i)\tan\phi'$$

Consequently, the safety factor can be determined explicitly by the following formula:

$$Fs = \frac{\sum \frac{c'\Delta x}{\cos\alpha_i} + (W_i \cos\alpha_i - U_i)\tan\phi'}{\sum W_i \sin\alpha_i}$$

The geometry of the scour hole and the original bed were determined based on the measurements recorded at different positions within the channel. The depth of the scour hole measured from the bottom of the hole till the original bed is 12 cm, the stable slope before the arriving of dune is 40° that is obtained by the temporal variation of the slope shown in figure (4-24).

The main mechanical parameters of the used non-cohesive (c'=0) sample are as shown in table (4-6):

γ_{wat}	9.81	kN/m3
ρ_s	1311.70	kg/m3
γ_{dry}	12.87	kN/m3
p	0.40	-
γ_{sat}	16.79	kN/m3
γ_{eff}	6.98	kN/m3
Φ_s	40.00	°

Table (4- 6): The main mechanical parameters.

Where (γ_{wat}) is the specific weight of water, (ρ_s) is the sediment density, (γ_{dry}) is the specific weight of dry sediment, (p) is the porosity, (γ_{sat}) is the saturated unit weight, (γ_{eff}) is the effective unit weight and (Φ_s) is the friction angle. The angle of repose measured in dry condition is 31.5°; however, the failure criterion for non-cohesive soil layer at very low confining stresses is reported in literature to be higher than the angle of repose (as an effect of the curved failure envelope in the Mohr-Coulomb plane). Therefore, the friction angle was decided to be the same as the scour hole slope (40°) before the arrival of the dune.

The slope failure is induced when a dune is existing on the scour hole edge. The loading dune's geometry was measured based on the measuring points placed on the scour hole edge and upstream of the hole to determine its height and length as illustrated in table (4-7) and figure (4-35).

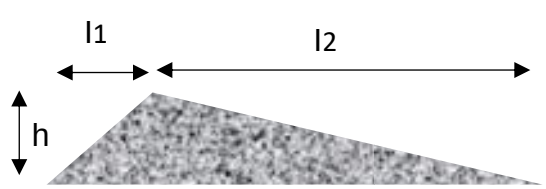

Figure (4- 35): Dune's dimensions' parameters

Xd [m]	0.14
h [m]	0.04
l1 [m]	0.02
l2 [m]	0.80
q_{max} [kPa]	0.265

Table (4- 7): Dune's dimensions and load.

Where h is the dune's height, l1 is the distance of the front, l2 is the distance of the tail and q_{max} is the load exerted by the dune ($=\gamma_{eff} * h$).

Figure (4-36) represents the geometry of the scour hole and the bed upstream of the scour hole as well as the distribution load exerted by the dune.

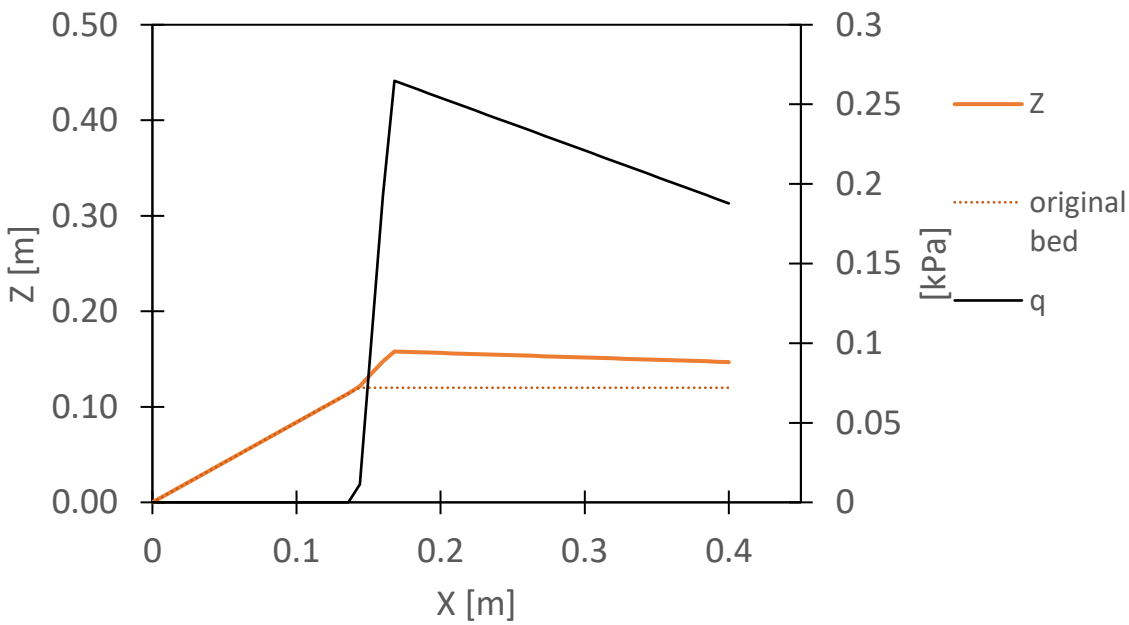

Figure (4- 36): Bed geometry and dune's load distribution.

The triggering point (p1) of the sediment avalanche is decided to be at 3 cm upstream of the active zone (horseshoe vortex zone) based on the observation of the sediment avalanche occur during the experimental run.

50 slices were determined for discretizing the sliding mass, the acting force and the mobilized volume for each slide was computed that corresponding to the critical failure surface which is determined when the safety factor (Fs) equals 1. The total mobilized volume is the summation of all the slices' volumes.

The hydraulic gradient that induces the seepage force was not measured experimentally. Therefore, sensitivity analysis was performed to investigate the effect of hydraulic gradient variation on the mobilized volume.

Figure (4-37) shows the mobilized volume change corresponding to hydraulic gradient from 0.1 to 1 with respect to friction angles of 31.5^o and 40°.

The mobilized volume is an increasing function of the hydraulic gradient. Increasing the seepage force results in triggering bigger volume to move. Less friction angle leads to bigger mobilized volume because of the reduction in the resistance.

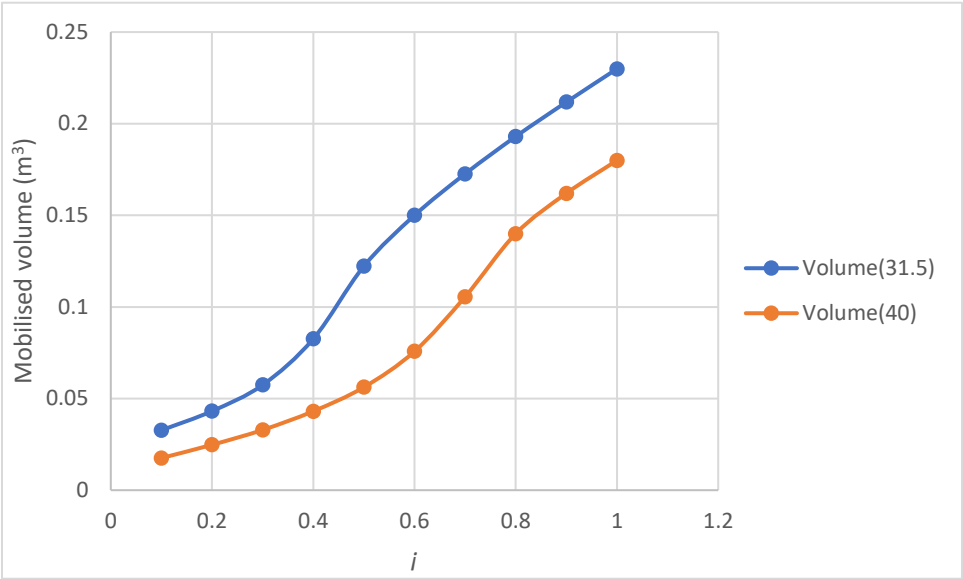

Figure (4- 37): Mobilized volume variation with hydraulic gradient at different friction angle.

The hydraulic gradient within the scour hole was measured during an experimental campaign performed by Bateman and others (2005) which was 0.11 for a smaller sediment size (d_{50} =1.617 mm) than the present one. Therefore, i=0.11 is used in the present analysis as a preliminary estimation.

Two constraints were applied to determine the critical surface of failure: first, based on the observation of the measured slope variation in E3, E4 and E5, the minimum slope inclination present immediately after the sediment avalanche ranges from 28º to 32º, as shown in figure (4-24) which helps to identify the starting point of the avalanche (p2) ; second, the factor of safety has to be (1) to determine the center of rotation(COR) of the sliding mass.

A range of values with x = [0.18:0.21] with increment of 0.1 to find the most realistic initiating point was tested. Four points were tried as shown in figure (4-38). At each point, different COR were tried to find the critical surface that corresponding to F=1; as shown in figure (4-39), different failure surfaces were tried to find the critical one that corresponding to Fs=1, and consequently, the corresponding angle of immediate slope after failure. It was found that the point at (0.21,0.16) has angle of slope after failure (31.7º) as illustrated in the graph of figure (4-40), thereby, this point is considered the most realistic one.

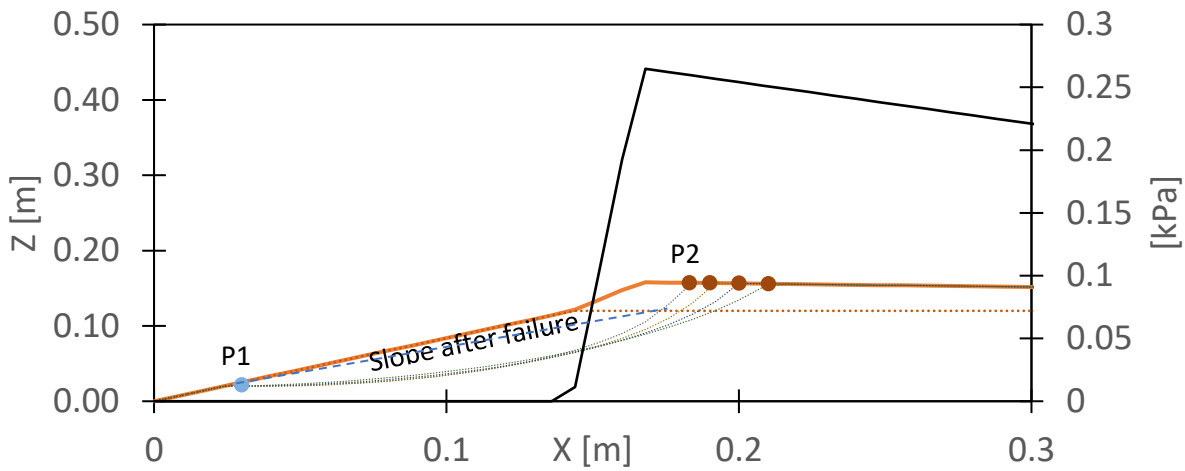

Figure (4- 38): Different tried locations of point (P2).

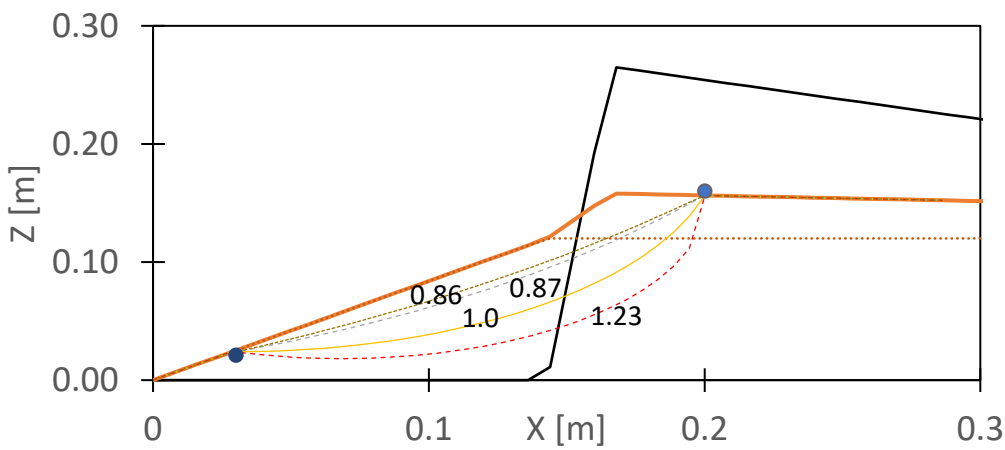

Figure (4- 39): Different tried critical surfaces with their corresponding safety factors.

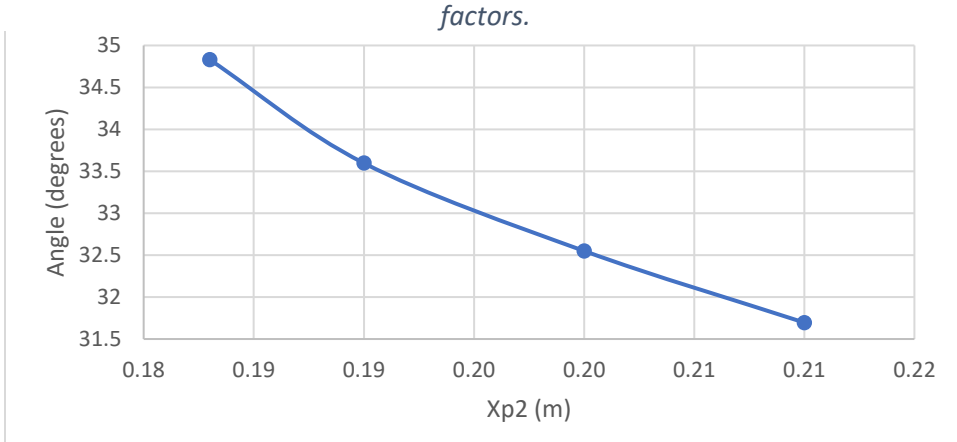

Figure (4- 40): Immediate slope angle after failure variation with p2 locations.

After determining the critical surface, the mobilized volume was calculated. However, the accumulated volume downstream of the triggering point is the difference between mobilized volume and the volume that was exist before the dune arrival as depicted in figure (4-41).

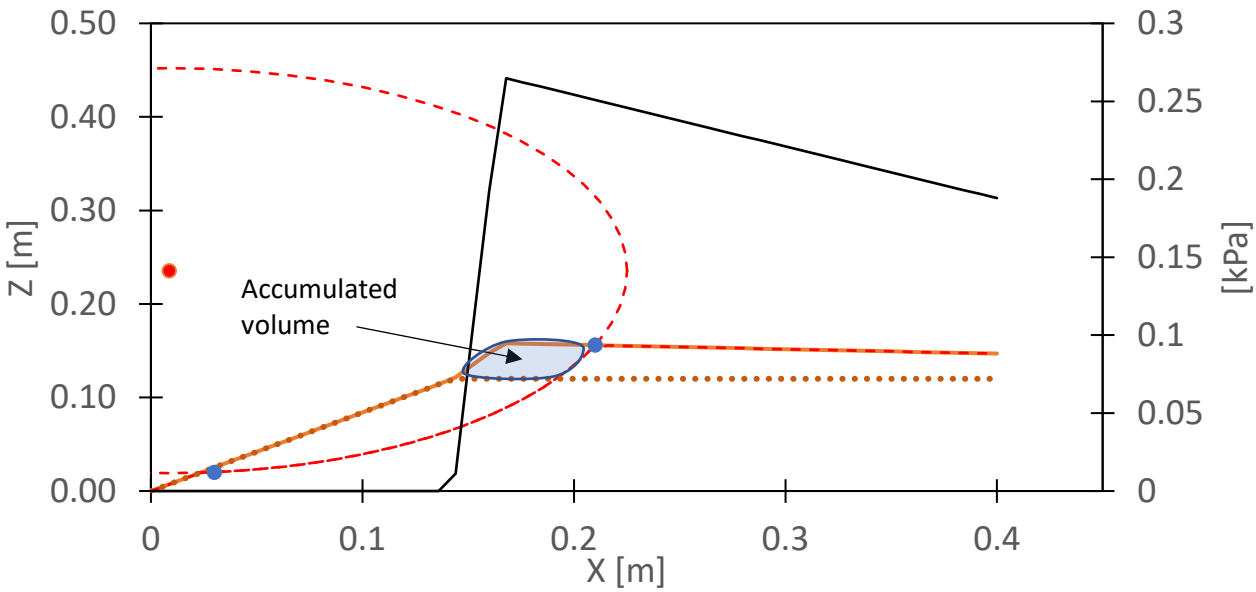

Figure (4- 41): The net accumulated volume downstream of the triggering point.

Therefore, the conceived geotechnical model can provide a preliminary interpretation of the sediment avalanche occurring within the scour hole at the time of failure. The model depicts that the scour hole slope failure occurs because of the external load exerted by the arrival of the dune front at the hole edge, consequently, an immediate failure occur to the inclined slope with a sliding mass moving towards downstream which is in agreement with the values of the amplitudes computed at 7.5 cm upstream of the pier and within the scour hole that has higher amplitude than all the other points, In addition to the behavior of slope temporal sudden decrease after gradual increase. It is deduced that the sudden decrease of slope is recorded when the immediate slope failure occurs and sediment avalanche started to move; thereafter, by considering the continuous sediment transport, the slope is striving to stabilize gradually to reach the maximum value before the arrival of the following dune.

This model is considered as a starting point to explain the real mechanism happening within the scour hole that has been neglected by most of the previous studies. This platform model can be significantly refined by considering more complex methods and more detailed observations of the sediment motion within the scour hole (e.g. the hydraulic gradient).

4.2.3. time scale analysis scour.

The Autocorrelation function was used for the computation of time scale which is computed as follows.

Where x is a time series:

$$A(x,k) = \frac{\overline{x(t)x(t+k)}}{\sigma_x{}^2}$$

Where k is a separation time, σ_x^2 is the variance of x and the over-bar denotes averaging. Note that x series already had zero average since they were computed as fluctuations around a mean elevation.

Time scale analysis for scour hole slope

Figure (4-42) depicts the autocorrelation function of temporal slope variation for E3, E4 and E5.

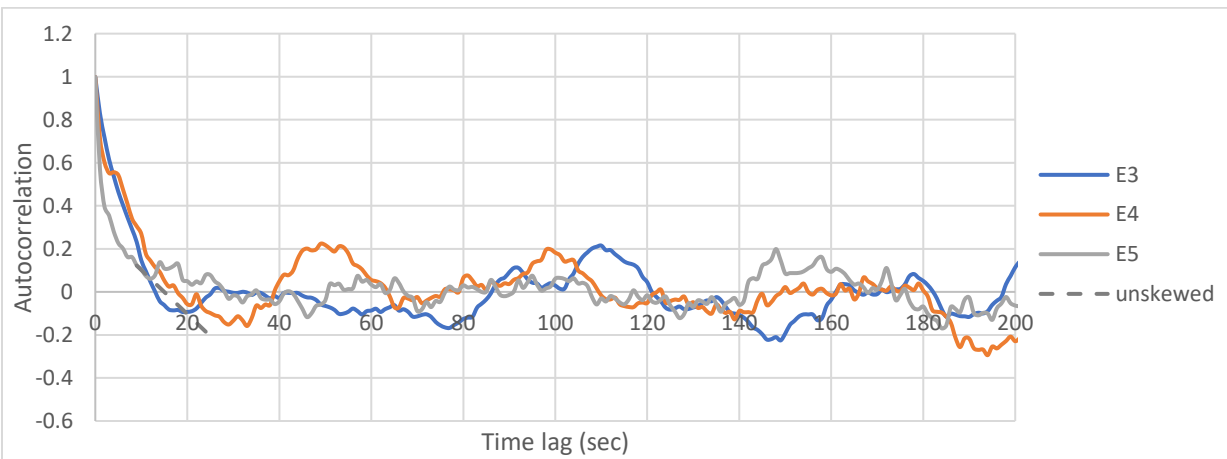

Figure (4- 42): Autocorrelation of slope variation in E3, E4 and E5.

Note: due to the skewness occurs in the autocorrelation of E5 when it approaches the (0), the unskewed part was exponentially interpolated to maintain the consistency of the function at this part.

For all the data series, the integral scale of correlation is not significantly different between the data series as the integral scale λ is (13.79), (17.71) and (14.96) for E3, E4 and E5 respectively. Additionally, it is illustrated that all the data series are weakly sinusoidal, but they are slightly different from each other. Moreover, E4 looks more periodic than the other series and the least having anomalous data as it has the highest λ.

To assure the similarity between the data series acquired by the three experiments E3, E4 and E5, Cumulative Distribution Function (CDF) was used as in figure (4-43).

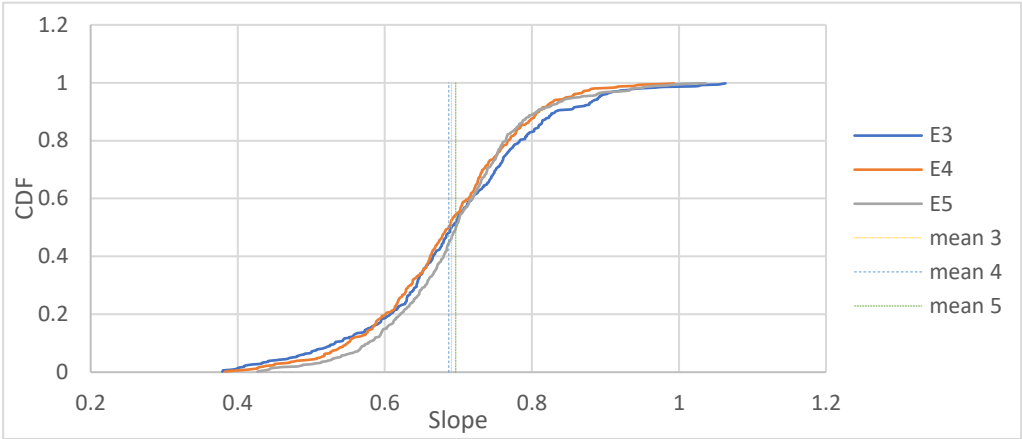

Figure (4- 43): CDF of slope variation series in E3,E4 and E5.

High similarity and overlapping between the three data series noticed; therefore, the trend of slope variation is highly similar in the three directions, the mean and the variant are quite similar.

The comparison of time scale for both discharge values ($1.4Q_c$, $1.6Q_c$) is shown in figure (4-44).

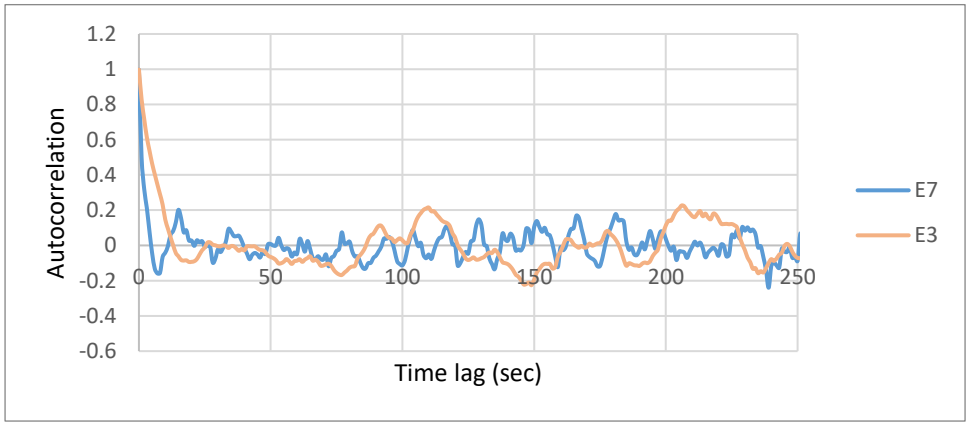

Figure (4- 44): Autocorrelation of scour hole slope variation in E3 and E7.

The comparison between E3 and E7 illustrates that E7 has integral scale (4.65) less than E3 (13.79), therefore, the period of oscillation for E7 is lower than E3 and has less wave length, and more periodic. However, they are weakly correlated. To visualize the different characteristics between E3 and E7 data series, CDF for both data series were done as illustrated in figure (4-45).

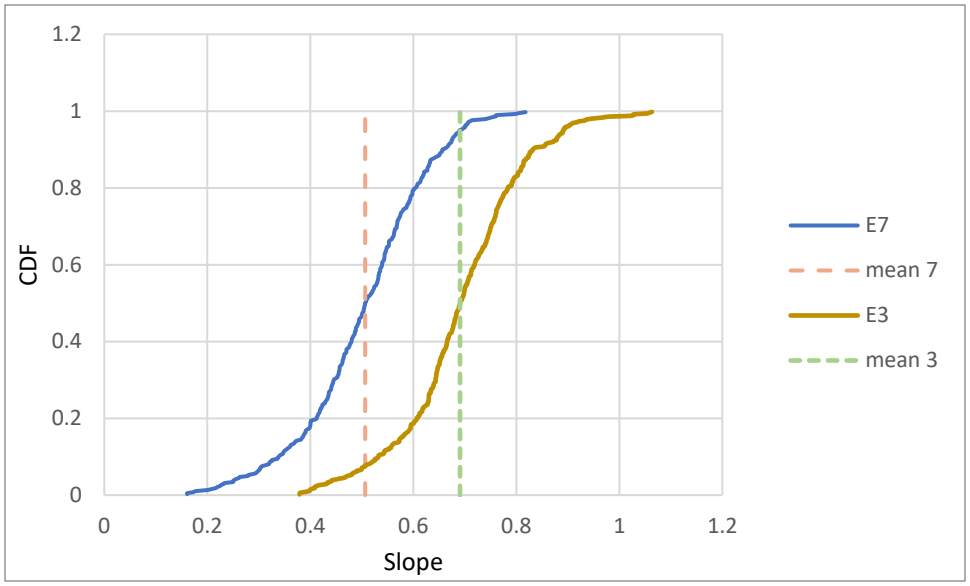

Figure (4- 45): CDF analysis of scour hole slope variation in E3 and E7.

The mean slope of E7 is lower than E3 that can be interpreted by the weakness of horseshoe vortex effect to scour and deepen the hole in comparison with the rate of incoming sediment that controls the scour depth and narrowing the hole; however, the trend of the distribution is not significantly different but E7 has similar range of distribution and dispersion to E3.

The autocorrelation function was applied for the seven experiments of steady flow rate conditions for all the measuring points. In addition, the CDF was used to present the cumulative distribution for each set of data which will emphasize quantitively the differences between the data series based on the characteristics of the distribution. Figure (4-46) illustrates the autocorrelation trends of points 2, 3 and 4 that placed at 2.5, 7.5 and 13.5 cm upstream of the pier nose in E3, and 2.5, 6.5 and 10.5 cm in E7 respectively, in addition to the scour hole slope variation for the flow rate (1.4Q_c) and (1.6 Q_c).

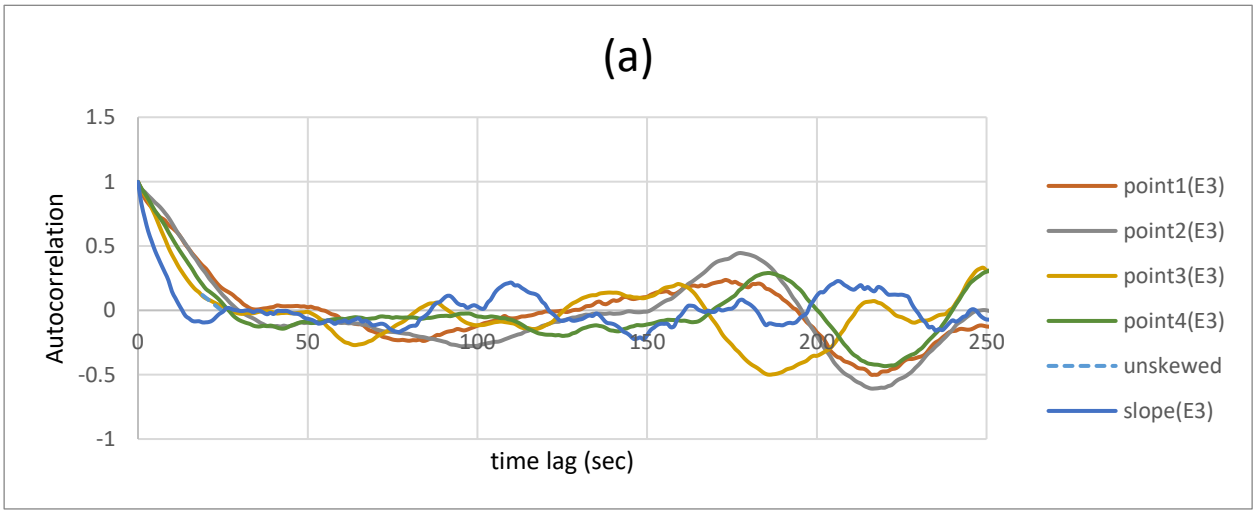

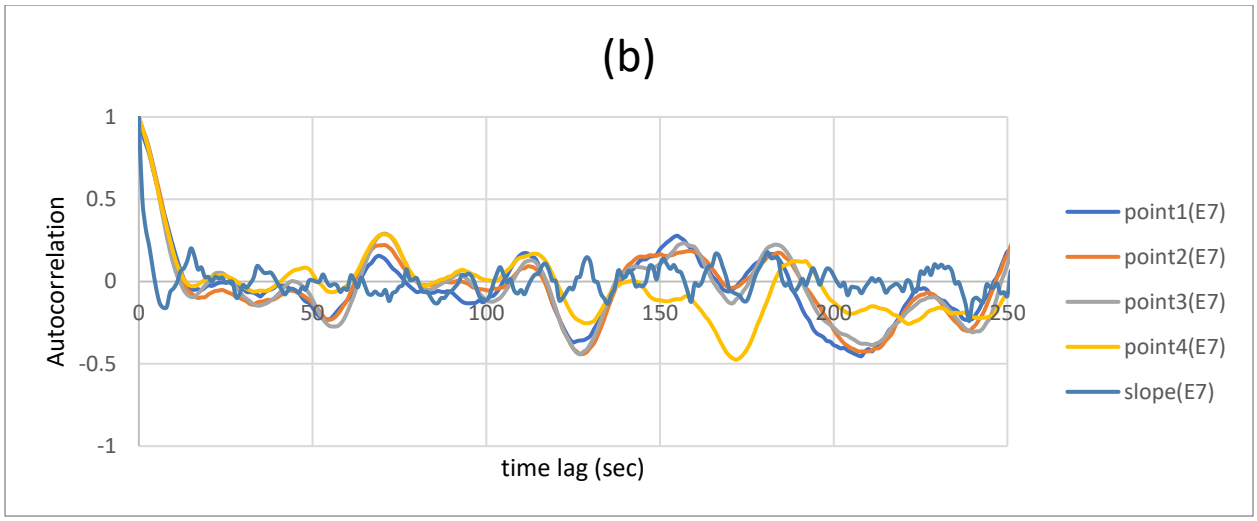

Figure (4- 46): Autocorrelation function comparison between measuring points within the scour hole and hole slope, (a) in case of Q=1.4Qc and E3, (b) in case of Q=1.6Qc and E7.

Better correlation is evident in case of lower discharge, the slope variation and points within the scour hole have close periodicity and sinusoidal level. Instead, for higher flow rate, the points within the hole have significant intercorrelation, and the same periodicity and sinusoidal level are present at all the points, inversely no clear relation between the points and the scour slope variation that seem to be more periodic but less sinusoidal.

Table (4-8) shows the value of λ for each point and for the slope variation computation. For 1.4Q_c, the series wave length is a decreasing function of the distance unlike for 1.6 Q_c that the points have no unique trend of λ over the distance. For both flow rate conditions, at all the points, λ is higher than the one obtained for slope variation; therefore, the wave period of depth fluctuation wave at all the points is higher compared to the one of slope variation that is more periodic as shown in figure (4-33).

	λ
Point #2(E3)	29.71
Point #3(E3)	24.61
Point #4(E3)	17.06
E3	13.79

	λ
Point #2(E7)	12.73
Point #3(E7)	11.97
Point #4(E7)	13.38
E7	4.65

Table (4- 8): Integral scale of correlation of points within the scour hole and slope variation in E3 and E7.

Figure (4-47) shows the comparison between the points located inside the scour hole for both E3 and E7, where points 2 and 3 were placed at 2.5 cm and 7.5 cm for E3 and 2.5 and 6.5 cm upstream of the pier nose for E7. Noting that the skewness correction is done for point#3 of E3

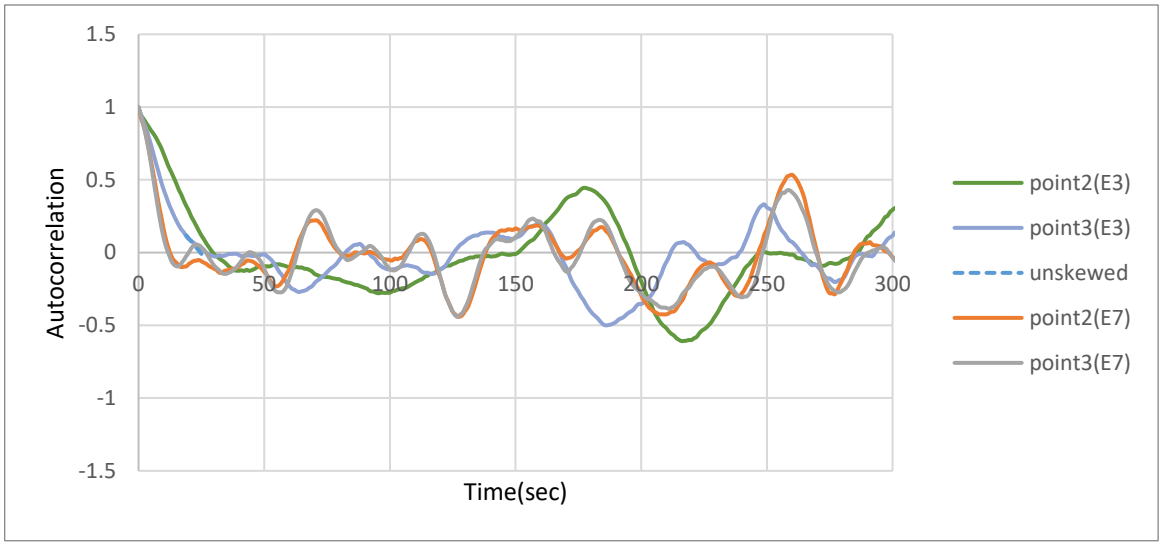

Figure (4- 47): Autocorrelation of water depths at points inside the scour hole in E3 and E7

Table (4-9) shows the values of λ for points 2 and 3 for E3 and E7.

	λ
Point2(1.4)	29.71
Point3(1.4)	24.61
Point2(1.6)	12.73
Point3(1.6)	11.97

Table (4- 9): Integral scale of correlation of points inside the scour hole in E3 and E7

For Q=1.6 Q_c, the points located inside the scour hole has similar λ as shown in the previous results which is generally lower than those which corresponding to discharge Q=1,4 Q_c. Moreover, the data series of higher discharge seem to be more periodic and sinusoidal. It is evident that the wave length in case of higher flowrate is less due to the rapid periodic oscillation.

For E3 and E7, The cumulative distribution of the data recorded inside the scour hole have significantly similar distribution pattern with close mean and dispersion range for the point placed at 2.5 cm, but at the further point that closer to the hole edge at 7.5 cm for E3 and 6.5 cm for E7 have significant difference in the mean value and dispersion range as shown in figure (4-48) and table (4-10).

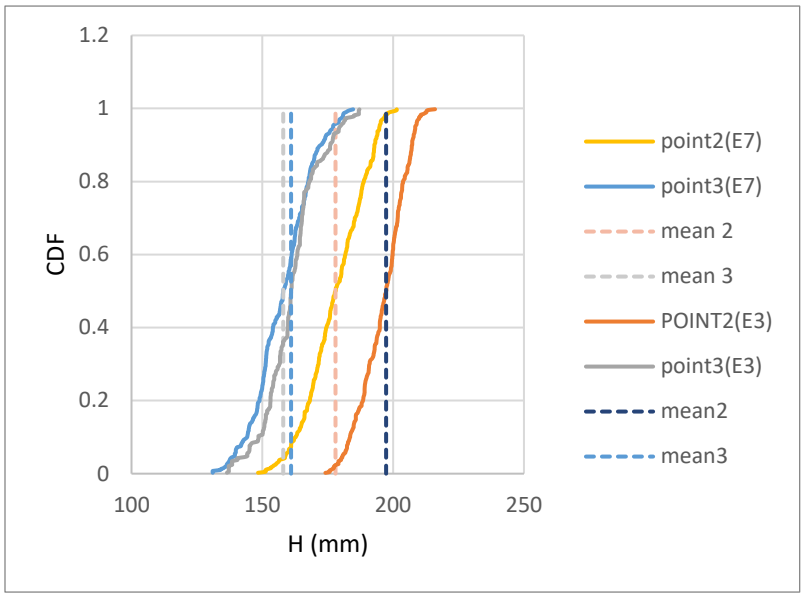

Figure (4- 48): CDF of depths measured at points inside the scour hole during E3 and E7.

	Mean (mm)	Dispersion Range (mm)
point2(E3)	197.32	41.91
point3(E3)	160.98	50.65
point2(E7)	177.97	53.01
point3(E7)	157.99	53.67

Table (4- 10): Mean depth and dispersion range of depths at measuring points inside the scour hole during E3 and E7.

In both conditions, point 3 has lower mean value than point2 as it is more far from the pier. However, the range of dispersion was more similar between the two points in the case of $Q=1.6Q_c$, which proves a homogeneous pattern of oscillation between both points as presented previously in the autocorrelation function and the amplitude computations.

4.3 Dunes characteristics.

The bed-forms were measured through the fixed points upstream of the scour hole. The measurements were acquired for both discharge values ($1.4Q_c$ and $1.6\ Q_c$) by placing three points upstream of the scour hole at 25 cm, 48 cm and 116 cm as previously mentioned in the description of E1 and E6.

4.3.1 time scale analysis of dunes.

The data concerning the bed-forms were detected in experiments E1 and E6 through the placed measuring points upstream of the scour hole.

Figure (4-49) presents the autocorrelation function for points 2, 3 and 4 for both conditions of discharge values, where points 2, 3 and 4 where placed at 25, 48 and 116 cm upstream of the pier nose respectively.

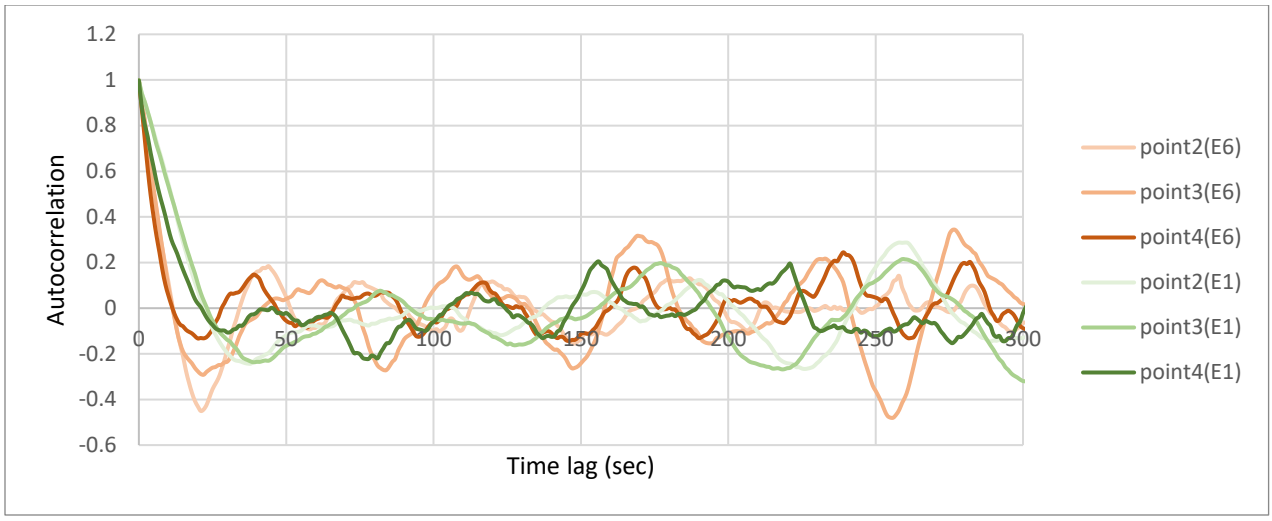

Figure (4- 49): Autocorrelation function of depths at points upstream the scour hole during E1 and E6.

Table (4-11) presents the values of λ at different points for both discharge ratios.

	λ
Point2(E1)	22.16
Point3(E1)	23.12
Point4(E1)	21.09
Point2(E6)	11.58
Point3(E6)	11.42
Point4(E6)	11.50

Table (4- 11): Integral scale of correlation of the points upstream the scour hole during E1 and E6.

The results of the autocorrelation function show less λ in case of higher discharge which is because of faster dunes motion. In addition, a marginal difference is observed in the values of λ and periodicity for the same discharge at different points, and high correlation is present. In general, the data series of higher discharge are more periodic and sinusoidal compared to the lower discharge due to the higher and better formation of the dunes through the channel.

Figure (4-50) represents the CDF analysis was carried out for the three points outside the scour hole for both discharges to find the difference in the distribution between them.

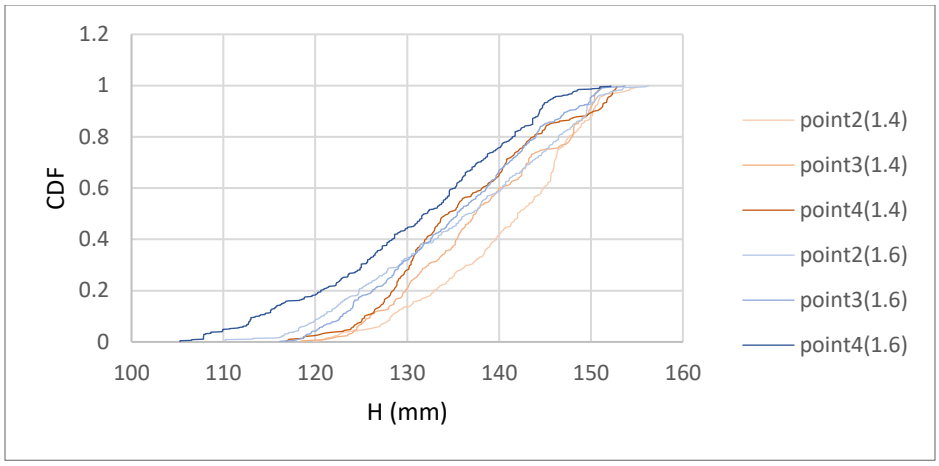

Figure (4- 50): CDF of measuring points upstream the scour hole in E1 and E6.

Table (4-12) shows the mean values and dispersion ranges of data extent at the above-mentioned points.

	Mean (mm)	Dispersion range (mm)
Point2(1.4)	142.03	35.18
Point3(1.4)	137.46	32.91
Point4(1.4)	134.45	35.91
Point2(1.6)	136.65	46.03
Point3(1.6)	135.45	37.59
Point4(1.6)	131.93	46.87

Table (4- 12): Mean depth and dispersion range of depths at measuring points outside the scour hole in E1 and E6.

The values of mean depths are slightly different between the points; however, the mean values of lower discharge are generally higher as the water depth is higher due to less sediment transport on the bed that creates smaller dunes. Unlike the range of distribution which has higher values at $1.6Q_c$ than at $1.4Q_c$, that interpreted by the existence of extensive fluctuation in case of higher discharge.

The measured data of the depth on the inclined surface of the scour hole was compared with the depth measured upstream of the scour hole based on the autocorrelation function as shown in figure (4-51) for discharge of 1.4 Q_c, where points A and B are placed 7.5 cm and 48 cm upstream of the pier.

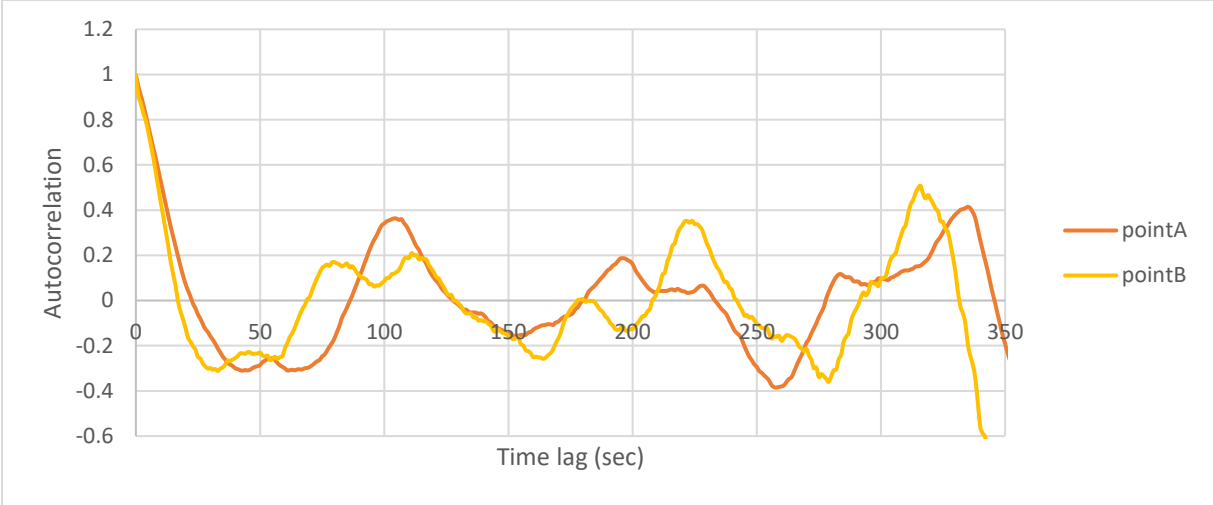

Figure (4- 51): Autocorrelation of a measuring point inside and outside the scour hole for Q=1.4Qc

Point A that located inside the scour hole has slightly higher λ (22.62) compared to point B (17.06), this difference in time scales can be interpreted by change of dune shape inside the scour hole due to the mechanism of sediment avalanche, as they tend to be flatter and spends more time to wash out from the inclined surface. In addition, both series have the same sinusoidal level.

Similarly, for higher discharge (1.6 Q_c), figure (4-52) shows the difference between two points A and B placed at distances 6.5 and 48 cm respectively.

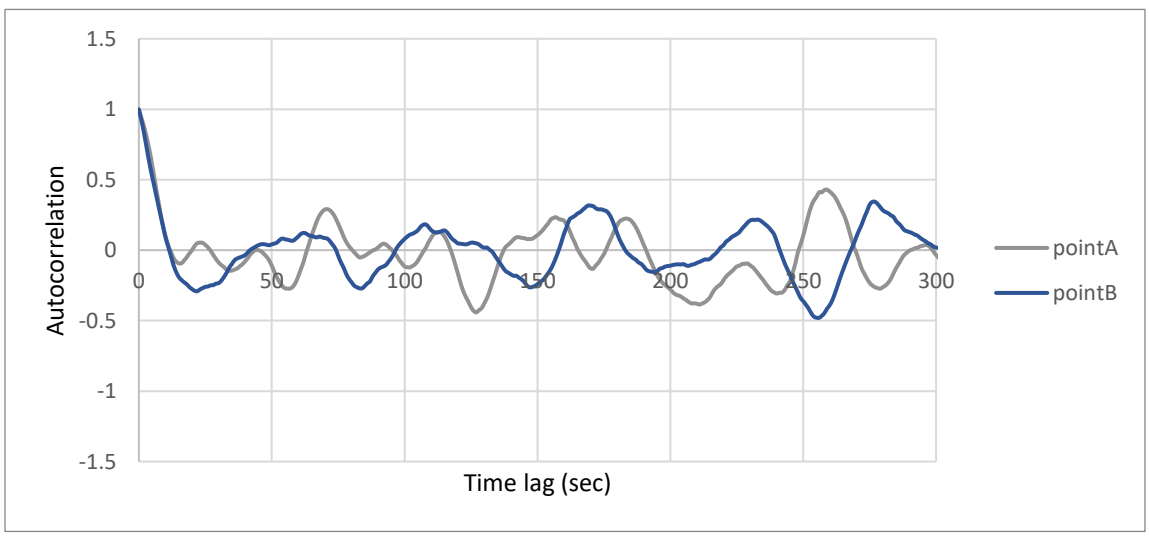

Figure (4- 52): Autocorrelation of a measuring point inside and outside the scour hole for Q=1.6Qc

Unlike 1.4Q_c, the integral scales λ are almost identical for both points, as it is (11.97) at point A and (11.42) at point B, which proves the previous observation of no tangible change in the dunes falling inside the hole due its big size compared to the scour hole as well as the high celerity.

CDF was used to find the difference in distribution characteristics between the dunes and the points inside the hole for both discharge values. Figure (4-53) and table (4-13) show the distributions and the values of mean and dispersion range of the data for both discharge values, as points A and be placed 7.5 cm and 48 cm upstream of the pier nose.

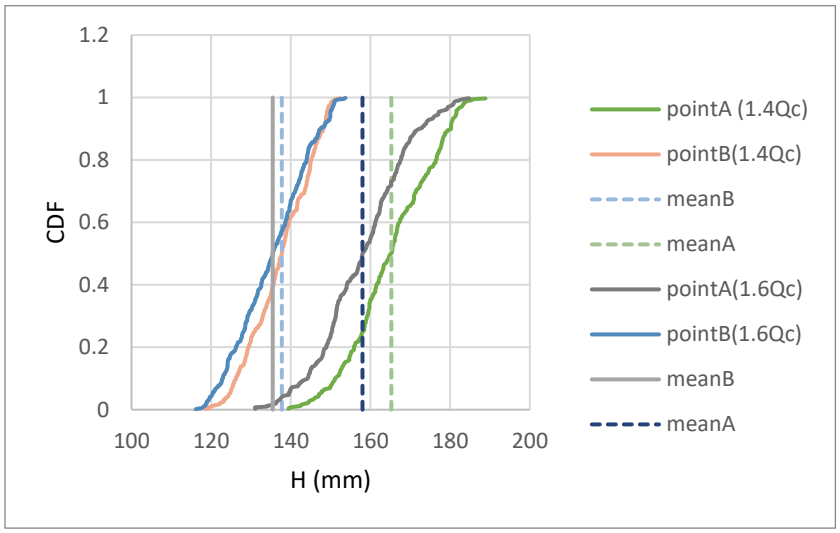

Figure (4- 53): CDF of a point inside and outside the scour hole for discharge of 1.4Qc and 1.6Qc.

	mean (mm)	dispersion range(mm)
pointA(1.4Qc)	165.23	49.45
pointB(1.4Qc)	137.74	33.96
pointA(1.6Qc)	157.99	53.67
pointB(1.6Qc)	135.45	37.59

Table (4- 13): Mean depth and dispersion range of depths at a measuring points inside and outside the scour hole for 1.4Qc and 1.6Qc.

As illustrated in the results, always, the points inside the scour hole has wider range of distribution than the outside dunes which was indicated in the calculations of the amplitude. However, this range is undermined at the points outside the scour hole and far upstream. Moreover, this difference between point A at both discharge in addition to the similarity at distant place from the hole promotes the previously stated behavior of dunes in case of higher discharge that follow a gradual evolution pattern as long as they approach the scour hole.

To understand the change between the migrating dune from upstream and the scour fluctuation at the pier, the data series acquired at the point placed at 0.5 from the pier nose and on the edge of the scour hole was compared to the points located inside the scour hole and upstream of the hole. Figure (4-54) illustrates the autocorrelation function of the data series measured at points 1, 2, 3 and 4 that are placed at 0.5 cm, 7.5 cm, 13.5 cm and 48 cm upstream of the pier nose for Q=1,4 Q_c.

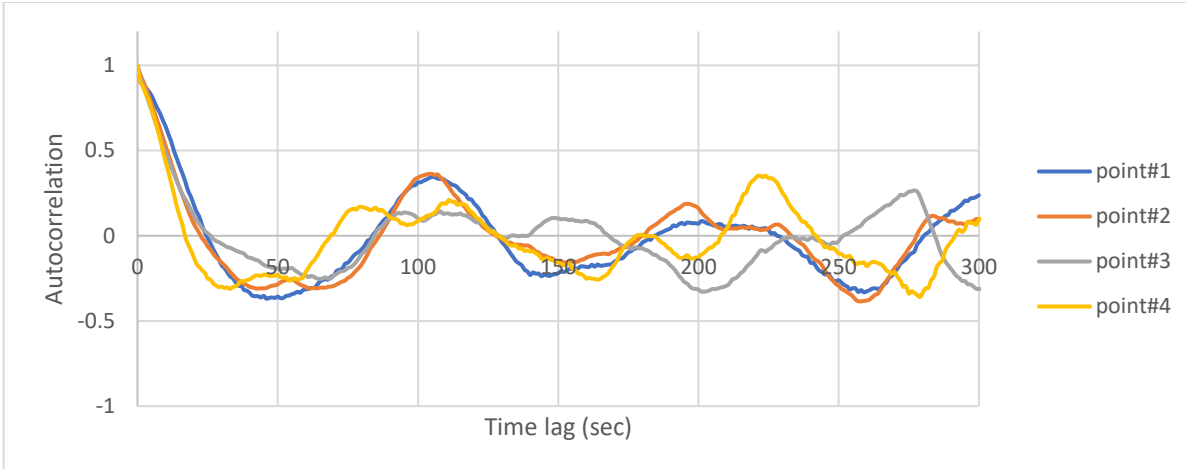

Figure (4- 54): Autocorrelation of depths at points inside and outside the scour hole at Q=1.4Qc.

The points located inside the scour hole have very similar values of λ, are highly correlated and have the same sinusoidal level and periodicity, while point#4 that is far upstream of the hole has less λ as shown in table (4-14). Therefore, the lowest point inside the hole has the same time scale characteristics as all the points within the hole which proves the claim of the dune shape change happens just after entering the scour hole in which a bigger wave length was evident in the points within the hole than the ones outside.

	λ
point#1	24.68
point#2	22.62
point#3	25.96
point#4	17.06

Table (4- 14): Integral scale of correlation for points inside and outside the scour hole at Q=1.4Qc.

Similarly, for 1.6Q_c, figure (4-55) shows the autocorrelation function for points 1, 2, 3 and 4 placed at 0.5 cm, 6 cm, 10 cm and 48 cm upstream of the pier.

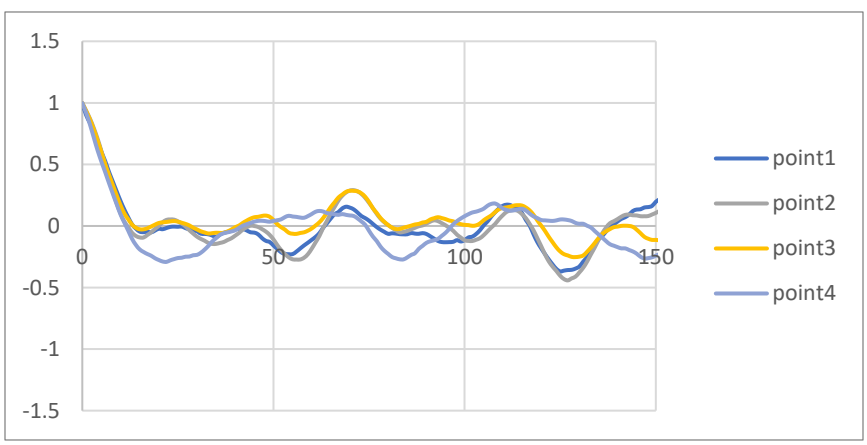

Figure (4- 55): Autocorrelation of points inside and outside the scour hole at Q=1.6Qc.

	λ
point1	13.39
point2	11.97
point3	13.38
point4	11.42

Table (4- 15): Integral scale of correlation for points inside and outside the scour hole at Q=1.6Qc.

The integral scale of correlation λ, as shown in table (4-15), has no significant difference between all the points. However, the points inside the scour hole are more periodic and sinusoidal than the points outside.

4.3.2 Dunes' celerity.

One of the main characteristics of the bed-forms is the celerity, three methods of computation used in our experiment to assess the dune celerity that are user-determined overlap by matching the dunes' peaks and lags, using cross correlation function and using sediment mass balance.

the cross-correlation is the measure of similarity of two series as function of the lag one relative to the other which defined as following.

$$C(x,y,L) = \frac{\overline{x(t)y(t+L)}}{\sigma_x \sigma_y}$$

Where $x(t)$ and $y(t)$ are function of time. L is the time lag. It can be negative, zero or positive, σx is the variance of x, σy is the variance of y and the over-bar denotes averaging.

Another assessment of the celerity was based on the value of amplitude Δ_D which used to give a first-order evaluation of dune celerity *c* based on sediment mass balance. The latter condition requires that the volume of one dune W_D passes through a transverse section during a dune period T_D. Therefore, λ_D is dune wavelength, *B* is channel width, *P* is porosity and Q_s is the sediment discharge.

$$W_D = 0.5\, \Delta_D \lambda_D B \;, \quad Q_s B T_D = W_D (1-P) \Longrightarrow c = \frac{\lambda_D}{T_D} = \frac{2Q_s}{\Delta_D(1-P)}$$

The celerity of the dunes was calculated only for case of distant placement of the measuring points, therefore, the celerity computations were performed only in E1 and E6.

Figure (4-56) depicts the installation of experiment E1 and the places of the lasers upstream of the pier.

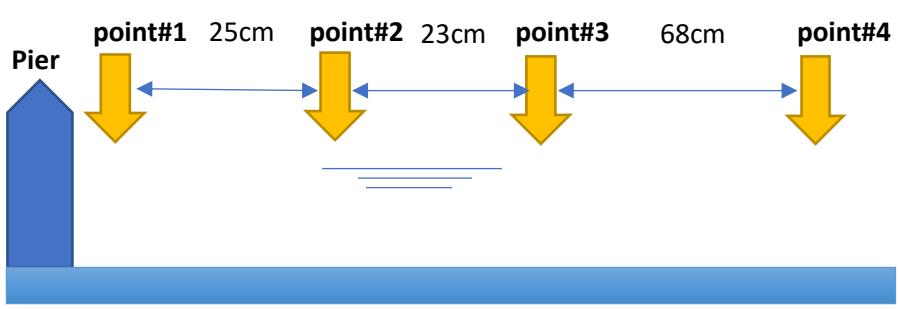

Figure (4- 56): Experiment E1 setup.

The celerity was calculated for this experiment using the three methods that mentioned previously. The celerity from point#4 to point #3, from point#3 to point#2 and from point#4 to point#2. Using user-determined overlap method to match the dunes and getting the time lag L, then calculating the celerity $c = {}^{d}/_{L}$ where d is the distance between the two measuring points.

Figure (4-57) shows the original places of the migrating dunes upstream of the pier from point#3 to point#2.

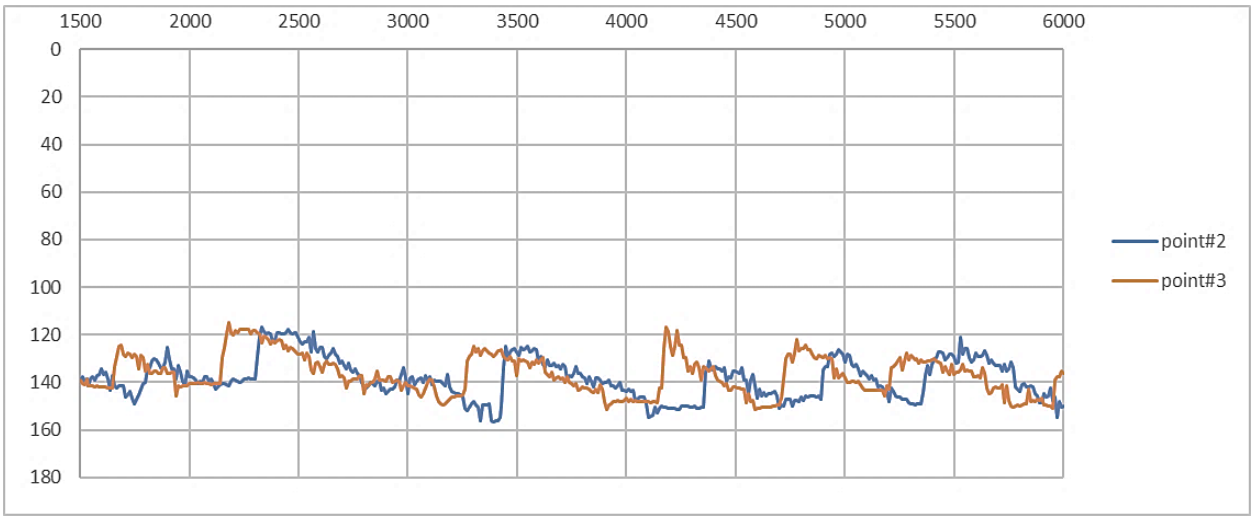

Figure (4- 57): Dunes originally exist at points 2 and 3 for Q=1.4Qc.

After applying a time lag of 180 seconds which is the temporal difference between the two series, as shown in figure (4-58), the dunes are highly matching to together.

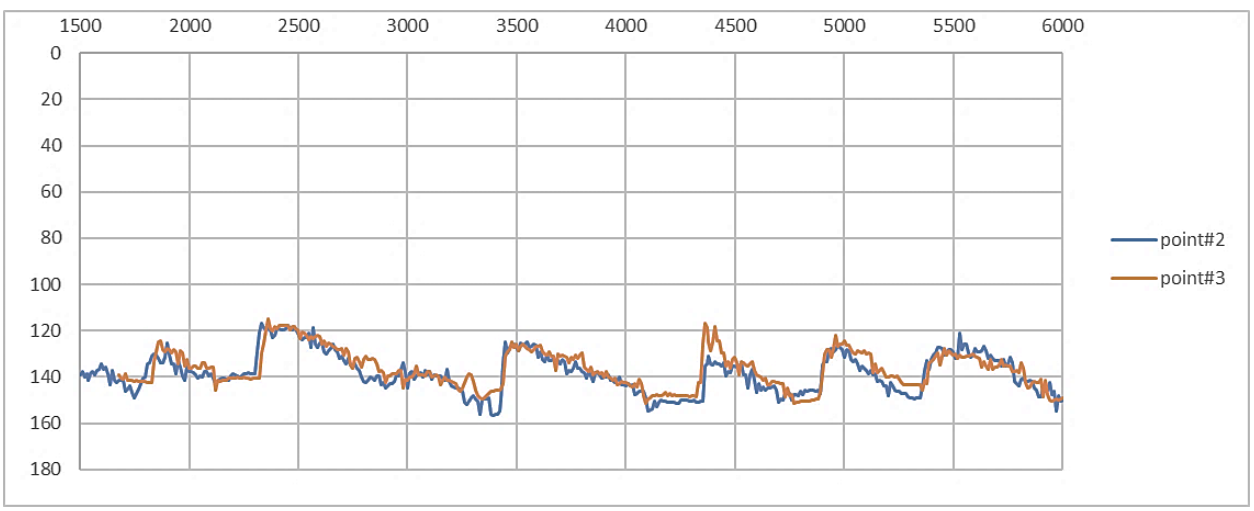

Figure (4- 58): Matched dunes between points 2 and 3.

Thereby, the results of the calculate celerity in this case are as in table (4-16), where d is the distance between the two points, L is the time lag applied to match both series and C is the calculated celerity.

d=	23	cm
L=	180	sec
C=	0.127778	cm/sec

Table (4- 16): Matching results.

The same approach was followed for the other two reaches that are between points 4 and 3, and points 4 and 2. Table (4-17) illustrates the results obtained by this method for three possible reaches.

Reach	distance(cm)	time lag (sec)	celerity (cm/sec)
4 to 3	68	530	0.1283
3 to 2	23	180	0.1278
4 to 2	91	710	0.1282

Table (4- 17): Matching results for all reaches for Q=1.4Qc.

The results show that for all the reaches, the values of celerity are in the same range ang highly similar with minor difference between them.

Another way to determine the celerity is using the cross-correlation function between the two series in this case. Figure (4-59) shows the cross-correlation curve and the point at the time step of best matching between both series.

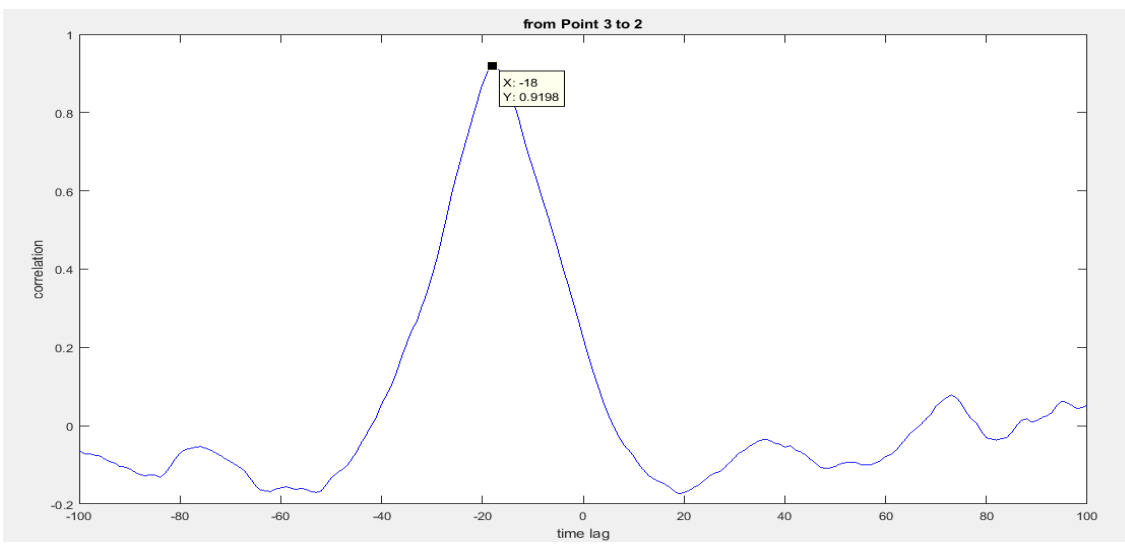

Figure (4- 59): Cross correlation function between points 2 ad 3 for Q=1.4Qc.

The graph illustrates that the highest correlation (0.919) happened after 18 time steps, in which every time step is 10 seconds, consequently, the time lag between both series is 210 seconds, and consequently the celerity is 0.1287 cm/sec.

By the same way, the celerity in other reaches was calculate by using this method of cross-correlation function. Table (4-18) shows the results for each reach and the correlation value at each of them.

Reach	distance(cm)	highest Correlation	time lag (sec)	celerity (cm/sec)
4 to 3	68	0.83	529	0.1286
3 to 2	23	0.919	180	0.1278
4 to 2	91	0.811	709	0.1283

Table (4- 18): Cross correlation function for all the reaches.

As shown in the previous results that obtained by the methods of user-determined overlap and cross-correlation function, the values of the celerity in all reaches are highly similar.

Additionally, the sediment mass balance was used based on the calculated amplitude with all the applied probability ranges at the measuring points 2, 3 and 4. Table (4-19) show the calculated celerity at each point based on the amplitudes calculated beforehand knowing that the value of the equilibrium sediment discharge for $Q=1.4Q_c$ is 6.18E-06 and the porosity is 41%.

(a)measuring amplitude for point#2 25 cm Upstream				
Prop %	p1	p2	ampl(mm)	c (mm/s)
80	0.1	0.9	19.642	1.066549
90	0.05	0.95	22.637	0.925439
95	0.025	0.975	26.02	0.805117
98	0.01	0.99	28.348	0.738999

(b)measuring amplitude for point#3 48 cm Upstream				
Prop%	p1	p2	ampl(mm)	c (mm/s)
80	0.1	0.9	21.746	0.963357
90	0.05	0.95	25.137	0.833399
95	0.025	0.975	26.44	0.792328
98	0.01	0.99	29.11	0.719655

(c)measuring amplitude for Point#4 116 cm Upstream				
Prop%	p1	p2	ampl(mm)	c (mm/s)
80	0.1	0.9	25.461	0.823
90	0.05	0.95	28.14	0.744
95	0.025	0.975	32.705	0.641
98	0.01	0.99	35.602	0.588

Table (4- 19): Celerity values result from sediment mass balance for Q=1.4Qc.

The results show that for all probability ranges the estimation of celerity is lower than those values obtained using cross-correlation function and user-determined overlap method of the dunes. However, for the least probability range (80%), the celerity values are the highest at all the points, and also the closest to the values computed by the other two methods.

Table (4-20) shows the results of celerity obtained by each method separately, averaging the celerity values at the points bounding each reach, was applied to the method of sediment mass balance to calculate the celerity for the three reaches as shown in the table with respect to all the probability ranges. Reach #1 was decided to be from point 4 to point 3, as reach #2 is from point#3 to point#2 and reach#3 is the biggest one which extends from point#4 to point#2 as written in the table. Additionally, all the celerity values are expressed in cm/second.

Reach		**distance(cm)**	**celerity (cm/sec)**					
			User-determined overlap	cross-correlation	sediment mass balance			
					prob 80%	prob 90%	prob 95%	prob 98%
1	from4 to 3	68	0.1283	0.1286	0.0893	0.0789	0.0716	0.0654
2	from3 to 2	23	0.1278	0.1278	0.1015	0.0879	0.0799	0.0729
3	from4 to 2	91	0.1282	0.1283	0.0945	0.0835	0.0723	0.0664

Table (4- 20): Celerity values obtained by all the methods of computation for Q=1.4Qc.

Figure (4-60) shows a graphical representation of the results included in the previous table.

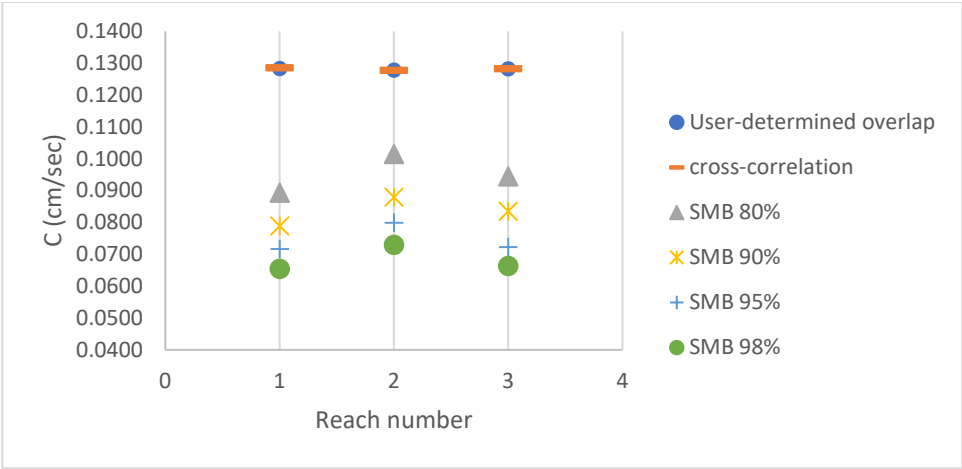

Figure (4- 60): Celerity values obtained by all the methods of computation for all the reaches.

The figure shows that the methods of user-determined overlap and cross-correlation are almost identical in the evaluation of the celerity. However, by applying the method of sediment mass balance, the estimated celerity is much lower in comparison with the other methods. Moreover, the less probability range of amplitude used in calculation, the higher value of celerity obtained. Therefore, the value corresponding to probability range 80% is the closest to the methods of cross-correlation and user-determined overlap; however, by using probability range of 98%, the least value is obtained and the furthest from the celerity obtained by the two other methods.

Figure (4-61) shows the installation of experiment E6 and the places of the lasers upstream of the pier.

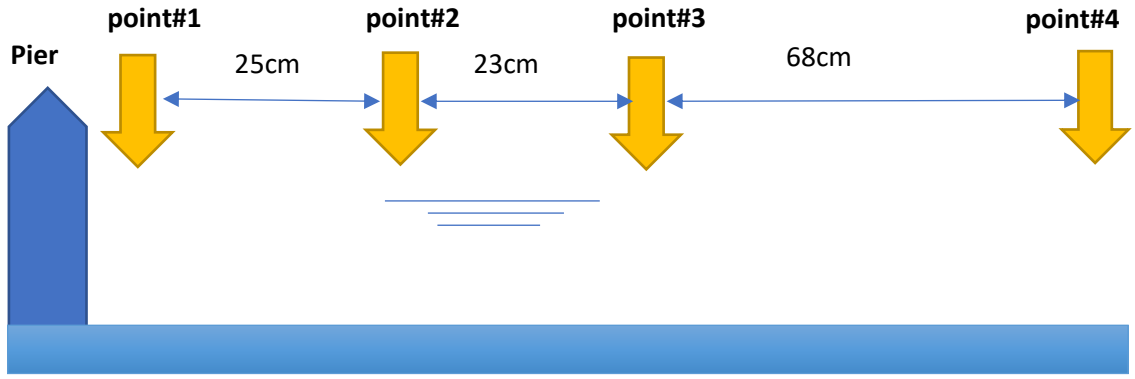

Figure (4- 61): Experiment E6 setup.

The same placement of measuring points as E1 was introduced to this experiment as mention before. The celerity was calculated for this experiment using the three methods that were mentioned previously. The celerity from point#4 to point #3, from point#3 to point#2 and from point#4 to point#2.

In case of considering the smallest reach between point#3 and point#2 which is 23 cm, the user-determined overlap method was used to match the dunes. Figure (4-62) shows the original places of the migrating dunes upstream of the pier from point#3 to point#2.

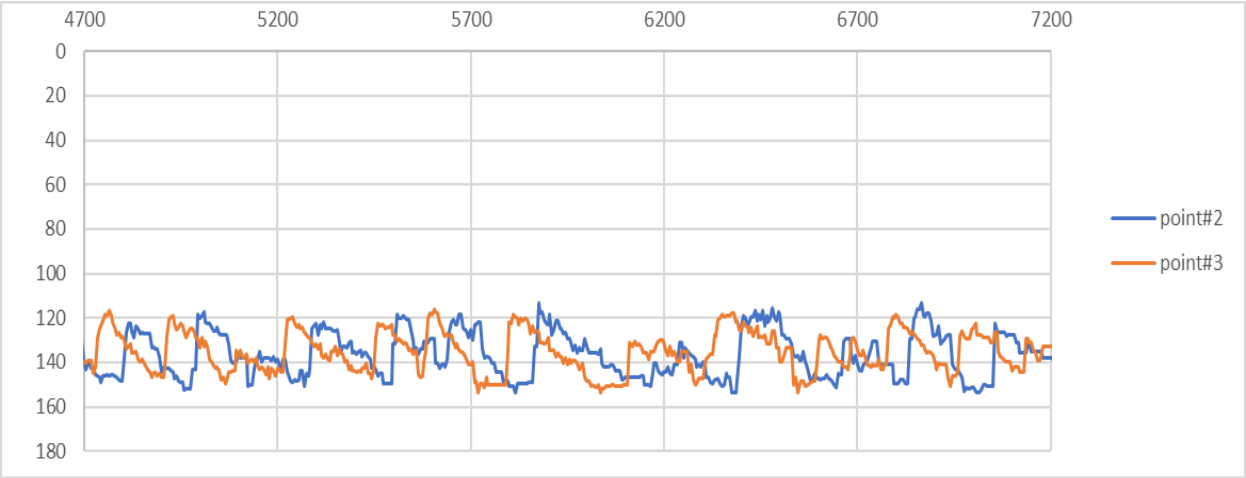

Figure (4- 62): Dunes originally exist at points 2 and 3 for Q=1.6Qc.

By applying a time lag of 145 seconds added to point#3 data series, figure (4-63) illustrates the match between the dunes.

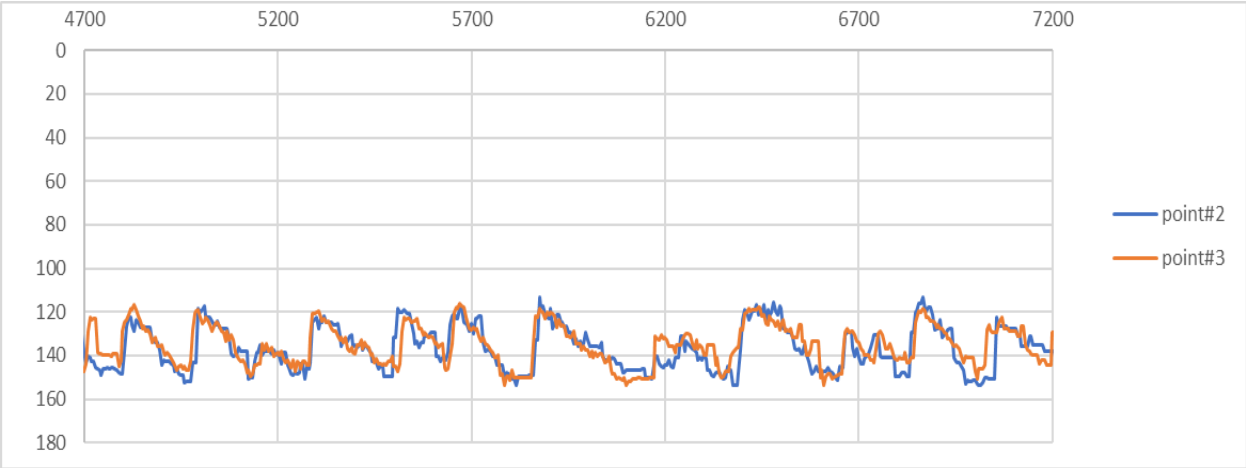

Figure (4- 63): Matched dunes between points 2 and 3.

The same approach was followed for the other two reaches that are between points 4 and 3, and points 4 and 2. Table (4-21) illustrates the results obtained by this method for three possible reaches.

Reach	distance(cm)	time lag (sec)	celerity (cm/sec)
4 to 3	68	145	0.4690
3 to 2	23	65	0.3538
4 to 2	91	210	0.4333

Table (4- 21): Matching results for all reaches for Q=1.6Qc.

The results show a weak correlation between the celerity in the reach between points 4 and 3, and between points 3 and 2. In other words, the reach between point 4 and 3 is where the creation of dunes happens; therefore, the dunes are not fully evolved in the first part of this reach. However, the reach between point 3 and 2 has completely evolved dunes migrating towards the scour hole.

By using the cross-correlation function, figure (4-64) shows the number of time steps different between both series to be matched knowing that each time step is 5 seconds.

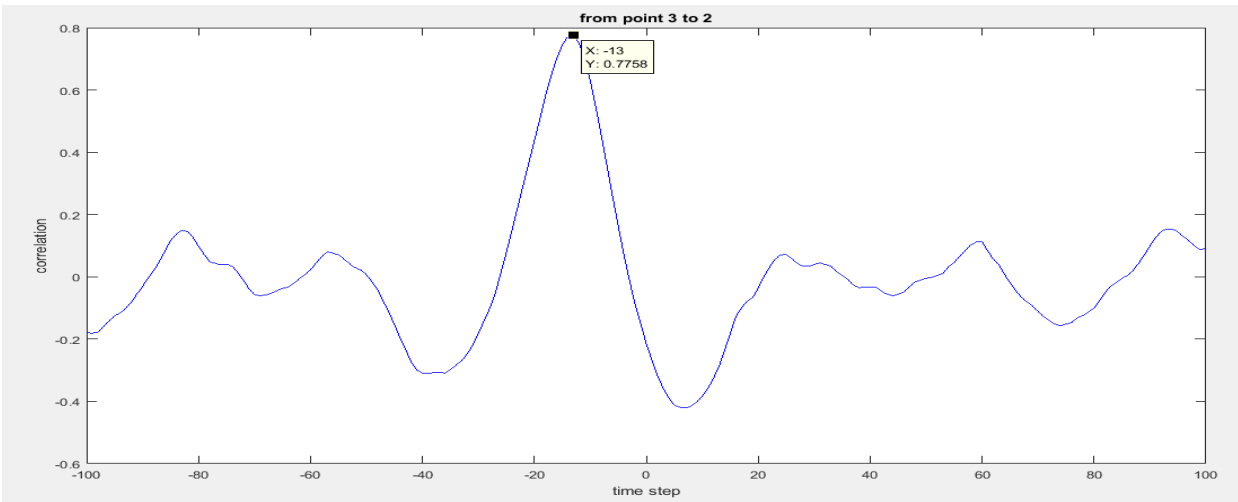

Figure (4- 64): Cross correlation function between points 2 ad 3 for Q=1.6Qc.

It is shown that the highest correlation is 0.77 where the difference between the two series is 13 time steps and each time step is 5 seconds; therefore, the time lag is (65) seconds and celerity is 0.3538 cm/sec.

By the same way, the celerity in other three reaches was calculate by using this method of cross-correlation function. Table (4-22) shows the results for each reach and the correlation value at each of them.

Reach	distance(cm)	highest Correlation	time lag (sec)	celerity (cm/sec)
4 to 3	68	0.473	145	0.4690
3 to 2	23	0.7758	65	0.3538
4 to 2	91	0.4928	210	0.4333

Table (4- 22): Cross correlation function for all the reaches.

The results corresponding to the application the cross-correlation function on different reaches show that the highest correlation is presented in the reach between points 3 and 2 which is 77.58% while the other reaches have lower correlation and less than 50%. Therefore, reach 3 to 2 represents the best evaluation of the celerity value for this experiment.

The sediment mass balance method was used based on the calculated amplitude with all the applied probability ranges at the measuring points 2, 3 and 4. Table (4-23) shows

the calculated celerity at each point based on the amplitudes calculated beforehand knowing that the value of the equilibrium sediment discharge for $Q=1.6Q_c$ is 2.61E-05 and the porosity is 41%.

(a) measuring amplitude for point#2 23 cm Upstream				
Prop%	p1	p2	ampl(mm)	c (mm/s)
80	0.1	0.9	27.748	3.182
90	0.05	0.95	31.204	2.830
95	0.025	0.975	33.593	2.628
98	0.01	0.99	36.951	2.390

(b) measuring amplitude for point#3 48 cm Upstream				
Prop%	p1	p2	ampl(mm)	c (mm/s)
80	0.1	0.9	24.092	3.665
90	0.05	0.95	29.613	2.982
95	0.025	0.975	31.734	2.782
98	0.01	0.99	33.083	2.669

(c) measuring amplitude for point#4 116 cm upstream				
Prop%	p1	p2	ampl(mm)	c (mm/s)
80	0.1	0.9	18.897	4.673
90	0.05	0.95	21.815	4.048
95	0.025	0.975	24.668	3.580
98	0.01	0.99	26.56	3.325

Table (4- 23): Celerity values result from sediment mass balance for Q=1.4Qc.

Unlike E1, the celerity computed using the amplitude values at each measuring point is close to those calculated by user-determined overlap and cross-correlation with marginal difference. However, the highest value obtained from the probability range of 80%, while all the other probability ranges have less celerity values at all the measuring points.

Table (4-21) shows the results of celerity obtained by each method separately following the same methodology in E1.

Reach		distance(cm)	celerity (cm/sec)					
			User-determined overlap	cross-correlation	sediment mass balance			
					probability 80%	probability 90%	probability 95%	probability 98%
1	from4 to 3	68	0.469	0.469	0.417	0.352	0.318	0.3
2	from3 to 2	23	0.354	0.354	0.342	0.291	0.271	0.253
3	from4 to 2	91	0.433	0.433	0.393	0.344	0.310	0.286

Table (4- 24): Celerity values obtained by all the methods of computation for Q=1.6Qc.

Figure (4-65) shows a graphical representation of the results included in the previous table.

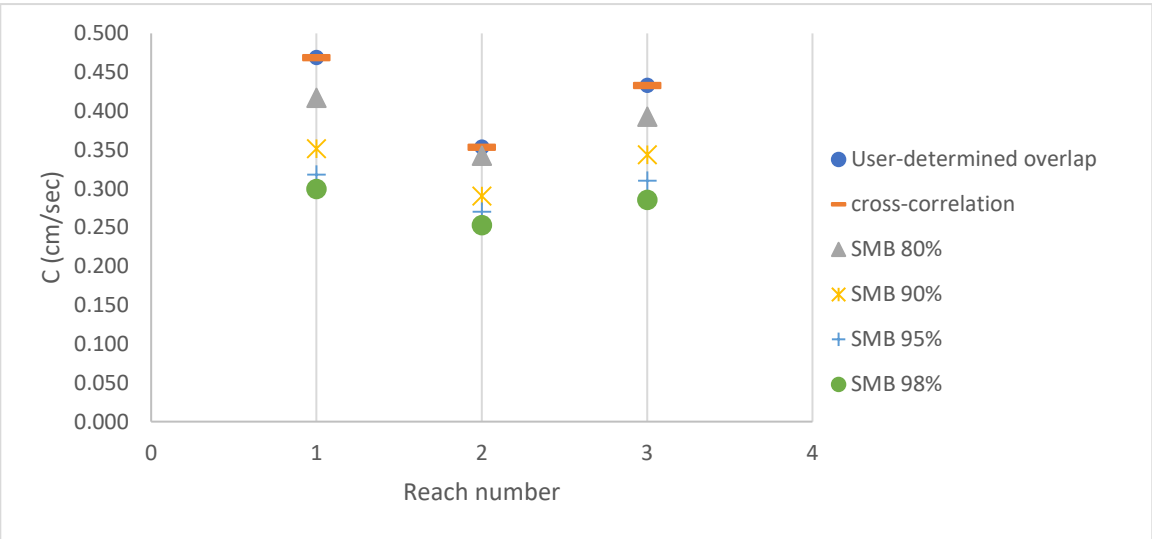

Figure (4- 65): Celerity values obtained by all the methods of computation for all the reaches.

The figure shows that the celerity calculated by using the user-determined overlap and cross-correlation are identical. Moreover, the values computed by cross- correlation function, user-determined overlap and sediment mass balance for the amplitude value corresponding to probability range (80%) of the second reach (between points 3 and 2) are highly similar. As noticed in E1, the higher probability range, the less value of celerity obtained. As the range of difference between the values computed by different method and using 80% probability ranges for all the reaches is relatively low compared to the difference observed in the experiment E1.

The comparison between E1 and E6 was performed to demonstrate the effect of varying the water discharge on the celerity value inside the channel with the same reach. Reach 2 that bounded by points 2 and 3 in both experiments was used to demonstrate the comparison.

Figure (4-66) demonstrates the values of celerity for different discharge values for all the methods used in the calculation and all the probability ranges.

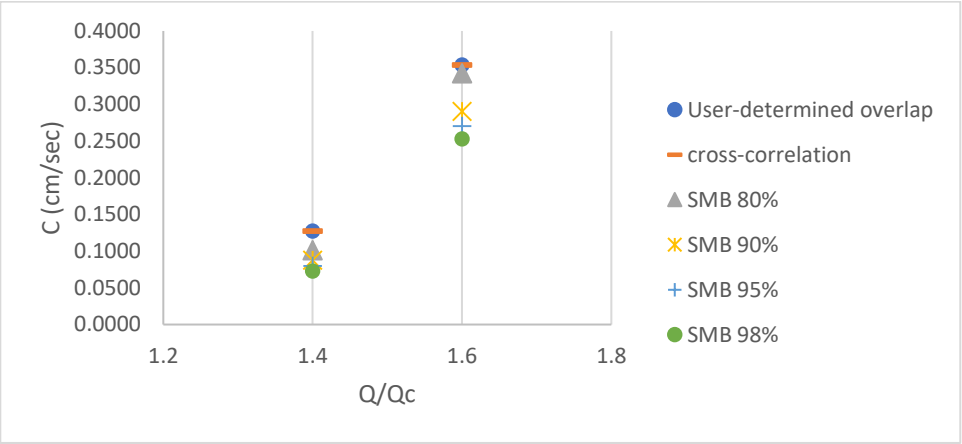

Figure (4- 66): Celerity values for different flow rate computed by different methods.

Based on the results shown, the celerity is an increasing function of discharge. Additionally, the range of variation in values between all the applied methods is less in case of lower discharge (1.4 Q_c).

4.4 Comparison with some of previous studies.

Many studies in literature have been performed with respect to different parameters mentioned previously in eq.(I) to assess the dependency of the scour depth on each parameter to have an overall understanding of the boundary conditions associated with the scour phenomenon.

Comparative graphical representation is introduced to compare the scour evolution and fluctuation of previous tests performed under steady clear-water and live-bed to the present one. Basically, the present study is a follow up to the experimental campaign started by Radice and Lauva (2017). Therefore, figure (4-67) shows a significant match between the data obtained from both studies. Furthermore, figure (4-68) illustrate the similarity between the present study and some of previous ones that performed under different conditions. For example, Chang et al (2004), have done sets of steady and unsteady tests under the condition of uniform and nonuniform sediments, in which the geometric standard deviation of sediment size distribution is ranging from 1.2 to 3.0. The tests (S1, S2, S5 and S6) associated with uniform sediment (size ranging form 1.0 mm to 0.71 mm) with standard deviation of 1.2 are compared with the present study. Moreover, case P1 of Hong et al (2016) experimental campaign was consider to be involved in this comparison, that has been carried out with pier size is 0.07 m and Q/Q_c is 1.78 with bigger sediment size (d_{50}=0.83 mm) in addition to test 8 that is used from Sheppard and Miller (2006) campaign which has been carried out with slightly smaller sediment size(0.27 mm) and bigger pier (0.152 m) with higher V/Vc (2.46).

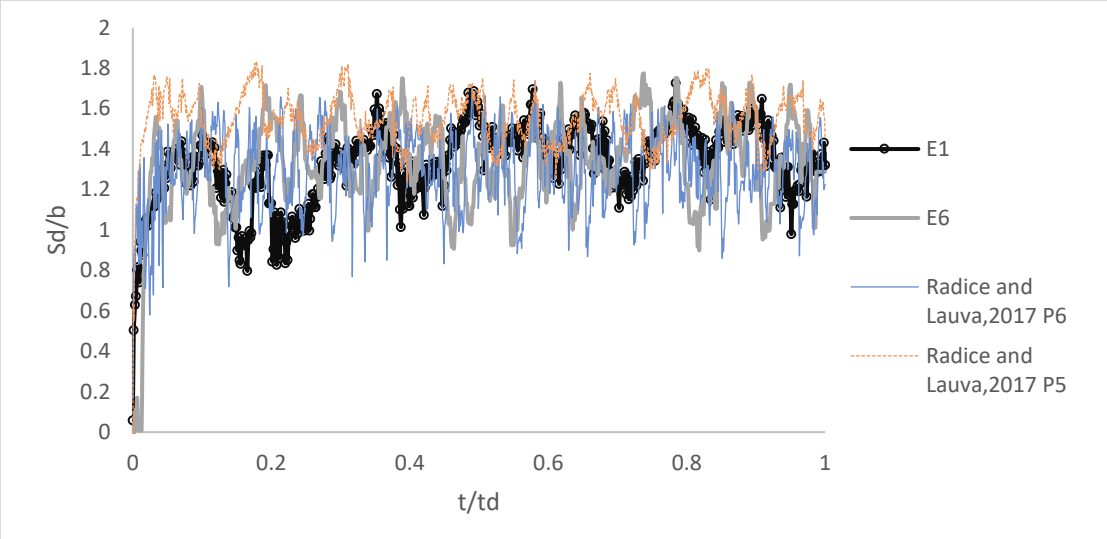

Figure (4- 67): Scour evolution and fluctuation comparison with (Radice and Luava, 2017).

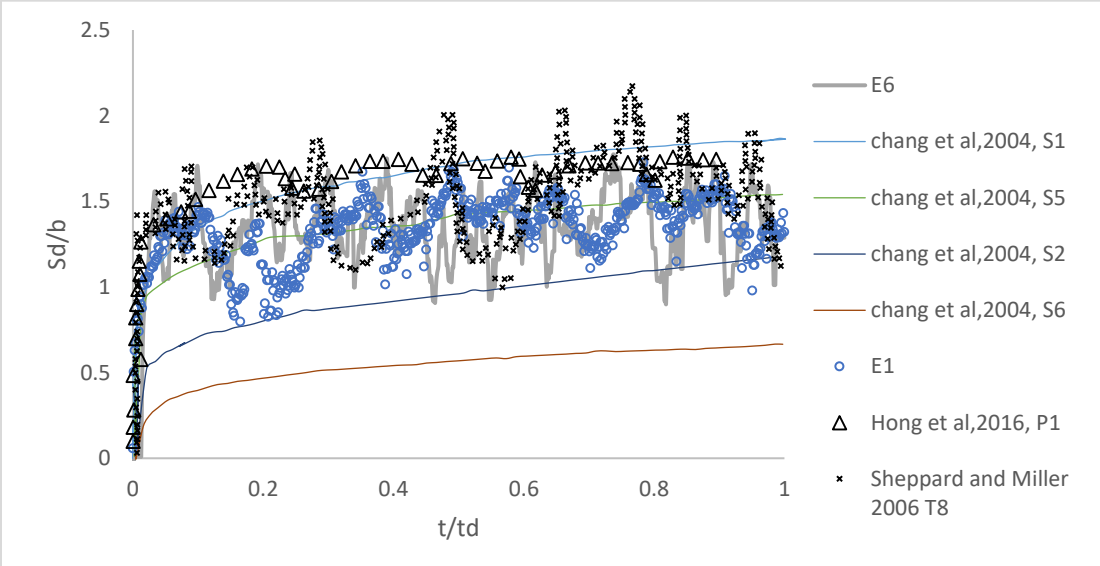

Figure (4- 68): Scour evolution and fluctuation comparison with some previous studies.

Run S1 of chang et al (2004) reached a scour depth higher than the present study due to the high velocity ratio (V/V_c=0.9), that according to Chiew and Melville (1987), the scour depth reaches its first peak at V/Vc= 1. Instead S2 and S5 that have lower velocity ratios, represent less scour evolution rate and value. Moreover, Hong et al (2016) and Sheppard and Miller (2006) have the same range of scour as the present study as both studies performed under live-bed conditions with V/Vc (1.78 and 2.46, respectively). The scour depth plummets to its trough at V/Vc = 2 approximately, then an increase noticed to reach its second peak at 4, stated by Chiew and Melville (1987), that can interpret the similarity of the data obtained by Hong et al (2016) and Sheppard and Miller with the present study.

In some studies, the maximum scour depth was focused as the most critical for structure design and vulnerability analysis purposes, mean scour depth instead was recalled in many studies as the best representation of the scour depth. Figure (4-67) shows the comparison between the values and trends obtained by current study and some of the previous ones. There is evident consistency between the present study and the others, as it is demonstrated that the mean scour depth is a decreasing function of the flow rate between Q/Q_c= 1~ 2, thereafter the mean scour increases gradually with the flow rate as shown by (Chiew and Melville,1987). On the other hand, for the maximum scour depth, there is agreement between the trend concluded by Ettmer et al (2015) and the results of the present study, that has instead a clear conflict with the results obtained by Radice and Lauva (2017), specially at Q/Q_c=1.6.

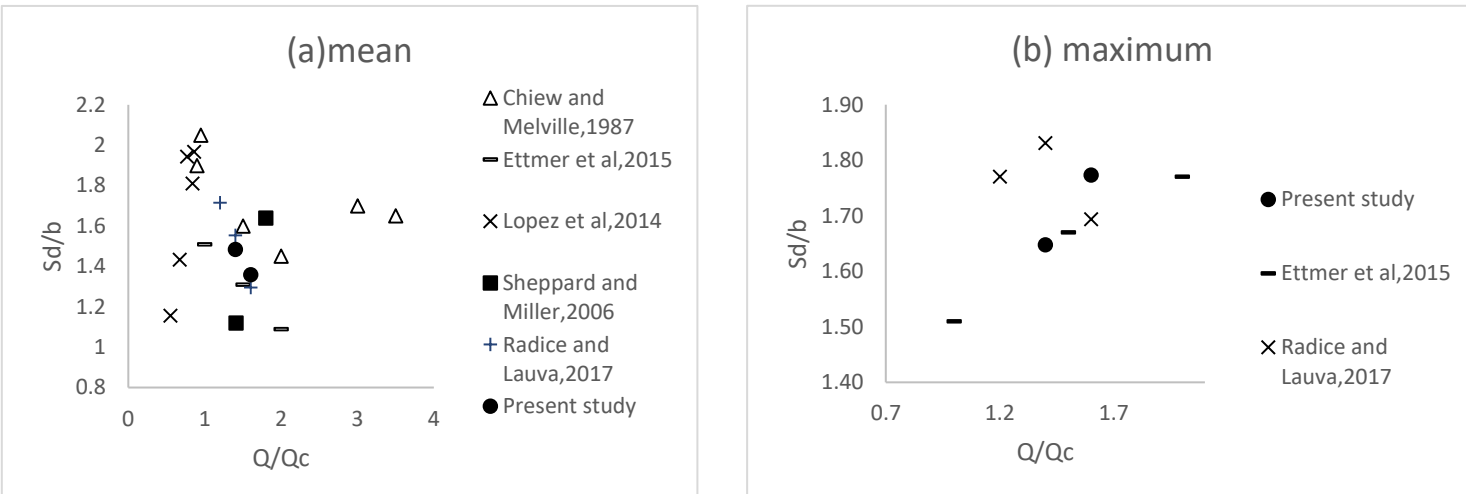

Figure (4- 69): Scour depth comparison between present study and previous ones: (a) mean scour depth,(b) maximum scour depth.

Moreover, the dimensionless equilibrium time for both discharge values are identical to the ones computed by Radice and Lauva (2017) as shown in figure (4-70).

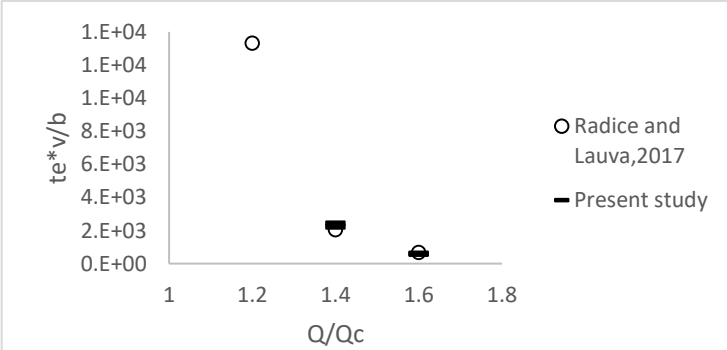

Figure (4- 70): Dimensionless equilibrium time similarity with (Radice and Lauva,2017).

5. Live-bed scour Unsteady flow study.

In fluvial rivers, significant transport of bed materials often takes place during peak-flow discharge in a flood event. For large rivers, the duration of a flood event may last for a few months, but for others the unsteadiness of a flood can be pronounced. The general practice of employing peak-flow discharge to evaluate the maximum scour depth for design may be questioned because the maximum scour depth occurring under a flood hydrograph can be much smaller than the calculated value using peak-flow discharge. In other words, using the peak-flow discharge for design can greatly overestimate the maximum scour depth in comparison to the actual conditions under the flood hydrograph. Therefore, when the flow unsteadiness is pronounced, the temporal effect on scour depth should be considered (chang et al, 2004). In clear water, the statement is accurate because the equilibrium time is long. Instead, in live-bed conditions, the associated scour depth behavior is quite unknown and worth exploring.

By imposing a stepwise water discharge hydrograph to the experimental run leads to deep investigation of unsteady conditions influence on the live-bed scour. Additionally, equilibrium sediment feeding was varied according to flow hydrograph.

Like steady state conditions, the startup and shut down were carried out in the same way; however, the operation of any experiment under the unsteady conditions is different. For each experiment, a predefined stepwise hydrograph was used to determine the steps of flowrate and sediment discharge. Therefore, the discharge change was carried out by an instantaneous reduction of the flowrate to reach a value less than the critical discharge (around 8 l/sec) to prevent any possible sediment motion and further induced scour during this transition period. After that the flowrate was increased simultaneously with the reactivation of sediment feeding components with the corresponding equilibrium sediment discharge.

5.1 Scour unsteady-experiments.

Four experiments were carried out under different chosen boundary conditions (T1, T2, T3 and T4). Three water discharge values were determined to build the addressed hydrograph for each experiment that were 1.2 Q_c, 1.4 Q_c and 1.6Q_c, each hydrograph has rising and recession limb to start and end with discharge (1.2 Q_c). Indeed, the experiments differentiate based on the upstream distance from the pier nose of the nearest migrating dune approaching the scour hole at the time the discharge modification. In a deterministic sense, one can expect that the scour trend just after the change of discharge depend on the position of the nearest coming dune. The dunes were detected clearly in higher flow rate (1.4 Q_c and 1.6 Q_c); contrarily, they were not well developed in the least discharge value (1.2 Q_c). Table (5-1) illustrates the values of

flow rate used in to build the hydrograph and their corresponding equilibrium sediment discharges. Noting that the values of water depth at different discharges are measured under the steady conditions.

Q (l/s)	Q/Qc	H (mm)	V (m/s)	Fr	Φ	Qs (m2/s)
15.80	1.2	133.51	0.296	0.258	0.002919	7.81E-07
18.40	1.4	135.78	0.340	0.294	0.023091	6.18E-06
21.03	1.6	133	0.395	0.346	0.097422	2.61E-05

Table (5- 1): Water and sediment discharges characteristics (Radice and lauva,2017).

Experiment	Description
T1	this experiment was carried out to have an initial envisage of behavior and evolution of bedforms and scour depth according to an imposed hydrograph with no attention payed to the place of the nearest approaching dune.
T2	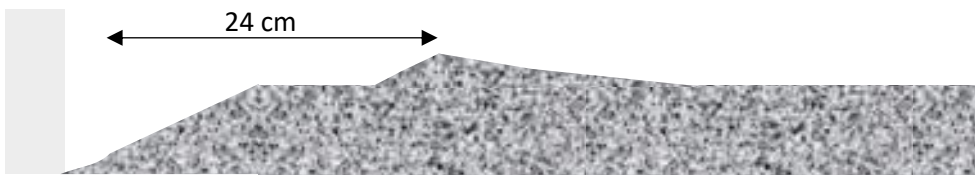
T3	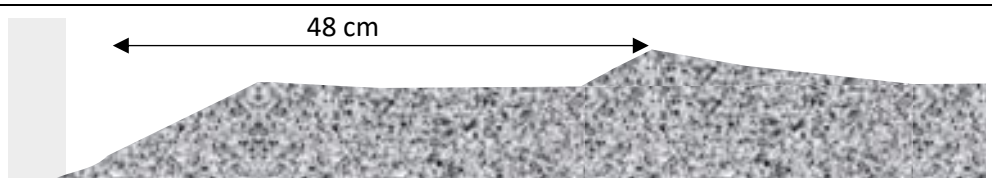
T4	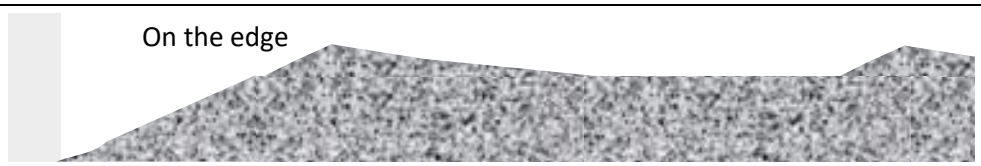
Measuring points positions	
Legend	Pier Measuring point **Note:** the written distances are measured from the pier nose in centimeters.

Table (5- 2): Experiments set up and illustrative description.

The experiments were run with the same placement of the measuring points as E1 and E6 in steady conditions, as the first point is placed at the deepest point of the scour hole at the stagnation zone in front of the pier, while the others were placed upstream of the scour hole at 25, 48 and 116 cm, respectively. All the experiments were performed with a prescribed hydrograph; however, T2, T3 and T4 were carried out with a control of the nearest approaching dune that is 24 cm, 48 cm from the pier and just upstream of the scour hole for T2,T3 and T4 respectively, as shown in table (5-2).

5.2 Unsteady-Experiments Analysis.

5.2.1 Scour progression phase.

The evolution of scour depth was recorded in experiments T1 and T2 for unsteady condition. Figure (5-1) shows comparatively the evolution phase of experiments E1 and E6 that performed in steady conditions, and T1 and T2 of unsteady. Due to an unknown reason, unexpected progression phase was recorded in T2 that contradicts in behavior with T1 and previous experimental campaigns done under the same boundary conditions by Radice and lauva (2017).

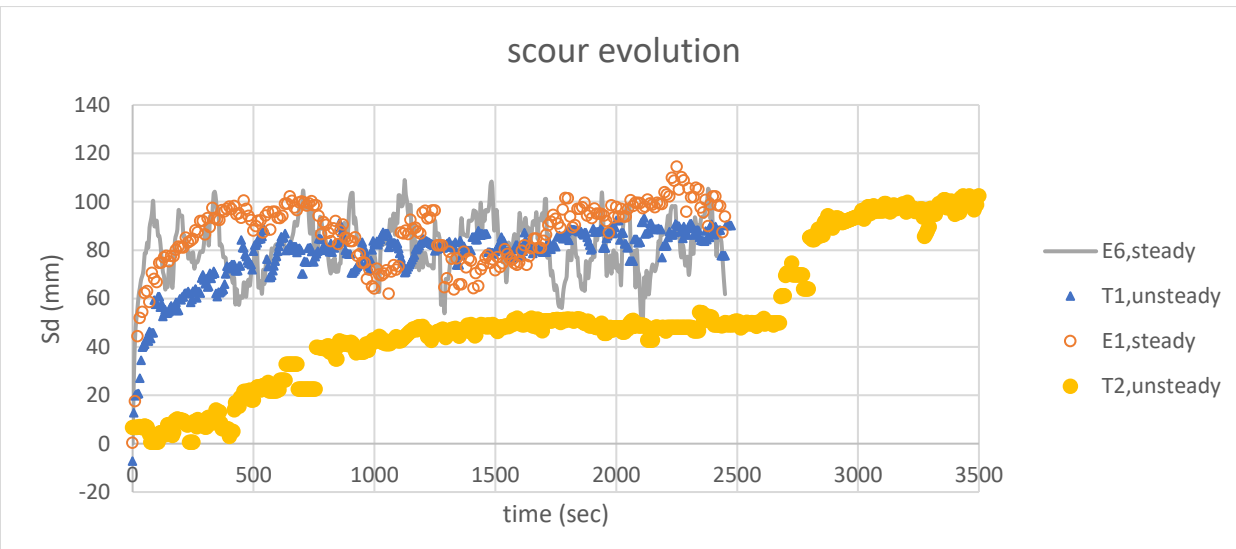

Figure (5- 1): Scour evolution in different steady and unsteady experiments.

Therefore, the scour progression phase was eliminated from T2 and was not contributing in any further analysis. After the elimination of the untrusted evolution phase, the scour evolution comparison will be clear between E1, E6 and T1 that present the scour evolution for discharge of $1.4Q_c$, $1.6Q_c$ and $1.2\ Q_c$ respectively.

Obviously, the evolution rate is a decreasing function of the flowrate, as shown in figure (5-1), the evolution rate of the scour depth was slower during experiment T1 in comparison with E1 and E6 that have higher discharge values. Furthermore, the depth fluctuation during the progression phase is an increasing function of flowrate that is

clearly depicted from figure (5-1), as a milder progression behavior presents at discharge of ($1.2Q_c$) than the higher ones.

The scour evolution was observed and measured only in experiments E1, E3, E6 and E7 for the steady conditions, and only T1 in unsteady condition after eliminating that of T2. The dimensionless equilibrium time (t_e*v/b) is computed from the measured equilibrium time and calculated velocity as presented in table (5-3).

Experiment	Q/Qc	te(sec)	V(m/sec)	teV/b
E1 steady	1.4	440	0.33	2420
E3 steady	1.4	410	0.32	2214
E6 steady	1.6	85	0.41	576.58
E7 steady	1.6	90	0.41	610.5
T1 unsteady	1.2	1855	0.298	9275

Table (5- 3): Equilibrium time characteristics for different steady and unsteady experiments.

The results of the dimensionless equilibrium time are graphically represented in figure (5-2) which concludes that the dimensionless equilibrium time is a decreasing function of discharge.

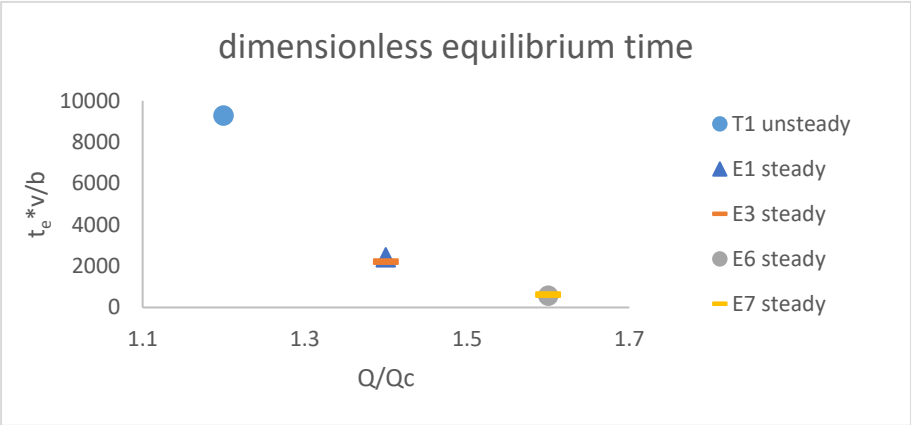

Figure (5- 2): Dimensionless equilibrium time for steady and unsteady experiments.

5.2.2 Scour depth and transition phases.

The transition phase is the period needed to address the new step of the hydrograph to the system. Usually, this period is limited to 5 minutes that are needed to lower the discharge under the critical one and adjust the hopper slot, thereafter, increasing the discharge to the designed value simultaneously with reactivating the hopper.

Each hydrograph consists of 5 discharge steps ($1.2Q_c$, $1.4Q_c$, $1.6Q_c$, $1.4\ Q_c$, and $1.2Q_c$), and they vary instead in the time steps. Table (5-4) and figure (5-3) represents the

hydrographs time steps applied to each experiment, and the total period of each hydrograph.

Hydrograph steps (seconds)				
steps	T1	T2	T3	T4
1.2 rising	2480	5855	1905	1060
1.4 rising	1910	1880	2175	2290
1.6 rising	1295	1760	1950	1905
1.4 recession	1725	2210	2160	1975
1.2 recession	3105	2760	2370	2650
Total period (sec)	10515	14405	10560	9880

Table (5- 4): Hydrographs time steps for unsteady experiments.

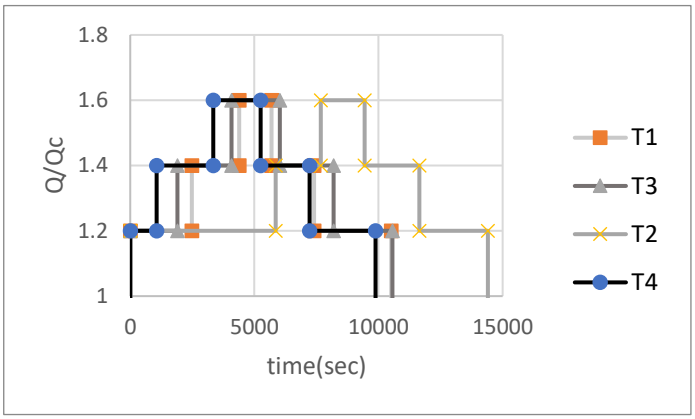

Figure (5- 3): Hydrographs time steps.

The time steps that used for water hydrographs is, consequently, applied to the sediment feeding hydrographs. Figure (5-4) depicts the water and sediment discharges hydrographs addressed to the four unsteady experiments.

(a)

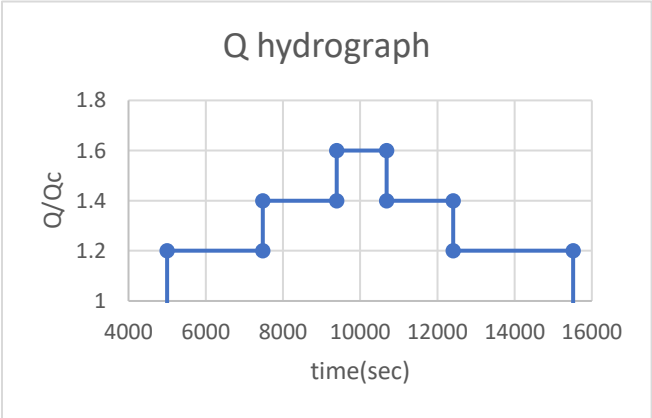

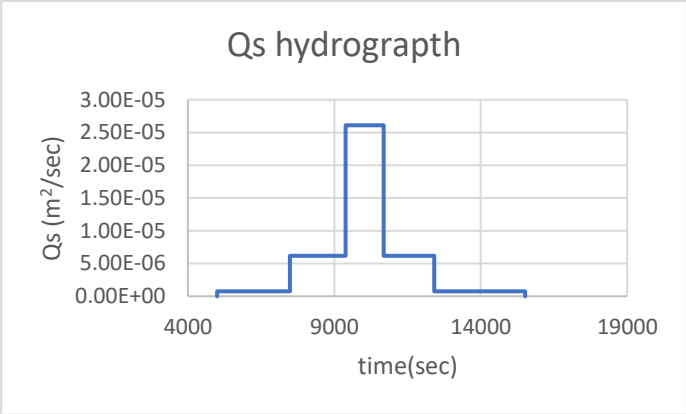

(b)

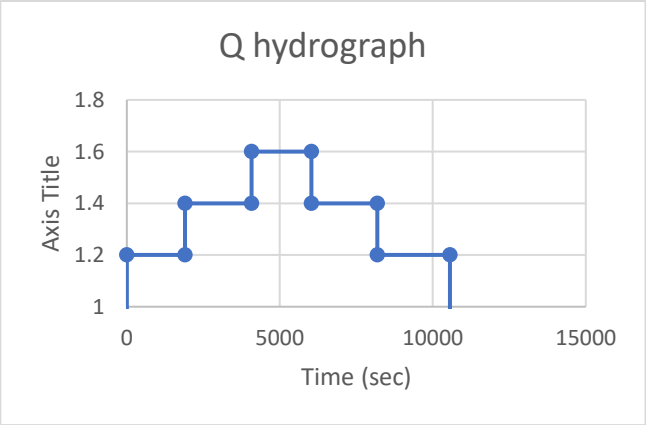

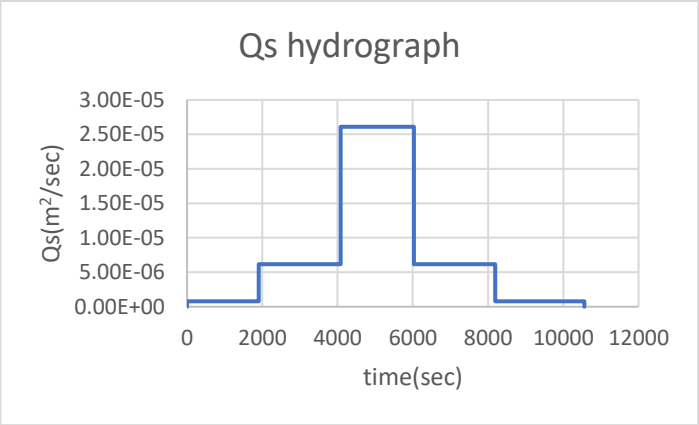

(c)

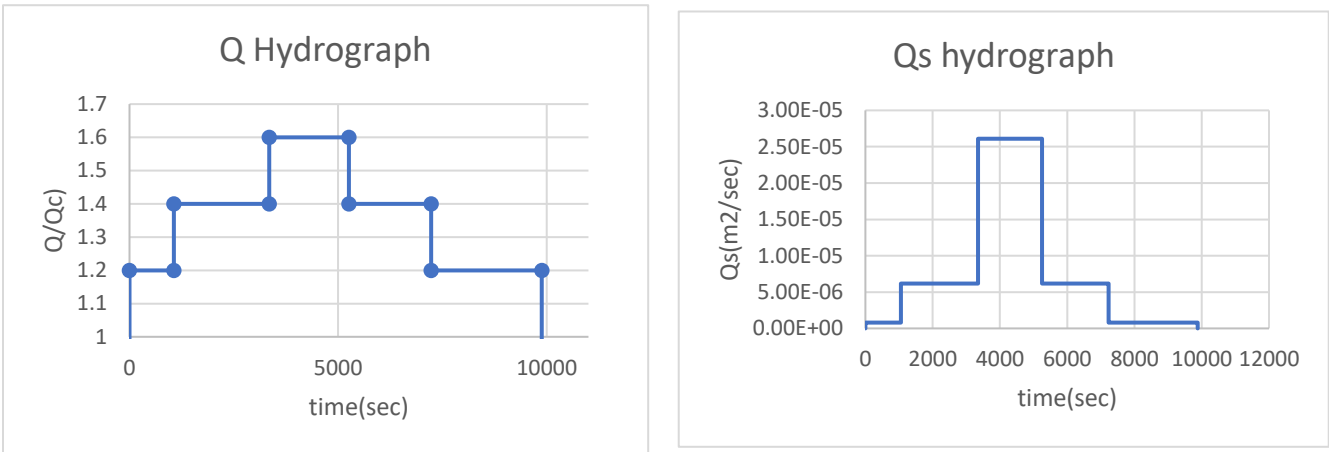

(d)

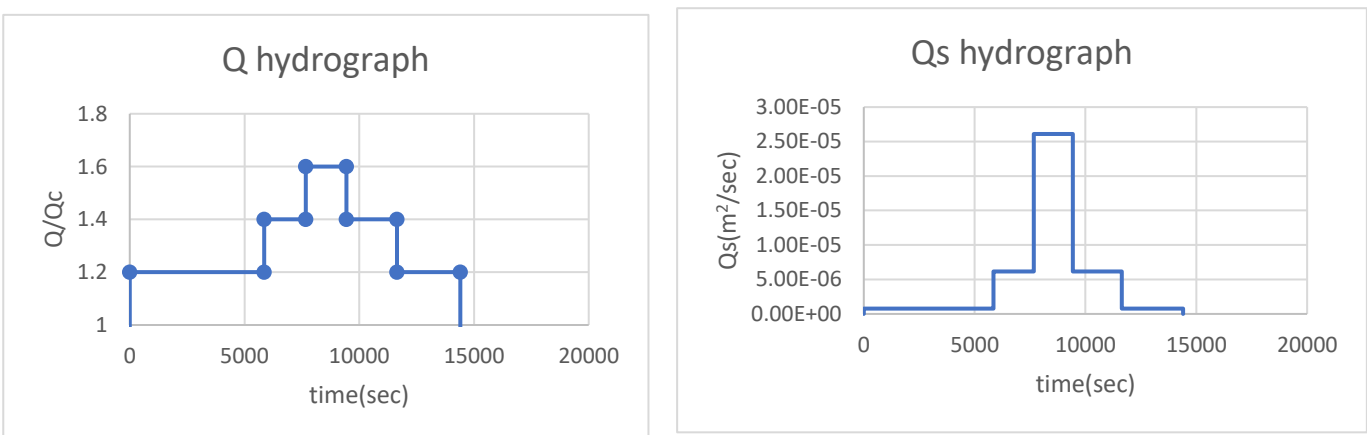

Figure (5- 4): Left panels: water hydrographs. Right panels: sediment feeding hydrograph. (a) the hydrographs applied to T1. (b) hydrographs applied to T2. (c) hydrographs applied to T3.(d) hydrographs applied to T4.

the measurements were obtained at all the points; however, the scope of the study is on the scour depth variation at the stagnation point (0.5 cm) from the pier face. Figure (5-5) depicts the temporal evolution of scour depth has throughout the hydrograph time steps in T1. Clearly, minor depth fluctuation is emerged in first time step during the progressive evolution of the scour depth at Q=1.2 Q_c, while the scour depth increasingly fluctuated temporally at higher discharges (1.4Q_c and 1.6Q_c) through the rising limb. Thereafter, arriving at the recession limb, a dramatic increase in scour depth is induced by lowering the discharge to 1.4Q_c. at the end of the hydrograph, the scour depth maintained relatively constant till the scour hole refill occurred gradually to reach the equilibrium scour depth at the end of 1.2Q_c step.

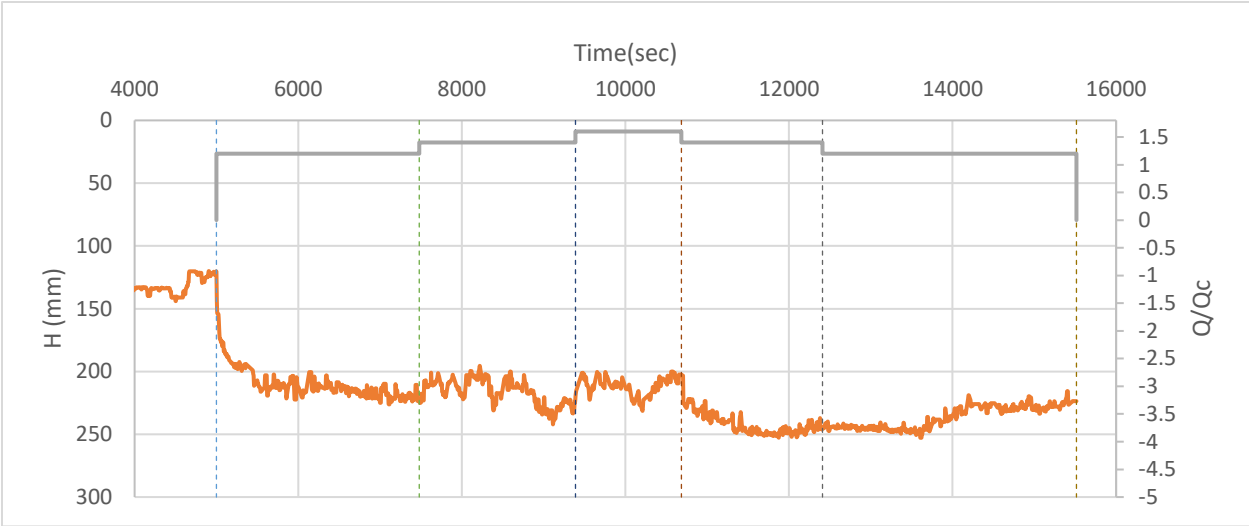

Figure (5- 5): Scour depth temporal evolution and variation during T1.

Furthermore, sensitivity analysis of nearest migrating dune approaching the scour hole at the time of water discharge modification is performed to find out the influence on the scour fluctuation at the pier nose during the transition phase.

For experiment T2, the discharge modification was carried out when the nearest migrating dune front is at 24 cm upstream of the pier nose. The coincidence between the existence of dune front at 24 cm and the exact transition step predefined in the prescribed hydrograph, is rarely possible; therefore, the hydrograph steps can be marginally different from those which defined prior to the experiment. Consequently, the hydrograph depicted in figure (5-4) is the modified one after performing the experiment.

Figure (5-6) represents the temporal scour depth fluctuation and variation, where points 1 and 2 are at 0.5 cm and 25 cm upstream of the pier nose, respectively. Obviously, the discharge modification from $1.4Q_c$ to $1.6\ Q_c$ during the rising limb, occurs when the migrating dune front arrives approximately at point#2, consequently, the refilling of the scour hole needs an adequate time to allow the dune to cover the distance between the two points that takes 155 seconds as measured graphically from the point of transition to the consecutive scour peak. Similarly, to change the discharge from $1.6Q_c$ to $1.4Q_c$ during the recession limb, 400 seconds needed for the approaching dune to start refilling the bottom of the scour hole. The scour fluctuation mounted gradually during the rising limb to reach its peak at $Q=1.6Q_c$. Inversely, the fluctuation magnitude decreased thoroughly during the recession limb.

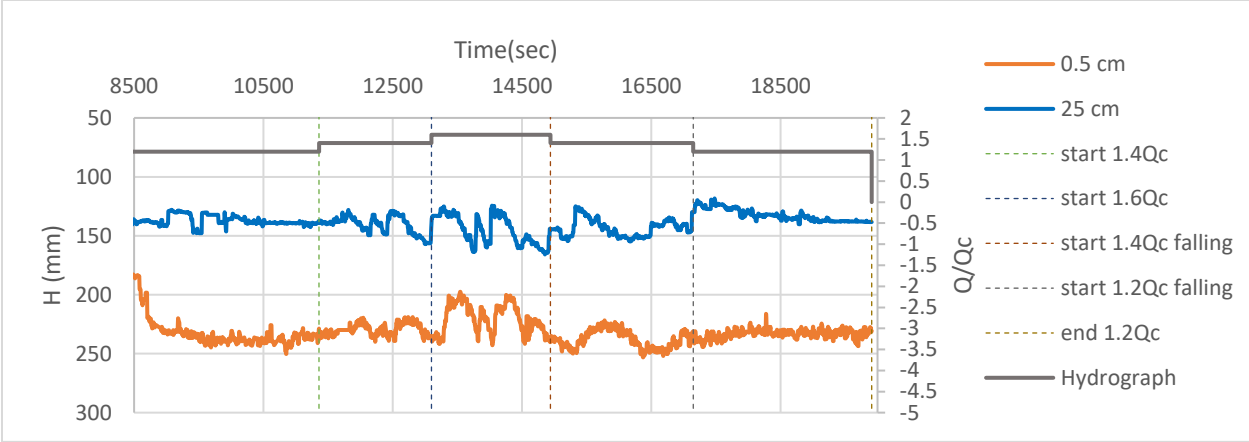

Figure (5- 6): Scour depth temporal evolution and variation during T2.

Further experimental investigation was performed by changing the discharge when the nearest dune approaching the pier face is at 48 cm upstream. Figure (5-7) presents the acquired data at points 1 and 3 that are placed at 0.5 cm from the pier nose and at distance of 48 cm upstream respectively. At each transition phase, the dune takes longer time to refill the scour hole and by reaching the deepest point within the hole. In other words, the refilling by the migrating dune between 1.4 Q_c and 1.6 Q_c during the rising limb is measured graphically to be 195 seconds compared to 155 seconds in experiment T2 due to the longer distance covered. Additionally, in case of decreasing from 1.6Q_c to 1.4 Q_c during the recession limb, it takes 450 seconds to cover the distance, and longer time 730 seconds is needed in case of transition between 1.4 Q_c and 1.2 Q_c.

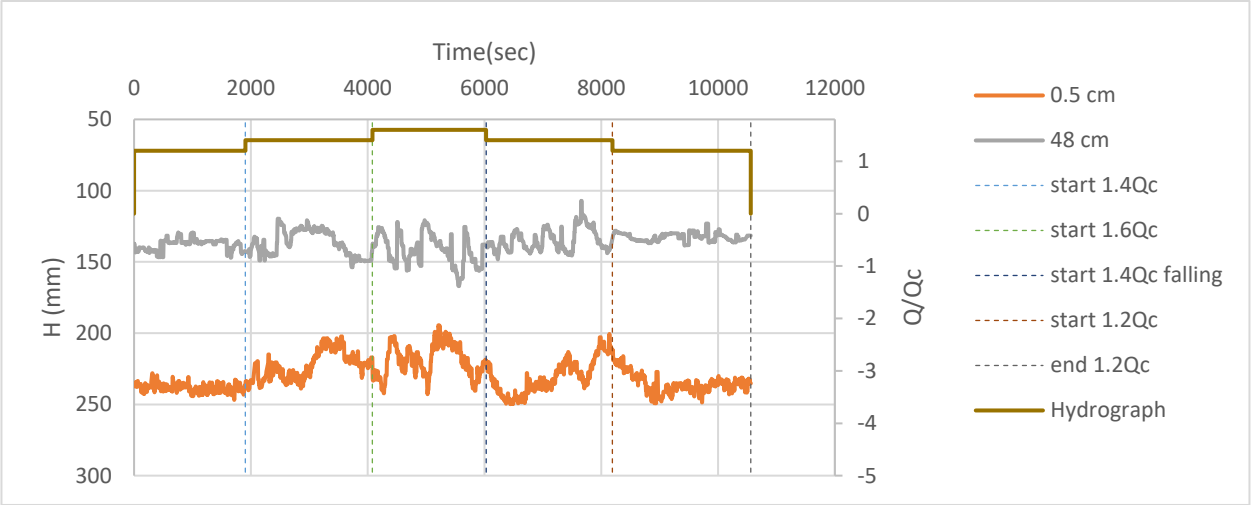

Figure (5- 7): Scour depth temporal evolution and variation during T3.

Experiment T4 was performed with the same concept of T2 and T3, but the discharge modification carried out when the nearest dune front is existing on the scour hole edge compromising with the prescribed hydrograph. Figure (5-8) shows the data acquired at

point#1 that placed at the pier face. The depth fluctuations at all the transition phase illustrate an immediate refill of the scour hole due to the close existence of the refilling dune to the bottom of the scour hole at the moment of discharge modification, unlike T2 and T3 where the dune needs a certain time to reach the bottom of the scour hole.

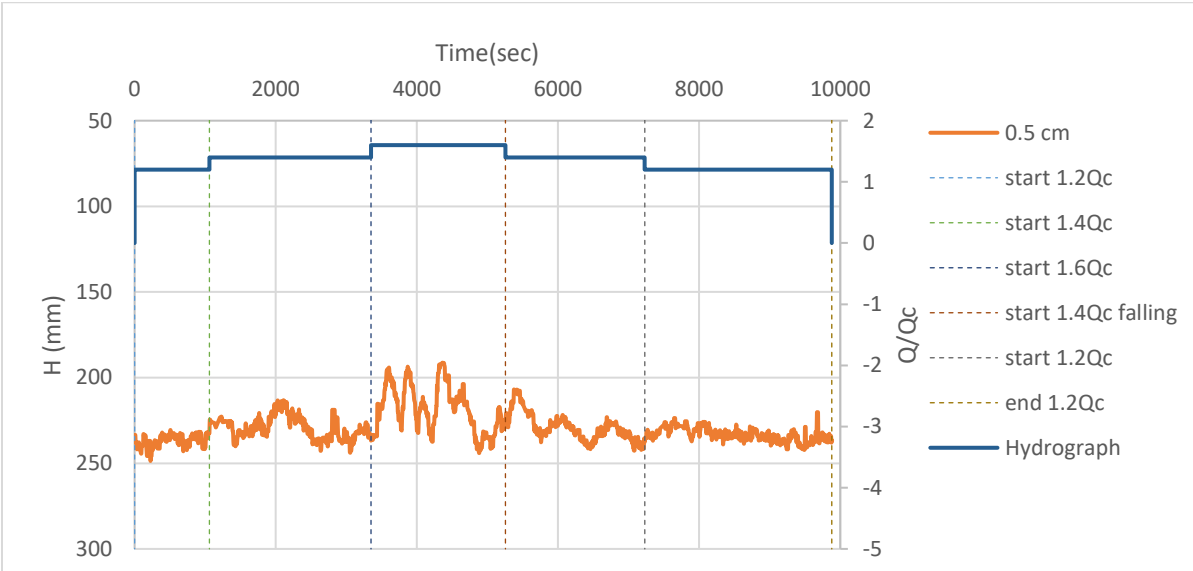

Figure (5- 8): Scour depth temporal evolution and variation during T4.

Table (5-5) represents graphically the transition phases in T2, T3 and T4 through the hydrograph steps.

	from 1.2 to 1.4 (rising)	from 1.4 to 1.6 (rising)	from 1.6 to 1.4 (recession)	from 1.4 to 1.2 (recession)
T2	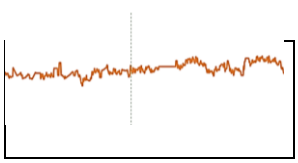	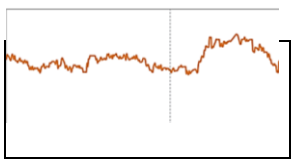	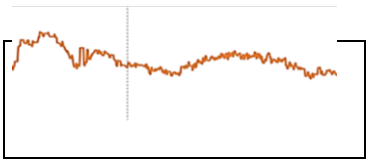	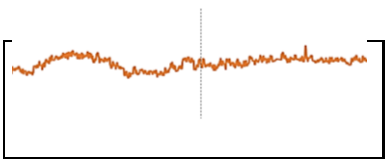
T3	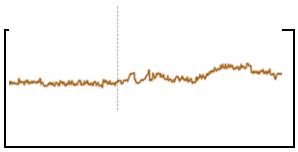	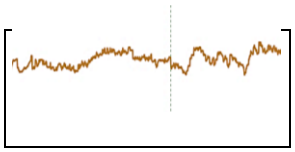	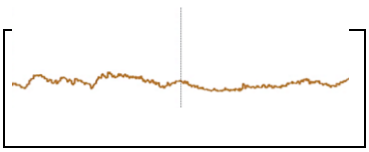	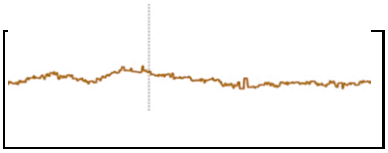
T4	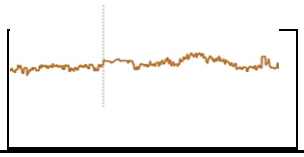	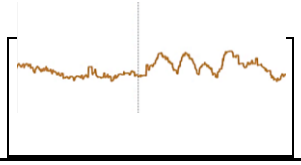	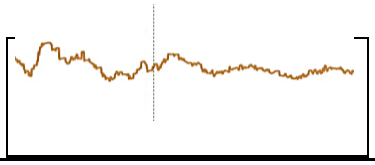	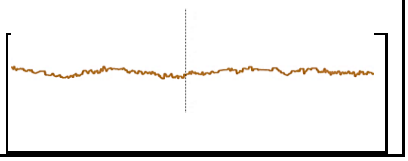

Table (5- 5): Transition phases in T2, T3 and T4.

By focusing on the transition phases in T2, T3 and T4, the same scour hole refilling behavior is emerged in T2 and T3. For all the experiments, the transition phase between $1.2Q_c$ and $1.4Q_c$ during the rising limb has the same pattern of gradual decreasing in the scour depth.

For T2 and T3, the scour depth peaked after certain time before the first refill after the discharge modification from $1.4Q_c$ to $1.6Q_c$. Although, the maximum scour depth varying before the arriving of the first refilling dune, the magnitude of refilling does not record any significant difference between T2 and T3 that is 36.6 mm and 35 mm, respectively, also this refilling pattern has not changed for the consecutive refilling events. Therefore, the dunes are rapidly reformed to a uniform bigger size than those of $1.4Q_c$ immediately after the discharge alteration to dynamically equilibrate with the new system conditions. During the recession limb, T2 and T3 has similar trend of increasing the scour depth then gradual decreasing after the arrival of the nearest dune to replenish the scour hole.

Instead, for T4, for the transition between 1.4 Q_c and 1.6 Q_c during the rising limb and all the recession limb, the scour depth shows an immediate decrease just after discharge modification due to the rapid feeding occurred by the nearest dune that exists on the edge of the scour hole.

In the unsteady flow experiments, general observations show that the scour depth increases steadily during the rising period of the hydrograph, and changes only slightly during the recession period (chang et al,2004). The previous conclusion obtained based on experiments of bridge pier scour carried out under unsteady clear-water scour conditions with uniform and nonuniform sediments. Similarly, flood wave approach was used in the investigation carried out by (Lopez et al, 2014). Figure (5-9) represents the comparison of the temporal evolution of dimensionless scour between T1 of the present study and the mentioned studies under the condition of clear water. It is evident that then scour evolution phase in case of live bed condition is faster and higher than this of clear water. Furthermore, the temporal fluctuation in case of live bed has no specific trend, but it fluctuates between through the hydrograph steps, unlike the clear water condition where the scour depth increases gradually over the whole time. Moreover, as (chang el al,2004) mentioned, the variation of scour depth during the recession phase is minor compared to the rising phase, in live bed instead, a dramatic increase in scour depth emerges during the start of the recession phase.

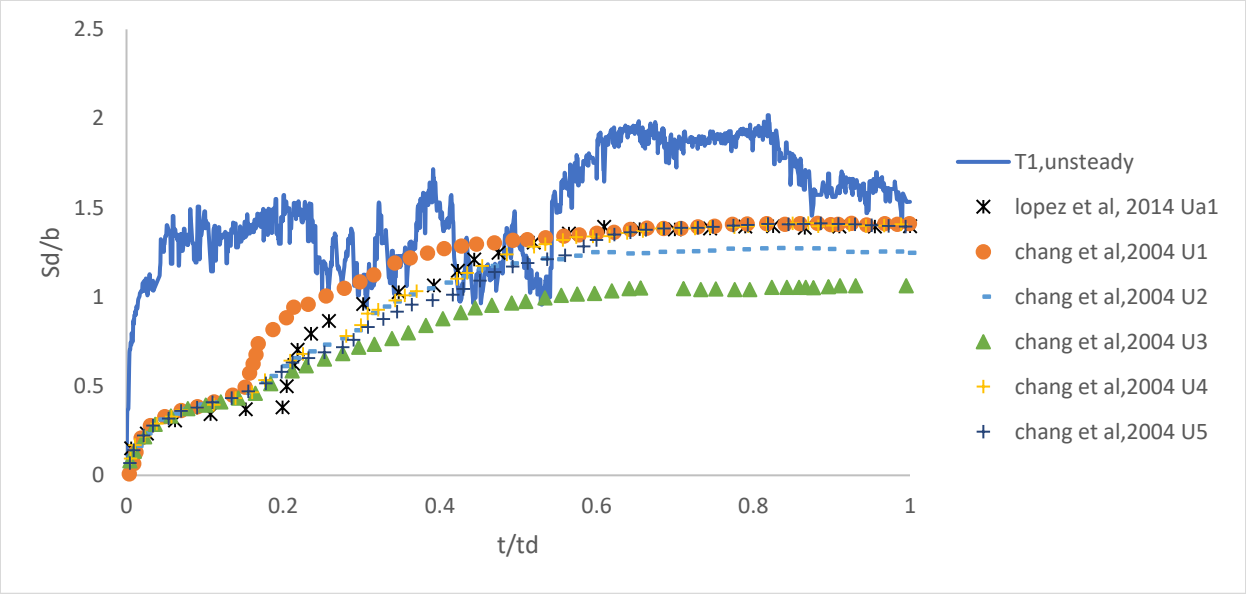

Figure (5- 9): Scour depth comparison between unsteady clear water conditions and unsteady live bed conditions.

5.2.3 Scour depth variation.

The analysis of scour depth is performed based of the calculation of maximum, mean and minimum scour depth values for each time step corresponding to the assigned hydrographs for the four experiments. Figure (5-10) presents graphically the values of dimensionless scour depth (Sd/b) for all the carried out runs. interestingly, It is evident that the least values of scour depth occur at the peak of the hydrograph for all the runs, Instead, the scour depth increases during the recession phase. For mean scour depth, for all the runs, plummets to reach its trough at the peak discharge, then increases gradually to reach its peak at the last discharge step of 1.2 Q_c, except for T1 where the peak values exist at the penultimate step. Similarly, the least maximum and minimum scour depth are at the hydrograph peak. the maximum scour depth increases gradually in recession limb, the minimum one instead increases dramatically.

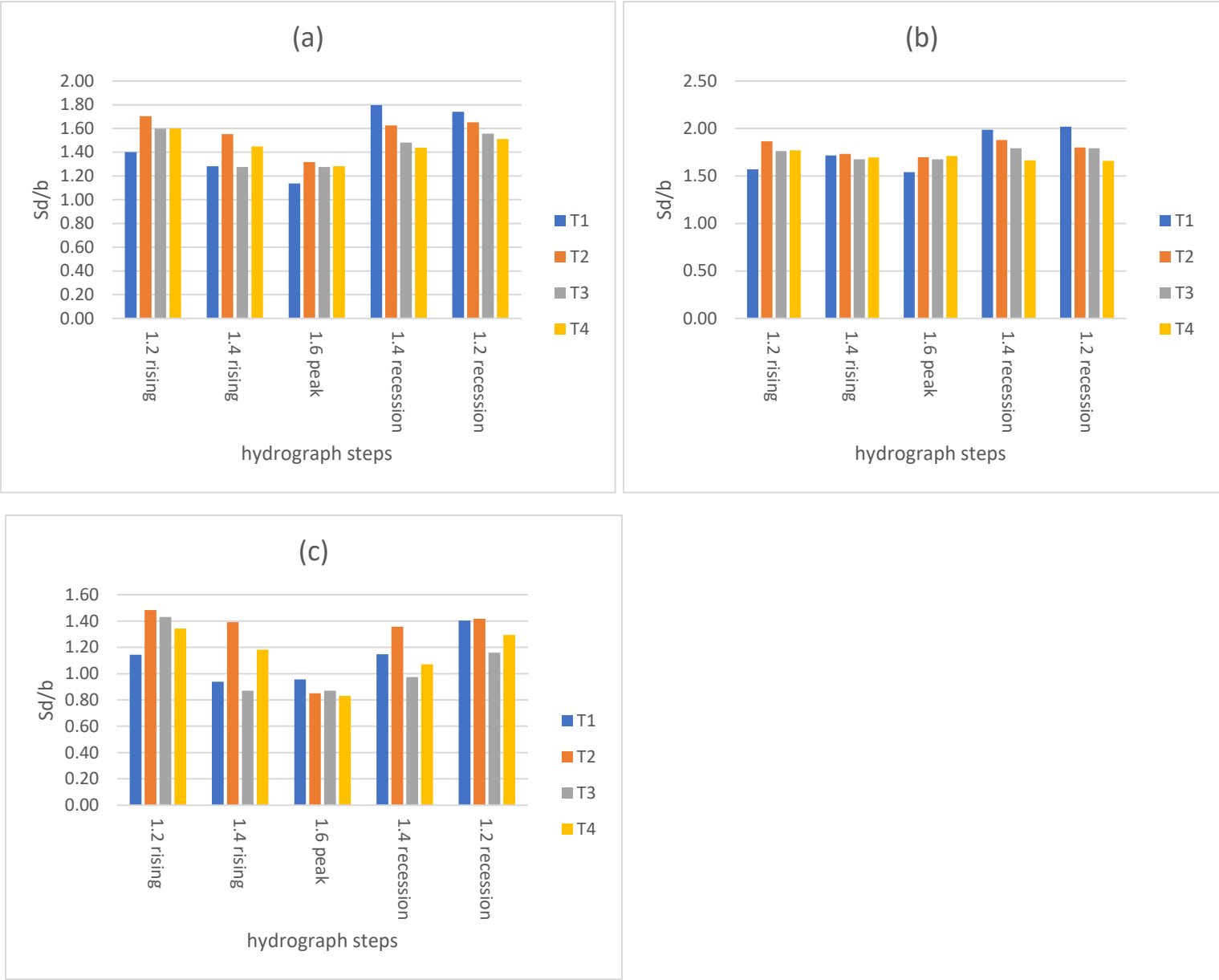

Figure (5- 10): Mean, maximum and minimum scour depth for different experiment: (a)mean scour depth,(b) maximum scour depth,(c) minimum scour depth.

For better quantitative representation, averaging the scour depth values at each discharge step for all the experiments together to have unique values of scour at each discharge step was done. Figure (5-11) depicts the trend of maximum, mean and minimum scour variation through a stepwise hydrograph for unsteady live bed condition.

It is depicted that during the rising phase, dramatic decrease of the mean and minimum scour depth is present to reach its trough at the peak flow rate, then a gradual increase is noticed. Therefore, U shape of scour variation throughout the imposed hydrograph is

present for mean and minimum scour depth. However, marginal variation in the maximum scour depth is observed to be present between the hydrograph steps.

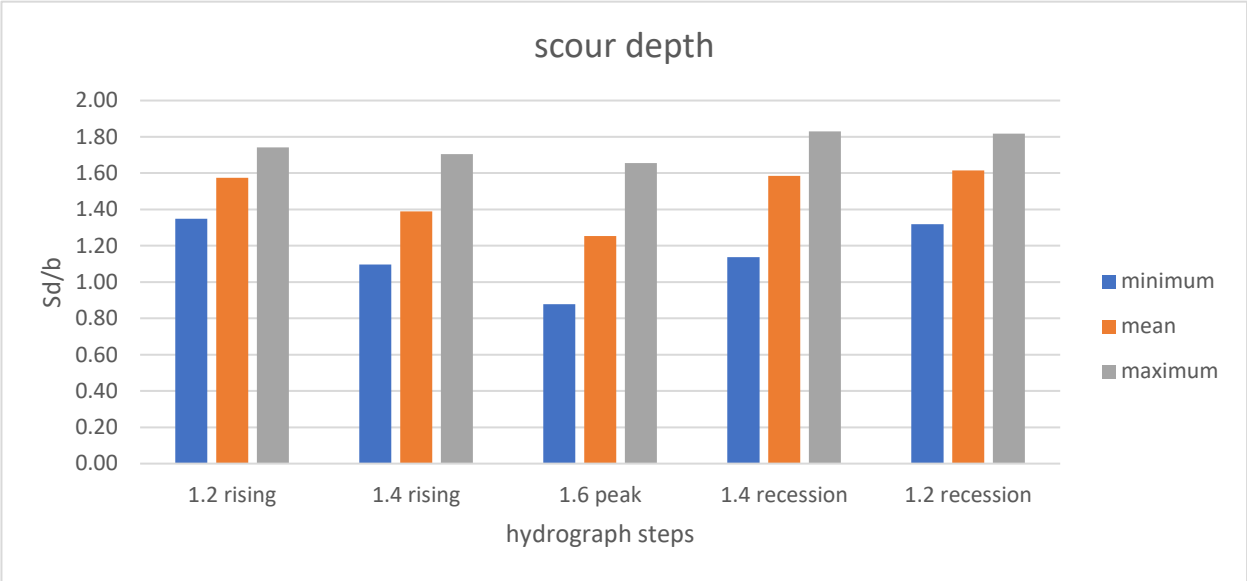

Figure (5- 11): Mean, maximum and minimum scour depth for unsteady live bed condition.

"Since previous investigations _Chang et al. 2004; Oliveto and Hager 2005; Lopez et al. 2006_ showed that the recession period of hydrograph plays a minor role in the scouring process, therefore, only the effect of rising limb of a hydrograph is herein addressed" a statement that claimed by (lai et al, 2009) to initiate their investigation in unsteady clear water scour conditions. However, the previous claim can not be valid in the present study of live bed conditions. By monitoring the scour depth development in the recession phase, it is evident that the scour depth increases during the recession limb. The difference in value between the scour depth measured at $1.4Q_c$ for the rising and the recession phase is not significant and can be interpreted by either saying that this difference is within the confidence value of the mean scour depth, or that the undermining rate of bed transport upstream to refill the scour hole due to decreasing the discharge is higher than the decreasing rate of dragging force exerted on the sediment existing at the pier zone which induce the momentum of rapid scouring at the beginning of the new step after the peak ($1.4Q_c$) and dumping at the end to reach the dynamic equilibrium similar to the rising phase. Therefore, the clear interpretation must be obtained by performing further investigation with larger time steps to emphasize if the scour depth is going to reach the equilibrium scour depth as in the rising phase, or otherwise is going to fluctuate on a higher scour depth values.

Figure (5-12) illustrates the mean, maximum and minimum scour depth for obtained under steady conditions for E1, E3, E6 and E7 comparatively with the values obtained under unsteady conditions. The present study shows no significant difference between

the maximum scour depth reached during the peak flow under the steady conditions and the unsteady conditions.

Furthermore, the comparison between steady and unsteady based on the mean depth measured shows a difference during the recession limb. It is always clear that, the mean and minimum scour depths are a decreasing function of the flowrate till a certain value under steady conditions as stated by Chiew and Melville (1987). However, the same behavior is concluded from the presented results. For design purposes, considering the peak discharge or the rising phase to be a platform, undoubtedly, leads to underestimation of the scour depth, consequently, the scour variation during the recession limb is worth investigation. Therefore, based on the present study, the argument stated by Chiew and Melville (1987) that the data should be presented considering the mean scour depth cannot be fully trusted for design purposes, as the maximum scour depth is always higher than the mean one.

On the other hand, the minimum scour depth is always coincident under all condition either steady or unsteady for both rising and recession limb.

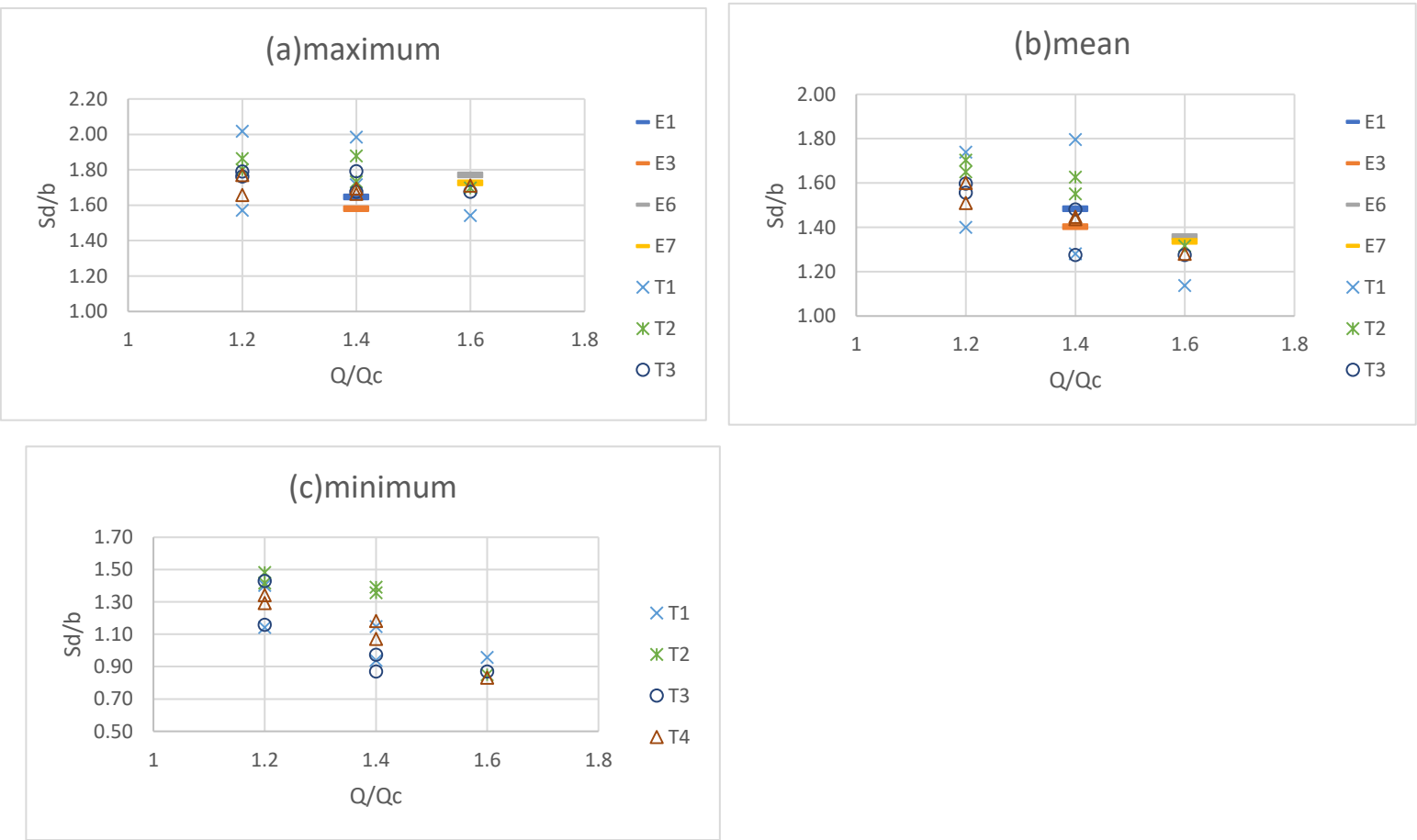

Figure (5- 12): Scour depth comparison between steady and unsteady conditions. (a) maximum, (b)mean,(c) minimum.

Conclusions.

The study presented results of laboratory experiments for live-bed at a cylindrical pier in covered flow. This study was a follow up of the investigation initiated be Radice and Lauva (2017) to understand the local scour phenomenon in covered flow, in which the findings were emphasized and deepen in the present study. In other words, this study amassed the depiction of scour occur at a cylindrical pier by exploring the geometric characteristics of the scour hole and introducing the effect of flow unsteadiness on the live-bed pier scour.

Seven runs were performed in steady conditions and varied based on the flow discharge and the positioning of the measuring points. The imposed discharges were 1.4 and 1.6 times the threshold flow rate for sediment transport. The time needed to reach the dynamic equilibrium is a decreasing function of the flow rate. Furthermore, the range of scour depth variation is an increasing function of the flow rate, as mean and minimum scour depths are a decreasing function with the flow rate, unlike, the maximum scour depth that is an increasing function of the flow rate.

At lower discharge, the fluctuation of the scour depth at the pier is controlled by the incoming dunes as implied by the similarity of the calculated amplitudes. However, the higher amplitudes that computed on the scour hole slope can be primary interpreted by the mechanism of sediment avalanche occurs within the hole due to the exerted load by the dune located on the hole edge which leads to instant failure of inclined surface and higher fluctuation in the points on it. On the other hand, at higher discharge, the amplitudes for all the points within the scour hole are similar and higher than the points located upstream of the scour hole that represent a gradual increase in the dunes size till reaches its maximum at the scour hole edge, and consequently dominate the relatively small scour hole when they fall inside. The behavior of the mechanism of the sediment avalanche can be proven by the measured temporal slope variation that show gradual increase in the hole slope and sudden decrease followed by another gradual increase , as well as the longer wave length that associated with the measurements inside the scour hole than the ones of upstream of the scour hole in case of lower discharge .

The Dunes celerity is an increasing function of the flow rate. It is deduced that the user-determined overlap method is coincide with the cross-correlation function in estimating the celerity that is always higher than the celerity estimated by the method of sediment mass balance. Furthermore, the celerity computation by sediment mass balance is a decreasing function of the probability range.

The importance of the present study was appreciably mounted by running four experiments under unsteady condition. It is concluded that the mean and minimum scour reach their trough at the peak discharge step. Instead, the maximum scour depth

remains almost constant over the whole period of the hydrograph. The analysis of the transition phases demonstrates a decrease of the mean scour depth in the transition from 1.2 Q_c to 1.4 Q_c, no matters the place of the nearest approaching dune at the time of discharge modification. Unlike the rest of transition phases that show a constant increase in the scour depth till the time when the nearest dune arrives to refill the scour hole that differentiates based on the distance of the approaching dune that were determined to be 24cm in T2 and 48 cm in T3. However, in case of the existence of nearest dune at the scour hole edge at the time of discharge modification, an immediate refilling to the scour hole was evident.

The present study is valuable in emphasizing some results obtained by previous studies and exploring new sides of the live-bed scour phenomenon in covered flow. The analysis that has been performed on the scour hole slope to understand the mechanism of sediment avalanche that triggered by the dune's weight exerted on the hole edge, can be considered as a simplified platform for further investigation to build upon by applying more complicated methods to include more parameters (e.g. applying the interactions between the slices, finding the real hydraulic gradient…). Moreover, the findings of the unsteady condition are valuable; however, they must be emphasized and deepen by applying longer hydrograph time steps. In addition, higher flow rate ratios (Q/Q_c), especially higher than 2, are recommended to be applied in the next studies to discover the transition phases behavior as well as the temporal variation of the scour depth and its agreement with the graph (velocity ratio- dimensionless average scour depth) presented by Chiew and Melville (1987).

References.

Melville B. W., Coleman S. E., (2000), Bridge scour, Water Resource, LLC, Colorado, USA.

Bersani P., Bencivenga M., (2001), Le piene del Tevere a Roma, Presidenza del Consiglio dei Ministri, Dipartimento per i Servizi Tecnici Nazionali, in Italian.

Segarra Lagunes M.M., (2004), Il Tevere a Roma, Gangemi, Rome, Italy, in Italian.

Richardson E. V., Davis S. R., (2001) Evaluating scour at bridges, Forth Edition, Rep. FHWA-NHI 01-001, HEC No. 18, Federal Highway Administration, Washington, D.C.

Imhof D., (2004), Risk assessment of existing bridge structures, PhD Thesis, University of Cambridge, UK.

Deng L., Cai C.S., (2010), Bridge Scour: Prediction, Modeling, Monitoring, and Countermeasures Review, Practice Periodical on Structural Design and Construction, 15, 125–134.

Brice J.C., Blodgett J.C., (1978), Countermeasures for hydraulic problems at bridges, Federal Highway Administration Report FHWA-RD-78-162.

Macky G.H., (1990), Survey of roading expenditure due to scour, Report CR 90.09, DSIR Hydrology Centre, Christchurch, New Zeland.

Graf W.H., (1998), Fluvial Hydraulics, Wiley, Chichester, U.K.

Brandimarte L, Paron P, Baldassarre GD (2012) Bridge pier scour: a review of processes, measurements and estimates. Environ Eng Manag J 11(5):975–989.

Chanson, H. (2004) The Hydraulics of Open Channel Flow: An Introduction, Second edition. Elsevier Butterworth-Heinemann.

Henderson, F.M. (1966) Open Channel Flow. (MacMillan Company, New York, USA).

Graf, W.H. (1971) Hydraulics of Sediment Transport. (McGraw-Hill: New York, USA).

Graf W.H., (1998), Fluvial Hydraulics, Wiley, Chichester, U.K.

Shen H. W., Schneider V. R., Karaki S., (1969), Local scour around bridge piers, Journal of Hydraulic Division, Am. Soc. Civ. Eng., 95 , 1919–1940.

Raudkivi A. J., (1991), Scour at Bridge Piers, In: IAHR Hydraulic Structures Design Manual 2, Breusers H., Raudkivi A.J. (Eds.), Balkema, Rotterdam, The Netherlands.

Melville B. W., Chiew Y.-M., (1999), Time scale for local scour at bridge piers, Journal of Hydraulic Engineering, 125, 59–65.

Brath A., Montanari A., (2000), Vulnerabilità idraulica dei ponti: In soluzioni innovative nella manutenzione dei corsi d'acqua con forte trasporto solido, (in Italian), L'Acqua 3, 45–60.

Radice and Lauva, (2017), Live-bed scour in a covered flow, Journal of hydraulic engineering, 143(10): 06017016.

Chiew and Melville,(1987), Local scour around bridge piers, JOURNAL OF HYDRAULIC RESEARCH. VOL. 25, 1987, NO. 1

Wen-Yi Chang; Jihn-Sung Lai; and Chin-Lien Yen, F.ASCE, (2004), Evolution of Scour Depth at Circular Bridge Piers, J. Hydraul. Eng., 2004.130:905-913.

Ettema, R., (1980), Scour at Bridge Piers, Ph.D. Thesis, Auckland University, Auckland, New Zealand. Report No. 124.

Chee, R. K. W., (1982), Live-Bed Scour at Bridge Sites, M.E. Thesis, Auckland University, Auckland, New Zealand.

Bernd Ettmer; Franciska Orth; and Oscar Link,(2015), Live-Bed Scour at Bridge Piers in a Lightweight Polystyrene Bed, J. Hydraul. Eng. 2015.141.

Guillermo López, F.ASCE1; Luis Teixeira, F.ASCE2; Miguel Ortega-Sánchez, F.ASCE3; and Gonzalo Simarro, F.ASCE4 ,(2014), Estimating Final Scour Depth under Clear-Water Flood Waves, J. Hydraul. Eng., 2014, 140(3): 328-332.

Kothyari, U. C., Garde, R. J., and Ranga Raju, K. G. (1992). “Temporal variation of local scour around circular bridge piers.” J. Hydraul. Eng., 10.1061/(ASCE)0733-9429(1992)118:8(1091), 1091–1106.

Jian-Hao Hong1; Yee-Meng Chiew, M.ASCE2; Po-Hung Yeh3; and Hsun-Chuan Chan4, (2016), Evolution of Local Pier-Scour Depth with Dune Migration in Subcritical Flow Conditions, J. Hydraul. Eng., 04016098.

Derek G. Goring[1] and Vladimir I. Nikora[2] ,(2002), Despiking Acoustic Doppler Velocimeter Data, Journal of Hydraulic Engineering, Vol. 128, No. 1.

MELVILLE, B. W., (1984), Live-Bed Scour at Bridge Piers, Journal of Hydraulic Engineering, Vol. 110, No.
9, A.S.C.E., pp. 1234-1247.

JAIN, S. C. and FISCHER, E. E., (1979), Scour Around Bridge Piers at High Froude Numbers, Report Number F.H.W.A.-R.D.-79-104, Federal Highway Administration, Washington D.C.

Ballio, F., Radice, A., and Dey, S. (2010). “Temporal scales for live-bed scour at abutments.” J. Hydraul. Eng., 136, 395–402.

Peng Wu, Ph.D.[1]; Ram Balachandar, Ph.D., P.Eng.[2]; and Jueyi Sui, Ph.D., P.Eng.[3] ,(2016), Local Scour around Bridge Piers under Ice-Covered Conditions, J. Hydraul. Eng.,142(1): 04015038

D. Max Sheppard, M.ASCE[1]; and William Miller Jr.[2],(2006), Live-Bed Local Pier Scour Experiments, J. Hydraul. Eng. ,132:635-642.

Deng L., Cai C.S., (2010), Bridge Scour: Prediction, Modeling, Monitoring, and Countermeasures Review, Practice Periodical on Structural Design and Construction, 15, 125–134.